

Proton irradiation effects on Nb₃Sn wires and thin platelets in view of High Luminosity LHC upgrade

THÈSE

Présentée à la Faculté des sciences de l'Université de Genève
pour obtenir le grade de Docteur ès Sciences, mention
physique

par

Tiziana Spina

De Bojano, Italie

Thèse N°

To my family

Contents

Acknowledgement	iv
Introduction.....	vi
CHAPTER 1: OVERVIEW AND PHYSICAL KEY CONCEPTS	1
1.1. Outline of the problem	2
1.1.1. The radiation environment in the innermost quadrupole windings.....	2
1.2. Physical background	3
1.2.1. The A15 phase	3
1.2.2. The Bragg – Williams long – range atomic order parameter in A15 compounds.....	8
1.2.3. The effect of disorder on T_c , B_{c2} and ρ_n	14
1.3. Radiation damage and radiation effects in A15 superconductors	15
1.3.1. Radiation damage theory	16
1.3.2. Differences in the radiation damage induced by protons and by neutrons	25
1.3.3. Radiation effects in superconductors	33
1.4. Flux pinning in multifilamentary Nb_3Sn wires before and after irradiation	40
1.4.1. Flux pinning before irradiation	43
1.4.2. Flux pinning after irradiation	47
CHAPTER 2: PREPARATION AND PROPERTIES OF Nb_3Sn SAMPLES	50
2.1. Description of the RRP and PIT Nb_3Sn multifilamentary wires.....	50
2.1.1. Characteristics of the Ta and Ti alloyed Nb_3Sn wires	50
2.1.2. Heat treatments	52
2.2. The fabrication of thin Nb_3Sn platelets.....	53
2.2.1. HIP (Hot Isostatic Pressure) process to fabricate homogeneous bulk Nb_3Sn samples	54
2.2.2. Cutting of thin platelets by spark – erosion	56
2.2.3. Flash Anneal for stress release.....	58
2.2.4. Characterization of the Nb_3Sn bulk samples by SEM, X-ray and AC susceptibility measurements.....	58
2.3. Main differences between bulk and multifilamentary Nb_3Sn wires	61
CHAPTER 3: MEASUREMENTS and PROTON IRRADIATION EXPERIMENTAL SET-UP	63
3.1. High energy proton irradiation experimental set-up	63
3.1.1. Proton irradiation of Nb_3Sn wires	63
3.1.2. Proton irradiation on Nb_3Sn platelets: the Bragg peak experiment.....	66

3.2. Magnetization measurements.....	73
3.2.1. VSM measurements to obtain J_c	73
3.2.2. AC susceptibility measurements to obtain T_c	76
3.3. Diffraction measurements	78
3.3.1. X-ray diffraction measurements at Unige (before irradiation).....	79
3.3.2. Synchrotron measurements at NRC-KI (after irradiation)	87
CHAPTER 4: RESULTS AND DISCUSSION	89
4.1. Results on Nb_3Sn wires.....	89
4.1.1. Decrease of T_c after proton irradiation	90
4.1.2. Enhancement of J_c after proton irradiation.....	92
4.1.3. Quantitative pinning force analysis.....	96
4.1.4. Comparison between proton and neutron irradiation on Nb_3Sn wires	108
4.2. Results on Nb_3Sn platelets	110
4.2.1. The Bragg –Williams LRO parameter	111
4.2.2. Decrease of T_c at the Bragg peak	118
CHAPTER 5: CALCULATION OF THE DPA NUMBER	122
5.1. Definition and calculation of dpa with FLUKA code	123
5.2. Evaluation of dpa at the Bragg Peak	124
5.3. Scaling between fluence and displacement per atom (dpa)	128
5.3.1. Relationship between dpa and physical properties	128
5.4. Relationship between dpa and S	134
5.5. The effects of protons and neutrons irradiation on the thermal stability of Nb_3Sn quadrupoles for HL-LHC Upgrade	136
CONCLUSIONS AND PERSPECTIVES	137
Résumé.....	141
BIBLIOGRAPHY	144
CURRICULUM VITAE	157

Acknowledgement

The present work was realized at CERN in the laboratories of the Superconductors and Superconducting Devices Section (SCD) in the Technology Department (TE). A part of the experimental work has been performed at the University of Geneva in the Department of Quantum Matter Physics (DQMP) and in the Laboratory of Crystallography of the Department of Solid State Physics (DPMC).

I wish to express my special thanks to Prof. René Flükiger for the guidance, enthusiasm, ideas, and support he has given me throughout the present work, I will never forget his teachings.

I gratefully remember the advice of Prof. Radovan Cerny of the Laboratory of Crystallography at the University of Geneva during the determination of the atomic order parameter by X-ray refining.

My special thanks go to thank both Dr. Amalia Ballarino and Dr. Luca Bottura for the financial support during these three years in the frame of the PhD student program at CERN.

I would like to thank Dr. Francesco Cerutti and Dr. Anton Lechner from the FLUKA team at CERN for the enlightening discussions about the radiation conditions in LHC Upgrade and the introduction in the problematic of the determination of the dpa numbers.

I address a particular thank to Dr. Bernardo Bordini for his precious help during the quantitative analysis of the pinning force after high energy proton irradiations.

I would also like to thank Dr. Michael Eisterer from the Atom Institute in Vienna for his constructive criticism as member of dissertation committee.

In addition, I convey my sincere thanks to the researchers from the University of Geneva for fruitful discussions, in particular Prof. Carmine Senatore, Dr. Marco Bonura, Dr. Marta Gibert Gutierrez, Dr. Enrico Giannini, Dr. Florin Buta as well as Dr. Bernd Seeber, Mr. Damien Zurmuehle and Mrs. Geraldine Cravotto for their help in the Nb₃Sn sample preparation.

I would also like to thank the staff of the SCD section at CERN, particularly Dr. David Richter for the excellent magnetization measurements performed on the Nb₃Sn wires before and after proton irradiations as well as Dr. Christian Scheuerlein for the organization, delivering and distribution of the radioactive samples.

I'm indebted to the working team in Louvain, in particular M. Loiselet and the team of IRRAD1 at CERN especially F. Ravotti and M. Glaser as well as to Dr. Y. Zubavichus, Dr. S. Shavkin and Prof. A. Ryazanov of Kurchatov Institute (Moscow) for the proton irradiation and crystallographic as well as the magnetization measurements of irradiated Nb₃Sn platelets.

Last but no least I would like to acknowledge the support of my loving family, none of this work would be possible without their support.

Introduction

In order to estimate the lifetime of quadrupole magnets in the High-Luminosity (HL) LHC accelerator, a precise knowledge of the potential damage on the superconductors caused by the simultaneous action of several high energy irradiation sources is needed.

The present work treats the effects of high energy proton irradiation on the physical properties of Nb_3Sn , the superconducting material used in the quadrupoles of HL – LHC: the critical current density (J_c), the critical temperature (T_c), the upper critical field (H_{c2}) and finally the Bragg - Williams atomic order parameter (S) in the Nb_3Sn wires in the quadrupoles. The significant variations of the critical surface induced by radiation could indeed lead to loss of performance of the superconducting magnets.

The whole work can be subdivided in five major parts:

- a) Study of the behavior of wires irradiated at high energy protons traveling through the wire (steady loss region, excluding the location of the Bragg peak): in this case a direct comparison with neutron irradiation on the same Nb_3Sn wires is performed.
- b) Study of the enhancement of J_c after proton irradiation: a *two-mechanism* model has been introduced to analyze the volume pinning force after irradiation to take into account the contribution of the radiation induced defects in addition to that due to grain boundaries.
- c) Study of the Bragg peak region of wires irradiated with high energy protons. In this region protons undergo a total energy loss; there is no analogy with neutron irradiation. The effects of irradiation in the Bragg peak region have never been studied before on Nb_3Sn crystallographic structure.
- d) A new work to establish a correlation between the displacement per atom (dpa) values and the variation of the atomic order parameter, S , as well as the correlated variation of T_c in Nb_3Sn .

- e) Application of the results to the problem of radiation damage in HL-LHC: study of the effects of irradiation on the thermal stability of Nb_3Sn quadrupoles for HL-LHC Upgrade.

Outline

The thesis is structured in five chapters:

- in the first chapter an overview of the physical concepts behind the understanding of the radiation damage in superconducting material is given;
- in the second chapter the preparation and properties of Nb_3Sn samples (wires and platelets) are described to arrive at a detailed knowledge of the atomic ordering before irradiation;
- in the third chapter the different types of measurements to investigate the radiation damage effects and the proton irradiation experimental set-up are reported;
- in the fourth chapter the results obtained are presented and discussed;
- in the fifth chapter the comparison between the radiation effects induced by charged particle and neutron irradiation on the critical properties of Nb_3Sn wires under investigation is performed introducing the statistical quantity, i.e. the displacement per atom (dpa), calculated by means of Monte Carlo simulation (FLUKA code); in addition in this chapter the proton damage effects on the new Nb_3Sn quadrupole (QXF) for HL-LHC is estimated.

CHAPTER 1: OVERVIEW AND PHYSICAL KEY CONCEPTS

In this chapter some aspects of the superconductivity in A15 superconductors and of radiation damage mechanism will be discussed.

In Section 1.1 a brief outline of the radiation environment expected during the HL – LHC lifetime is given; in Section 1.2 the Nb-Sn phase diagram as well as the behavior of the low temperature properties of A15 compound Nb₃Sn are described to give the background for the evaluation of the Bragg-Williams long – range order (or LRO) parameter, S. In literature, Nb₃Sn was so far assumed to be perfectly ordered, based on the very low value of the normal state electrical resistivity, by analogy to other A15 type compounds, e.g. V₃Si. In the present work, the order parameter S was thus experimentally determined by means of a refinement procedure on X-ray diffraction data, which will be described in detail. The parameter S is an important experimental quantity when analyzing the effects induced by high energy irradiation on the crystal structure of Nb₃Sn; as mentioned above, one of the goals of the present work is to relate this quantity to the displacement per atom (dpa). This value is commonly used in irradiation studies and is obtained through Monte Carlo simulations (FLUKA code [1]).

In contrast to the order parameter S, the dpa parameter cannot be directly measured and no general correlation between dpa and physical properties has been established yet. In particular, no direct correlation study was undertaken between the dpa value and the change of the order parameter in Nb₃Sn after high energy irradiation. Based on careful calculations on the dpa in the innermost quadrupoles of HL-LHC by A. Lechner, L. Esposito, F. Cerutti et al. [2], a correlation between this quantity and T_c would allow determining the effective variation of T_c during the acceleration lifetime.

In the present work, the dpa was calculated using the FLUKA code (see Chapter 5). In Section 1.3 the radiation damage theory, as well as the irradiation effects in A15 superconductors are discussed to underline the mechanisms governing the observable changes in

the critical parameter T_c , J_c and B_{c2} . Finally, the literature concerning the flux pinning in multifilamentary Nb_3Sn wires before and after irradiation is reported in Section 1.4.

1.1. Outline of the problem

In order to reach the integrated luminosity of 3000 fb^{-1} in the HL – LHC accelerator, the NbTi inner triplet in the LHC project will be replaced by Nb_3Sn quadrupoles with larger aperture [3]. To ensure the stability of these magnets under operational conditions it is important to study the behavior of T_c and J_c as well as B_{c2} up to the highest fluences reached during the entire accelerator lifetime. Since no available source is able to produce simultaneously different high energy sources, irradiation effects have to be studied separately for each one of them being present in the HL-LHC radiation environment, i.e. photons, electrons, pions, neutrons and protons.

In this work the effects of proton irradiation on the superconducting properties of ternary RRP and PIT Nb_3Sn wires are studied. The data are compared with those obtained after neutron irradiation of the same Nb_3Sn wires by T. Baumgartner et al. [4], in the frame of collaboration between CERN and the Atominsttitut Vienna (See Subsections 4.1.4 and 5.3.1 for further details).

1.1.1. The radiation environment in the innermost quadrupole windings

The proton fluences studied in the present work are well beyond those calculated by F. Cerutti [5] and A. Lechner [2] on the basis of FLUKA simulations for the whole HL-LHC operation time. These calculations show that the maximum dpa (1.8×10^{-4}) is expected at the inner winding of the most exposed quadrupole Q1 (see also Section 5.5) and the radiation spectrum will consist of photons, electrons, protons and pions, with energies up to $\sim 100 \text{ GeV}$ and peaks at $\sim 100 \text{ MeV}$ and neutrons with peak value around 1 MeV . At a luminosity of 3000 fb^{-1} the maximum fluence

estimated for the quadrupole, after introducing an inner W shield, is: $\sim 1.8 \times 10^{21}$ neutrons/m² and 1.3×10^{20} protons/m² (total hadrons: $> 3 \times 10^{19}$ hadrons/m²) [2].

Recently, the luminosity to be reached was increased to 4000 fb⁻¹; all values calculated for 3000 fb⁻¹ have to be multiply simply by 4/3.

1.2. Physical background

Superconductivity in Nb₃Sn was discovered in 1954 by Matthias et al. [6]; up to the discovery of the HTS materials in 1986 the strong interest for Nb₃Sn was due to the fact that its T_c was among the highest ones of the materials known at that time having the potential to be used as wires in applications. Nb₃Sn crystallizes in the Cr₃Si structure, forming a brittle intermetallic compound. It belongs to a class of materials known as A15 compounds, most of them being stable at the stoichiometric composition A₃B. Seventy binary compounds have the A15 structure and six of these have a T_c higher than 17 K (the highest critical temperature around 23 K is reached from the Nb₃Ge compound followed by Nb₃Sn with T_c around 18 K) [7].

In order to understand the effects of proton irradiation on Nb₃Sn wires and thin films it is important to know the physical properties for different states of atomic ordering in A15 systems. In addition, the correlation between radiation damage and radiation induced disorder in atomic structure must be known. The goal of the following subsections is a review of the physical principles of radiation damage.

1.2.1. The A15 phase

In compounds with the chemical formula A₃B where the A atoms are transition metals of the 4th, 5th or 6th column of the periodic table and the B atoms can be either transition (usually noble metals) or non – transition metals. The structure has a primitive cubic cell of 8 atoms and belongs to the space group O_h³ - Pm3n. Its unit cell, shown in [Figure 1](#), has 6A atoms in 6c sites at (1/4, 0, 1/2), (1/2, 1/4, 0), (0, 1/2, 1/4), (3/4, 0, 1/2), (1/2, 3/4, 0), (0, 1/2, 3/4) with point

symmetry, $\bar{4}2m$ and 2B atoms in 2a sites at $(0, 0, 0)$ and $(1/2, 1/2, 1/2)$ with point symmetry m3. The B atoms have 12 neighbors at a distance $r_A + r_B = \frac{5a}{4}$. The A atoms have a larger coordination number of 14 at a distance $2r_A = \frac{6a}{4}$ (a is the lattice parameter, r_A and r_B are the atomic radii of the A and B atoms respectively). In the Nb_3Sn structure the 6c sites are occupied by Nb atoms and the 2a sites by Sn atoms.

An important feature of the A15 structure is the presence of orthogonal chains of A atoms along the three [100] directions bisecting each face of the bcc lattice formed by B atoms. An interesting feature in Nb_3Sn is the reduction in Nb – Nb interatomic spacing in the chains with respect to the cubic Nb crystals¹. Following the Labb   – Friedel model for perfect A15 lattice [8] this reduction in Nb – Nb chains results in a narrow peak in the d-band density of states (DOS) near the Fermi level. According to the BCS microscopic theory the critical temperature is $T_c \approx \theta_D \exp [1/(N(0)V)]$, where $N(0)$ is the electron density of states at the Fermi surface, θ_D

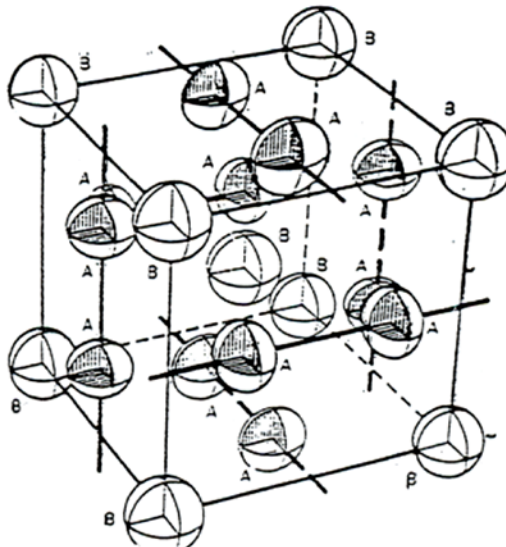


Figure 1 The A15 structure. The picture shows the structural arrangement of the A and B atoms in the unit cell A_6B_2 . The drawing also schematically depicts the anisotropy along the chains, as a consequence of the very short A-A nearest neighbour distances [9].

is the Debye temperature proportional to $N(0)^{\frac{1}{3}}$, and V is the electron – phonon interaction parameter. It follows that the high T_c in this structure comes from the very high DOS at the

¹ In Nb_3Sn the Nb – Nb distance along the chain is $(a_0/2) < 2.65\text{\AA}$, which is smaller than the nearest neighbor Nb – Nb distance $\sqrt{3}a_0/2 = 2.86\text{\AA}$ in elemental, bcc niobium [134].

Fermi level, $N(0)$ [10]. Actually the BCS theory is valid for weak coupling superconductors, i.e. for superconductors with a very small electron-phonon coupling constant, λ_{ep} ($\lambda_{ep} \ll 1$). For Nb_3Sn the strong coupling theory has to be applied ($\lambda_{ep} \sim 1.8$) (Migdal – Eliashberg theory) for which: $\frac{T_c}{\omega_0} = \exp\left(\frac{-(1+\lambda_{ep})}{\lambda_{ep} - \mu^* - \langle\omega\rangle\langle\omega_0\rangle^{-1}\lambda_{ep}\mu^*}\right)$, where $\mu^* = \frac{N(0)V_c}{1+N(0)V_c\ln(E_B/\omega_0)}$ is the Coulomb pseudopotential of Morel and Anderson [11] and ω_0 is the maximum phonon frequency [12].

The phase diagram of Nb – Sn intermetallic compound

The A15 structure normally occurs between 18 and 25 at.% Sn. As reported by Flükiger [13], the type of formation of the A15 phase in a system $\text{A}_{1-\beta}\text{B}_\beta$ (where β is the B composition) is essentially governed by the B element.

Intermetallic $\text{Nb}_{1-\beta}\text{Sn}_\beta$ is based on the superconductor Nb, which crystallizes in a bcc Nb structure ($T_c=9.2\text{K}$). At the thermodynamic equilibrium it can form in the compounds $\text{Nb}_{1-\beta}\text{Sn}_\beta$ ($0.18 < \beta \leq 0.25$), Nb_6Sn_5 and NbSn_2 , according to the generally accepted binary phase diagram by Charlesworth et al., shown in [Figure 2](#). In the present work we generally use the form Nb_3Sn when the precise Sn content is not important.

The Nb_3Sn phase can be formed either above 930°C in the presence of a Sn – Nb melt, or below this temperature by solid state reactions between Nb and Nb_6Sn_5 or NbSn_2 . In the solid solution of Nb – Sn at low Sn concentrations β the critical temperature of bcc Nb is gradually reduced from about 9.2 K to about 4 K at $\beta=0.05$ [14]. The formation of homogeneous $\text{Nb}_{1-\beta}\text{Sn}_\beta$ samples with a precise Sn content is rather difficult, due to the high vapor pressure of Sn at the formation temperature of the A15 phase; this difficulty can be overcome with a preparation under high pressures, following Goldacker et al. [15].

As will be explained in the following, the knowledge of the precise stability limits of A15 phase in Nb_3Sn is important since the superconducting and normal state properties depend critically on the composition β [9].

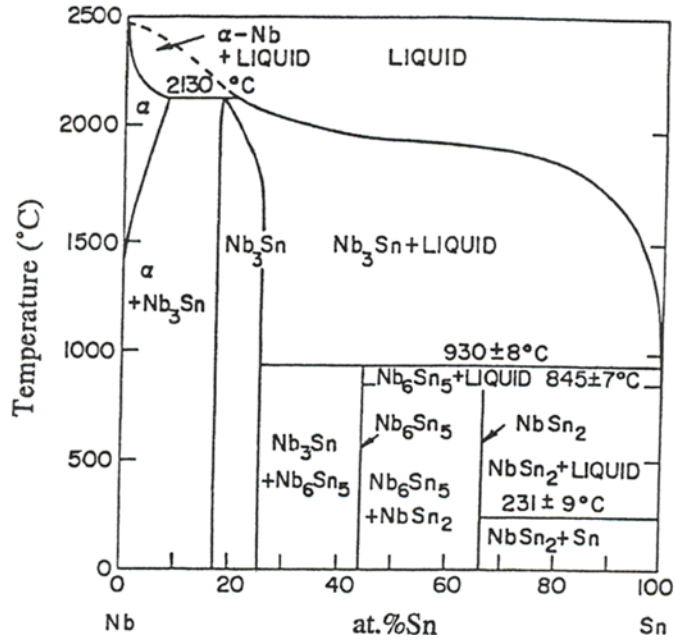


Figure 2 The Nb-Sn phase. After Charlesworth et al. 1970 [15].

Critical parameters with Sn composition

The variation of T_c in Nb_3Sn , shown in Figure 3, has a linear behavior up to $\beta = 24.5$ at.%Sn. At Sn contents exceeding 24.5 at.%Sn, a “saturation” in T_c is observed. As reported by Devantay et al. [16], the extrapolation of T_c to 25 at.%Sn for a hypothetical, cubic and stoichiometric sample would yield 19 K, i.e. nearly 1 K higher than the reported value for tetragonal stoichiometric Nb_3Sn . This is indirectly confirmed by the slight increase of T_c in Ta alloyed Nb_3Sn occurring simultaneously with the suppression of martensitic transformation.

The variation of $B_{c2}(0)$ with the Sn composition (shown in Figure 4) follows the corresponding linear variation of T_c up to 24 at.%Sn but decreases again above ~ 24 at.%Sn $B_{c2}(0)$. The different behavior above 24 at.%Sn with respect to the saturation trend found in $T_c(\beta)$ can be explained as follows: below 24 at.%Sn, the increase of T_c and of the specific heat, γ , is dominant over the decrease of ρ_0 , thus $B_{c2}(0)$ increases with β ; above 24 at.%Sn, T_c (and probably also γ) shows the above mentioned “saturation” thus the strong decrease observed for $B_{c2}(0)$ can be

explained by the variation of the electrical resistivity, ρ_0 , which is itself a function of composition and atomic order, as shown in [Figure 5](#) [17].

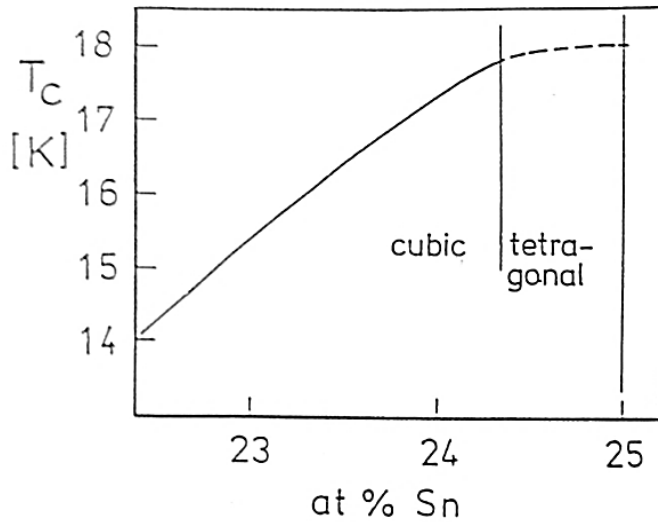


Figure 3 T_c vs Sn concentration for binary Nb_3Sn . After Devantay et al [18].

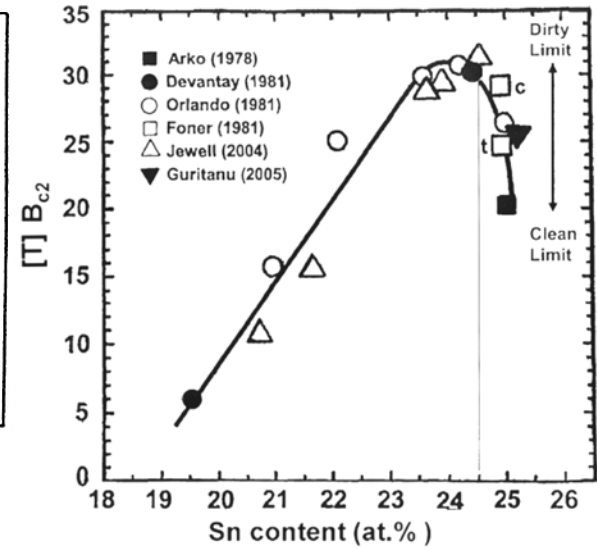


Figure 4 B_{c2} vs Sn content for binary Nb_3Sn [18].

For high field magnet applications it is important to have superconducting wires with high upper critical fields and high critical temperature values. The upper critical field B_{c2} can be optimized by adding certain elements to the precursors of Nb_3Sn wires (mainly Ta and Ti), thus producing ternary A15 phases with enhanced normal state resistivity. The effects of additives are described in many publications such as [19, 20, 21, 22, 23] (Ta additions), and [24, 19, 20, 21, 25, 26, 23] (Ti additions). As pointed out by Flükiger et al. [20], Ta substitutes Nb on the chains, thus forming $(\text{Nb}_{1-x}\text{Ta}_x)_3\text{Sn}$, whereas Ti substitutes Sn, yielding $\text{Nb}_3(\text{Sn}_{1-x}\text{Ti}_x)$. As a side effect of the addition of doping elements to Nb_3Sn , the martensitic transformation to the tetragonal phase is suppressed [17], which allows taking advantage of the higher critical temperature values of the cubic phase: 18.3 K instead of 18.0 K. The linear behavior of the lattice constant, a , as a function of Sn composition is shown in [Figure 6](#).

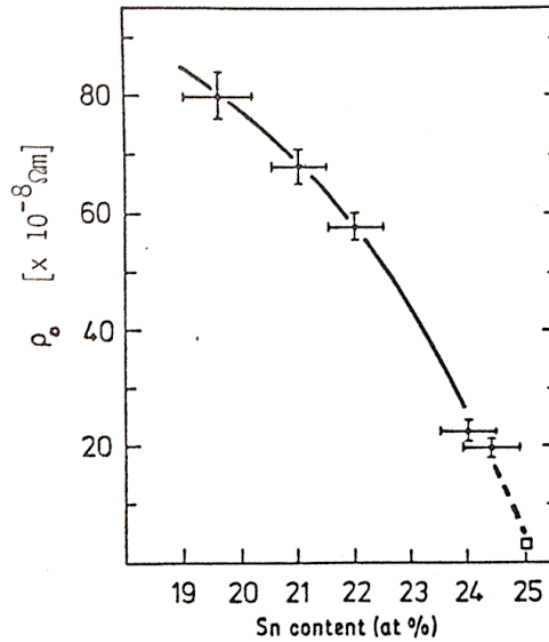


Figure 5 Variation of ρ_0 in $\text{Nb}_{1-\beta}\text{Sn}_\beta$ as a function of the Sn content. Between 24 at.%Sn and 25 at.%Sn there is a smooth transition between a dirty type II superconductor (with an electronic mean free path $\lambda < 3\text{nm}$) to a clean type II superconductor with $\lambda > 10\text{nm}$ Devantay et al. [16].

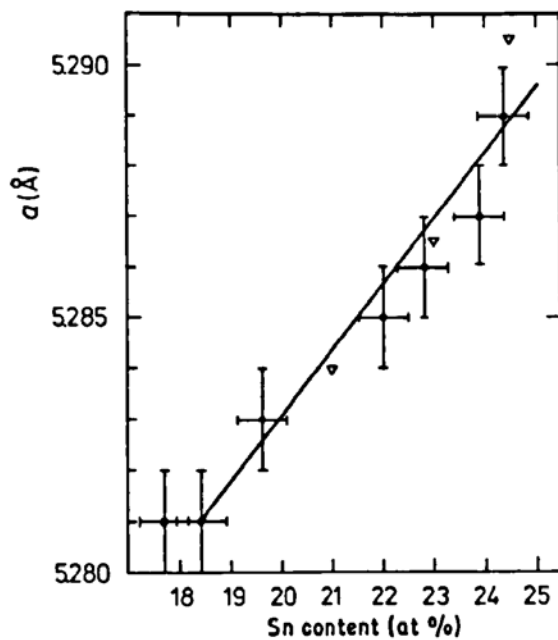


Figure 6 Lattice constant vs Sn content in Nb_3Sn [27]

1.2.2. The Bragg – Williams long – range atomic order parameter in A15 compounds

Atomic ordering can be defined as a distribution of atoms over the lattice sites of the crystal at thermodynamic equilibrium and is described by the Bragg – Williams long – range atomic order parameter [28] (abbreviated: LRO parameter) as a function of temperature: $S=S(T)$.

The LRO parameter value in a fully ordered stoichiometric A15 compound is $S=1$. Usually, the experimentally derived value of S deviates from unity, $S \leq 1$, depending on the thermal history of the sample². The equilibrium order parameter, S_e , can only be modified at temperatures above the diffusion limit temperature, $T_D \sim 0.5T_F [K]$, where T_F is the melting temperature. All order parameter measurements performed at room temperature describe thus in reality a non –

² A certain amount of disorder can be frozen in since the cooling process from the melt or from annealing temperature occurs in finite times.

equilibrium state. However, due to the slow diffusion, there is a small difference between the order parameter at room temperature and that at $T \sim T_D$, i.e. at $T \sim 900^\circ C$ [29].

Definition of the Bragg - Williams LRO parameter, S

In A15 type compound of the general formula $A_{1-\beta}B_\beta$ the degree of atomic ordering can be described through the two parameters, S_a and S_b for each lattice site, defined as:

$$S_a = \frac{r_a - (1-\beta)}{1 - (1-\beta)} = \frac{r_a - (1-\beta)}{\beta} \quad \text{and} \quad S_b = \frac{r_b - \beta}{1 - \beta} \quad 1$$

where β is the Sn composition and r_a and r_b are the occupation factors for the A and B atoms respectively; particularly r_a is defined by the fraction of 6c sites (or *a sites*) occupied by A atoms and r_b by the fraction of 2a sites (or *b sites*) occupied by B atoms.

The LRO parameter S is defined in such a way that $S=1$ for the perfectly ordered lattice and $S=0$ for random distribution representing complete disordering in the lattice. These two states correspond to $r_a=1$ (or $r_b=1$) and $r_a=0.75$ ($r_b=0.25$) at the composition β .

It is possible to connect S_a and S_b and the two occupation factors r_a and r_b by the formulas:

$$S_b = \frac{3\beta}{1-\beta} S_a \quad \text{and} \quad r_b = 3r_a - 3 + 4\beta. \quad 2$$

At $\beta = 0.25$, it follows from equation 2 that $r_b = 3r_a - 2$, i.e. the degree of atomic ordering is fully described by only one parameter: it is $S_a = S_b = S$.

Partial disorder in the A15 structure can be induced by a random site exchange between A and B atoms, as shown in Figure 7.

As will be discuss later on, the importance in the observation of order parameter changes in A15 type compounds resides in the correlation between deviations from perfect ordering and the superconducting transition temperature T_c .

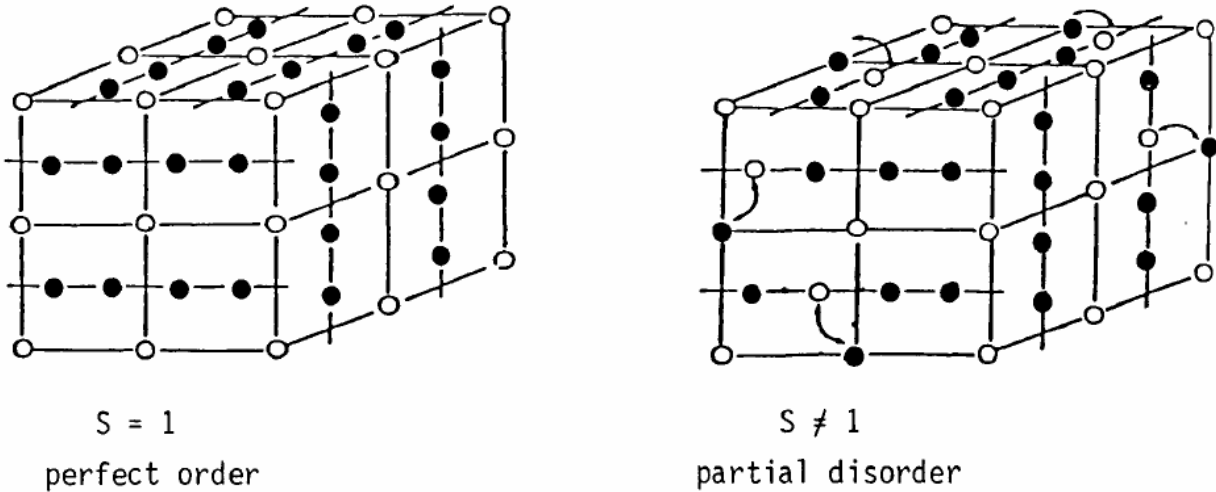


Figure 7 The A15 type structure of a system A_3B with different occupation of the 6c (black atoms) and the 2a (white atoms) sites by the two atomic species. $S=1$ means perfect ordering, i.e. the probability to find atom A on 6c sites is 1 and the probability to find atom B on 2a sites is 1. $S = 0$ means complete disorder, i.e. the probability to find atom A on 6c sites is 0.75 and the probability to find atom B on 2a sites is 0.25.

The Rietveld refinement to obtain S values

The first accurate measurement of order parameters in several A15 compounds were accomplished by Van Reuth et al. (1967) [30] and Van Reuth and Waterstrat (1968) [31] by X – Ray diffraction measurements. Later on, Flükiger et al. [32] used also neutron diffraction measurements. For the present work the X – ray diffraction was adopted. The procedure to obtain S consists in comparing the measured and the calculated X-ray diffraction intensities, i.e. performing a Rietveld refinement, thus minimizing the function M computed as the weighted sum of the difference between the observed intensity, $I_{obs,i}$, and the calculated intensity, $I_{calc,i}$:

$$M = \sum_{i=1}^n \omega_i (I_{obs,i} - I_{calc,i})^2 \quad 3$$

with n the total number of points used in the refinement and ω_i , the weight obtained from the variance in $I_{obs,i}$: $\omega_i = \frac{1}{\sigma_{obs,i}^2}$.

The spectrum for the calculated intensities, $I_{calc,i}$ depends on phases (crystal structure, microstructure, quantity, cell volume, texture, stress, chemistry etc.), on instrument geometry

characteristics (beam intensity, Lorentz – Polarization, background, resolution, aberrations, radiation etc.) and on sample (position, shape and dimensions, orientation) and is described by equation 4:

$$I_{calc,i} = \sum_{j=1}^{N_{phases}} K_j \sum_{k=1}^{N_{peaks}} L_k |F_{k,j}(S, B_n)|^2 S_j(2\theta_i - 2\theta_{k,j}) P_{k,j} A_j + bkg_i \quad 4$$

where K_j is the scale factor for each phase, L_k is the trigonometric factor known as Lorentz - Polarization factor, $F_{k,j}(S)$ is the structure factor that is a function of the LRO parameter, S , and of the temperature factor, B_n , $S_j(2\theta_i - 2\theta_{k,j})$ is the profile shape function³, $P_{k,j}$ is the preferred orientation factor (or texture), A_j is the absorption factor that describes the attenuation of the primary and diffracted beams, bkg_i is the polynomial background function. One single peak is composed by all equivalent reflections m_k and the number of peaks, N_{peaks} , is determined by the symmetry and by the space group of the phase.

The agreement factors to estimate the quality of the least square refinement procedure are the R – factors (“weighted” residual factor, R_{wp} , and the “expected” residual factor, R_{exp}) and the “Goodness of Fit”, Goff or “Reduced chi – square”, χ^2 .

The “weighted” residual factor, R_{wp} , is the most straightforward discrepancy index, it follows directly from the square root of the quantity minimized, scaled by the weighted intensities:

$$R_{wp} = 100 \sqrt{\frac{M}{\sum_{i=1}^n \omega_i I_{obs,i}^2}} \quad 5$$

its absolute value does not depend on the absolute value of the intensities but on the background.

The R_{exp} is the minimum R_{wp} value reachable using a certain number of refineable parameters, p :

$$R_{exp} = 100 \sqrt{\frac{n-p}{\sum_i \omega_i I_{obs,i}^2}} \quad 6$$

³ Different profile shape functions are available (Gaussian, Cauchy, Voigt and Pseudo – Voigt (PV), Pearson VII, etc.); in this study the PV function was used: $PV(2\theta_i - 2\theta_k) = I_n[\eta_k \left(\frac{1}{1+S_{i,k}^2} \right) + (1-\eta_k) \exp - S_{i,k}^2 \ln 2]$ where $S_{i,k} = 2\theta_i - 2\theta_k / \omega_k$ and from Caglioti formula and Gaussianity ω_k and η_k are determined respectively.

where $n-p$ is the number of degrees of freedom. Conventional R-Factors, cR_{wp} , cR_{exp} , are calculated as above but using background – corrected counts, i.e. in the denominators the quantity $I_{obs,I}$ is changed to $I_{obs,I} - bkg_i$ [33].

The “Goodness of Fit”, GofF, is the ratio between the R_{wp} and R_{exp} and cannot be lower than 1; a good refinement gives GofF values lower than 2.

The structure factor

The most important factor that influences the refinement procedure to obtain the LRO parameter is the structure factor defined as:

$$F_{hkl} = \sum_i f_i \exp -B_i \frac{\sin^2 \theta}{\lambda^2} [\exp i(\frac{2\pi}{\lambda} \mathbf{r}_i \cdot \mathbf{q})] \quad 7$$

where f_i is the atomic scattering factor (or atomic form factor) of the atom i at a site described by the atomic position vector \mathbf{r}_i , B_i is the temperature factor and \mathbf{q} is the scattering wave vector.

The Debye-Waller temperature factor B_i describes the negative variation of the intensity of scattering due to thermal vibration of the atoms and it is connected with the mean square amplitude of atomic oscillations, $\overline{u_i^2}$, that can be anisotropic or isotropic. For isotropic vibration the term B_i can be written as $B_i = 8\pi^2 \overline{u_i^2}$, and theoretically can be derived through the Debye expression:

$$B_i = \frac{6h^2}{m_i k \Theta_D} \left\{ \frac{\phi(x)}{x} + \frac{1}{4} \right\} \quad 8$$

where Θ_D is the Debye temperature, m_i is the mass of the atoms or vibrating systems, x is the ratio of Θ_D to the absolute temperature, and $\phi(x) = \frac{1}{x} \int_0^x \frac{\xi}{e^\xi - 1} d\xi$ is a function given in table 5.2.2B of the International Tables of Crystallography. For Nb and Sn atom the values for B_i are 0.43 and 0.3 \AA^2 respectively, which for Nb_3Sn leads to an estimated weighted average of: $\overline{B_i}_{\text{Nb}_3\text{Sn}} = \frac{3B_i_{\text{Nb}} + B_i_{\text{Sn}}}{4} = 0.4 \text{\AA}^2$.

The atomic scattering factor, f_i , defined as the ratio between the amplitude scattered by an atom and a single electron, is proportional to the number of electrons and it decreases with increasing scattering angle. The most frequently used values of the atomic scattering factor as a function of $\frac{\sin\theta}{\lambda}$ are those calculated by Cromer et al. [34] on the basis of Hartree – Fock functions.

For a perfectly ordered, stoichiometric A15 type compound A_3B the structure factor will be:

$$F_{hkl} = f_B \left\| 1 + \cos 2\pi \left(\frac{h+k+l}{4} \right) \right\| + \\ + 2f_A \left\| \cos 2\pi \left(\frac{1}{2} + \frac{h}{4} \right) + \cos 2\pi \left(\frac{h}{2} + \frac{k}{4} \right) + \cos 2\pi \left(\frac{k}{2} + \frac{1}{4} \right) \right\| \quad 9$$

where f_A and f_B represent the atomic scattering factor for A and B atoms lying on 6c and 2a sites, respectively. If deviations from perfect order or from ideal stoichiometry are introduced, the f_A and f_B for the atoms A and B have to be replaced by the effective:

$$f_a = r_a f_A + (1 - r_a) f_B \\ f_b = (1 - r_b) f_A + r_b f_B \quad 10$$

i.e. the formula A_3B is generalized to: $A_3B \rightarrow (A_{r_a}B_{1-r_a})(A_{1-r_b}B_{r_b})$ [18].

In the *Full Prof* software [33] used in the present work the structure factors are obtained with the following formula:

$$F_h = \sum_{j=1}^n O_j f_j(\mathbf{h}) \exp -B_j \|\mathbf{h}\|/4 \sum_{s=1}^m T_{js}(\mathbf{h}) \exp 2\pi i (\mathbf{h}^T S_s \mathbf{r}_j + \mathbf{h}^T \mathbf{t}_s) \quad 11$$

where n is the number of atoms in the asymmetric unit, m is the number of the reduced set of symmetry operators (centric lattice translation and inversion center operators removed), O_j (i.e. r_a, r_b in equation 10) is the occupation factor related to S with equation 1, $f_j(\mathbf{h})$ is the scattering length (in electron units for X-rays), B_j is the isotropic temperature parameter given (in \AA^2), and \mathbf{r}_j is the position vector of atom j. The symmetry operator $\{S_s | \mathbf{t}_s\}$ is applied to the scattering vector \mathbf{h} . \mathbf{h}^T is a row matrix with elements (hkl). The temperature factor $T_{js}(\mathbf{h})$ is given by:

$$T_{js}(\mathbf{h}) = \exp\{-\mathbf{h}^T S_s \beta_j S_s^T \mathbf{h}\} \quad 12$$

where β_j is the symmetrical matrix representing the anisotropic temperature parameters of the atom j [33].

In this study the temperature factor is isotropic and thus the parameters β_j should be set to zero.

1.2.3. The effect of disorder on T_c , B_{c2} and ρ_n

Since disorder affects the peak density of states⁴, many authors [35, 18, 10, 36, 9] studied the variations of the critical temperature T_c in terms of the degree of atomic order (i.e. Bragg-Williams LRO parameter S). Irradiation and rapid quench experiments [37, 38, 39] established that, for all typical A15-type superconductors, a decrease in S causes usually an important decrease of T_c . Appel [40] derived an expression for the electron-phonon interaction parameter $\lambda_{ep}(S)$ on the basis of the experimental dependence of the density of states $N(0)$ on S , obtained from specific heat measurements. He calculated the dependence of the critical temperature on the long range order parameter S using the McMillan formula [12].

The dependence of the normal state resistivity ρ_n on atomic order is due to the reduction of the mean free path l of the conduction electrons with increasing disorder.

The observed increase of B_{c2} can also be explained by the decrease of l , as shown by Gor'kov [41]. In the dirty limit, which is characterized by an electronic mean free path much smaller than the BCS coherence length ξ_0 , the Ginzburg-Landau parameter k can be expressed as a function of ρ_n :

$$k = k_0 + C\sqrt{\gamma}\rho_n \text{ for } l \ll \xi_0 \text{ with } C = 2.37 \times 10^6 \frac{Kg^{3/2}m^{5/2}}{KA^2s^4} \quad 13$$

In equation 13, which is known as the Gor'kov-Goodman relation, k_0 is the Ginzburg-Landau parameter of the pure material, and γ is the electronic specific heat coefficient. Due to the relationship:

$$B_{c2} = k\sqrt{2}B_c \quad 14$$

⁴ Crystallographic disorder, in which A and B atoms exchange positions, causes a decrease of the electronic density of states $N(0)$ [8].

the upper critical field exhibits an increase which primarily reflects the change in k given by equation 14.

1.3. Radiation damage and radiation effects in A15 superconductors

The interaction of high energy particles (protons, neutrons, electrons and heavy ions) with crystal lattices gives rise to microstructural defects that are referred to as **radiation damage**; the produced crystal defects modify the macroscopic properties of materials which are referred to as **radiation effects**. Radiation damage and radiation effects can be distinguished by their characteristic time scale: the primary events produced by irradiation occur in less than 10^{-11} s after the bombarding particle has interacted with the solid while the diffusion of defects take few milliseconds and the time scale of the nucleation and growth of voids by agglomeration of vacancies is of the order of months. In addition, while in the analysis of radiation damage the solid temperature can be neglected because the energies involved in the interaction of lattice atoms with projectiles are far above the thermal energy ($\sim kT$), in the study of radiation effects the kinetic of the migratory event is highly dependent on solid temperature which appears as a Boltzmann factor, $\exp(-E/kT)$ where E is the characteristic energy of a thermodynamic process.

In this section the main physical quantities used to quantify the radiation damage, to characterize the spatial arrangement of displaced atoms and the evolution of the damage cascade will be studied. The theoretical formulation adopted here follows that one used in the book by Gary S. Was [42].

In Chapter 5 the key concepts introduced hereafter will be evoked in the frame of FLUKA implementation to estimate the radiation damage induced on Nb_3Sn after proton and neutron irradiations and above all to obtain the displacement per atom (dpa) values. During the following description a particular attention will be given to the differences between the high energy radiation damage induced by proton and by neutrons. Finally, the effects on the A15 structure will be discussed on the basis of changes in the critical properties after high energy irradiation.

1.3.1. Radiation damage theory

The radiation damage event is defined as the transfer of the kinetic energy from an incident projectile to the solid and the resulting distribution of target atoms. It can be described as follows: when an energetic incident particle interacts with a lattice atom it transfers a kinetic energy, T , to the lattice atom giving rise to a *primary knock - on atom* (PKA). If T is higher than a threshold value (the *displacement energy*, E_d) the PKA is displaced from its lattice site. The displaced atom travels through the lattice encountering other lattice atoms and if such encounters involve sufficient energy transfer (at least equal to the displacement energy E_d) additional knock-on atoms are created resulting in the production of a displacement cascade. The radiation damage event is concluded when the PKA comes to rest in the lattice as an interstitial. The result of a radiation damage event is the creation of point defects (vacancies and interstitials, known as *Frenkel pairs*) and clusters of these defects in the crystal lattice, shown schematically in [Figure 8](#).

To estimate the radiation damage, the number of displacements per unit volume and per unit time, R_d , have to be calculated:

$$R_d \equiv \frac{\text{number of displacements}}{\text{cm}^3 \text{s}} = N \int_{E_{min}}^{E_{max}} \Phi(E_i) \sigma_D(E_i) dE_i \quad 15$$

where N is the lattice atom density, E_{max} and E_{min} are the maximum and minimum energy of the incoming particle respectively, $\Phi(E_i)$ is the energy dependent particle flux and $\sigma_D(E_i)$ is the energy dependent *displacement cross section*.

The displacement cross section is the probability for the displacement of lattice atoms by incident particles and is the key feature to quantify the radiation damage. It is given by:

$$\sigma_D(E_i) = \int_{T_{min}}^{T_{max}} \sigma(E_i, T) v(T) dT \quad 16$$

where T_{max} and T_{min} are the maximum and minimum energy transferred in a collision of a particle of energy E_i and a lattice atom respectively, $\sigma(E_i, T)$ is the probability (named the scattering cross section) that a particle of energy E_i will give a recoil energy T to the first atom it

encounters in the target, i.e. to the PKA, and $v(T)$ is the number of displaced atoms resulting from such collision.

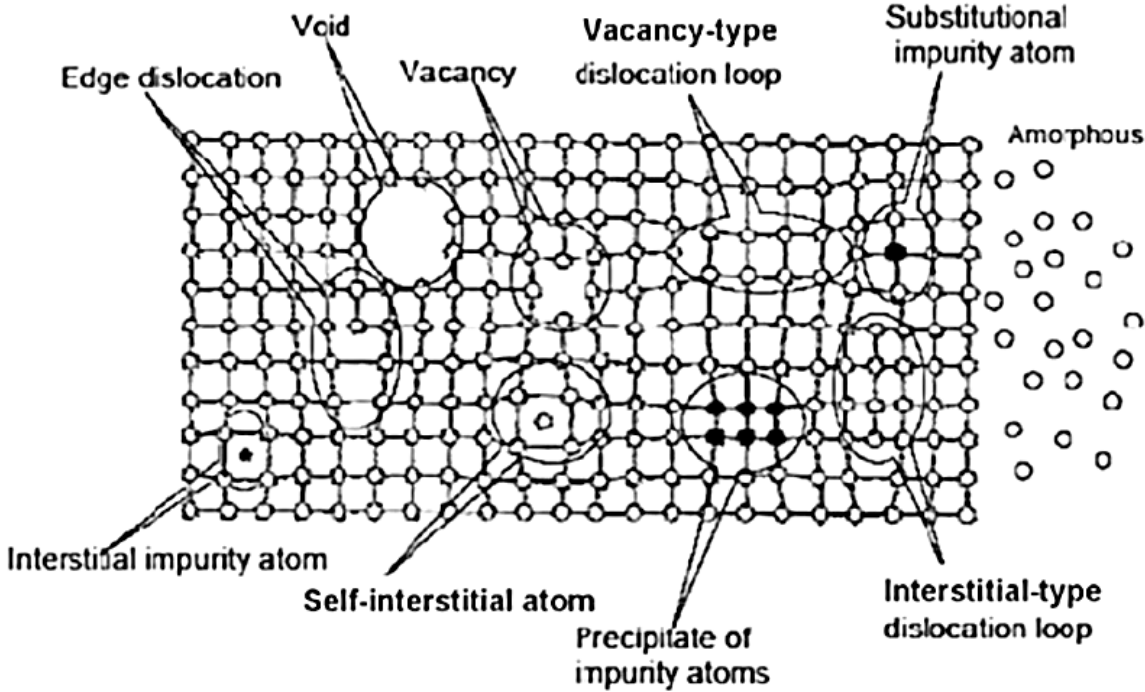


Figure 8 Most important radiation induced defects in a crystal lattice. The open dots belong to the original crystal, and the black dots indicate impurities. Self-interstitials, interstitial impurities and vacancies are point defects (zero-dimensional defects) while dislocation loop are line defects (one-dimensional defects). Voids are agglomeration of vacancies while precipitates are agglomeration of impurity atoms. All of these defects make the crystal lattice less flexible against strain, which manifests itself in a loss of ductility and an increase in hardness. In addition, the material becomes brittle and small cracks can develop, which may grow further, leading to the amorphization of the crystal lattice [43].

Quantification of the radiation damage

The scattering cross section, $\sigma(E_i, T)$, and the total number of displacements induced by the primary knock-on atom (PKA), $v(T)$, quantify the radiation damage. They describe the total number of displacements in the target from a flux of particles with a known energy distribution.

The scattering cross section $\sigma(E_i, T)$ contains the type of interaction between the projectile and the target atom. Depending on the nature of the projectile (charge, mass and energy) there are three types of mechanisms of interactions: *elastic* and *inelastic interactions* with nuclei and *electronic interaction* with the electron cloud of the atom. In elastic and inelastic interactions the

energy and momentum are transferred from the particle to the nucleus and the PKA moves in a partly ionized state through the lattice. In the elastic scattering, the nucleus is not transmuted and the interaction process is described

- for neutrons: by the hard sphere model from which the elastic scattering cross section, σ_s , is found to be independent from the recoil energy T , i.e. $\sigma_s(E_i) \propto (\gamma E_i)^{-1}$, where $\gamma = 4mM/(m+M)^2$ and the average recoil energy is $\langle T \rangle = \gamma E_i/2$.
- for low energy protons ($E_i \approx 1 \text{ MeV}$): by the Rutherford scattering and the elastic scattering cross section is a strong function of the recoil energy T , i.e.: $\sigma_s(E_i, T) = \frac{\pi b_0^2}{4} \frac{E_i \gamma}{T^2}$, where b_0 is the impact parameter and the average recoil energy is $\langle T \rangle \approx E_d \ln(\gamma E_i/T)$.

For high energy protons (several tens MeV and above): in addition to the elastic nuclear collision the contribution of inelastic nuclear collisions (secondary particles) start to count and the computation of the total scattering cross section is not straightforward.

In the inelastic scattering there is a loss of kinetic energy in the system and nuclear reactions lead to transmutation of the nucleus, which can become radioactive. The transmuted nucleus does not fit ideally into the lattice structure and therefore it changes the mechanical properties of the material, as reported by Kiselev [43].

It follows that in both the elastic and inelastic scattering, the PKA gains a recoil momentum; if the recoil energy exceeds the displacement energy, E_d , the atom can be displaced from its lattice site. As will be described in the next subsection, these interactions contribute to the nuclear stopping power or, in other words, to the non-ionizing energy losses (NIEL) and are responsible for the radiation damage in the materials.

Electronic interaction is due to the Coulomb scattering between the projectile and the electron cloud of the PKA, therefore it occurs only for charged particles (protons and ions). In this case the energy transfer by the projectile can shift the electrons from the atomic core to an outer shell (excitation) or can lead to the removal of an electron (ionization). These types of interaction contribute to the energy loss known as *electronic stopping power* and will lead to no permanent

radiation damage since damage in the electronic structure “anneals” spontaneously [44]. For further details see next subsection concerns the stopping power and Bragg peak.

The second quantity of interest to describe radiation damage is the *total number of displacements* that the PKA create in the solid, $v(T)$. Kinchin and Pease [45] developed a simple model from which the average number of displaced atoms in the cascade can be estimated as a function of the original PKA energy, T . In this theory it is stated that if $T < E_d$ then no displacement will take place ($v(T) = 0$) while if $E_d < T < 2E_d$, $v(T) = 1$; under the hypothesis that energy loss by electron stopping is given by a cut-off energy E_c ⁵, it follows that for $2E_d < T < E_c$, $v(T) = \frac{T}{2E_d}$. If the PKA energy $T > E_c$, no additional displacements occur until the electron energy losses reduce T to E_c . In this case the number of displacements is $v(T) = \frac{E_c}{2E_d}$.

However, the Kinchin and Pease model [45] overestimates the amount of displacements by a factor between 2 and 10 [46]. Indeed the energy transfer by a hard sphere model constitutes only an approximation. In addition it is supposed that the arrangement of the atoms in the solid is randomly distributed, neglecting the effects due to atomic vibration that are important to define the displacement energy E_d and above all the effects that arise from crystallinity as focusing and channeling are overlooked; both these processes can result in long-range transport of interstitials away from the initial PKA reducing the number of displacements per PKA as calculated from the simple Kinchin and Pease model [45]. Finally the condition that the cascade is created by a sequence of two-body collisions between atoms forbids that the cascade can be represented by displacement spikes, as will be described hereafter.

A more accurate estimation of $v(T)$ is given by Lindhard, Scharff and Schioett theory (LSS theory) [47]. In this theory, to ensure a reliable prediction of the total number of displacements generated by the PKA, they adopted a realistic energy transfer cross section instead of that one obtained by the hard-sphere model and, noting that in reality collisions of the PKA with atoms compete with collisions with electrons, they removed the quantity E_c introduced in the K-P model [45] and treated the two collision processes as independent events. Thus, according to Lindhard’s energy partitioning theory, the number of displaced atoms is:

⁵ This means that for all energies less than E_c electronic stopping is ignored and only atomic collisions occur.

$$v(T) = \xi(T) \left(\frac{T}{2E_d} \right) \quad 17$$

where $\xi(T) = \frac{1}{1 + 0.13(3.4\varepsilon_T^{1/6} + 0.4\varepsilon_T^{3/4} + \varepsilon_T)}$ is the damage energy efficiency function⁶, and ε_T is a reduced PKA energy given by: $\varepsilon_T = \frac{T}{2Z^2\varepsilon^2/a}$ (ε is the unit electronic charge and a is the screening radius). In 1975, Norgett, Robinson and Torrens [48] based on LSS model calculate the number of displacements per cascade, N_d , as a function of the *damage energy*, E_D , namely the energy available to generate atomic displacements by elastic collisions:

$$N_d = \frac{kE_D}{2E_d} = \frac{k(T - \eta)}{2E_d} \quad 18$$

where k is the displacement efficiency and it is equal to 0.8, T is the total energy of the PKA (or recoil energy of PKA) and η is the energy lost in the cascade by electronic excitation. It should be underlined that in the NRT approach [48] it is implicitly assumed that the defect concentration is equal to the calculated number of displacements and in addition the displacements formed are assumed to be stable.

The displacement per atom

At this point it is important to introduce another quantity that will be very useful in the present work to compare the radiation damage induced by protons and by neutron, i.e. the displacement per atom (dpa) (see Section 5.1 for further details). The dpa is a measure of the amount of radiation damage in irradiated material. The dpa rate is a derived quantity obtained dividing the number of displacements per unit volume and time, R_d given in equation 15, by the atomic density N of the material:

$$R_{dpa} = \frac{R_d}{N} = \int_{E_{min}}^{E_{max}} \Phi(E_i) \sigma_D(E_i) dE_i \quad 19$$

⁶ i.e. the fraction of the recoil energy left for the damage energy that is equal to the recoil energy minus the energy dissipated in ionization or excitation

where $\phi(E_i)$ is the fluence of the projectile and σ_D is the displacement cross section [49]. As reported by Schulson [50] the dpa represents the number of times each atom has been displaced and is given by:

$$dpa = N_d \sigma \Phi t \quad 20$$

where Φt is the fluence of projectile and σ is the scattering cross section.

Today J. F. Ziegler's computer code (SRIM) [51], implements stochastic methods and is widely used by scientists studying radiation damage in materials by ion accelerators. It allows quick calculations of the range of ions, the number of vacancies produced, the energy lost and several other parameters that are needed to plan and conduct ion beam experiment [46].

The damage cascade

In the models described above it was assumed that every created Frenkel pair was preserved and that no annihilation occurred; thus it is neither taken into account how the displaced atoms are arranged in the space (i.e. the volume of the *damage cascade*) nor the kind of evolution of the damage cascade with time to determine the actual number of defects that survive the displacement cascade (i.e. the *stable defects*).

In order to understand how the damaged region looks like, one needs to know whether the displacements are concentrated or distributed. Therefore two main features have to be taken into account: the *mean free path*, λ , and the *primary recoil spectrum*.

The *mean free path* λ for displacement collisions, i.e. collisions where the transferred energy is greater than E_d , is defined as:

$$\lambda = 1/N\sigma' \quad 21$$

where σ' is the cross section for the transfer of energy in excess of E_d , given in terms of the differential energy transfer cross section between lattice atoms. It follows from equation 21 that as the energy of the moving atom drops, the cross section increases slowly but the mean free

path becomes very small at energies just above E_d approaching to the atomic spacing at which point each atom along the recoil path is displaced.

The second quantity, the *primary recoil spectrum*, gives a measure of the density of displacement damage in the target and it is defined as the density of recoil atoms with energies between T and $T + dT$ induced by radiation:

$$P(E_i, T) = \frac{1}{N} \int_{E_d}^T \sigma(E_i, T') dT' \quad 22$$

where N is the total number of the primary recoils and $\sigma(E_i, T)$, the energy transfer cross section of a particle of energy E_i to create a recoil of energy T . Anyway for defect production, it is more important to define the fraction of damage energy that is produced in recoils of a particular energy. This quantity is given by “weighting” the recoil spectra by the number of defects or by the damage energy produced in each recoil, thus:

$$W(E_i, T) = \frac{1}{E_D(E_i)} \int_{E_d}^T \sigma(E_i, T') E_D(T') dT' \quad 23$$

where $E_D(T)$ is the damage energy created by a recoil atom of energy T .

Finally, to determine the defects that survive the displacement cascade the evolution with time of the damage cascade has to be considered.

As shown in [Figure 9](#), the development of the damage cascade with time can be divided in four stages: collisional, thermal spike, quench, annealing. During the first stage (less than 1 ps), i.e. the *collisional stage*, the PKA initiates a cascade of collisions until the atom energy is too low to create further displacements: the damage consists of energetic displaced atoms and vacant lattice sites, as discussed in the previous subsections. In the second stage, i.e. the *thermal spike stage*, the collisional energy of the displaced atoms is shared among their neighboring atoms in a very short period (about 0.1 ps) leading to local “melting”. The third stage, i.e. the *quenched stage*, lasts several ps and consists in the transfer of the energy to the surrounding atoms; as a consequence, the melted zones return to the condensed phase and stable lattice defects form, either as point defects or as defect clusters⁷. Finally, the *annealing stage* involves further

⁷ Note that the total number of defects at this stage is much smaller than the number of atoms displaced in the collisional stage.

rearrangement and interaction of defects and occurs by thermally activated diffusion of mobile lattice defects. By definition, the annealing stage continues until all mobile defects escape the cascade region or another cascade occurs within it and the timescale extends from nanoseconds to months, depending on the temperature and the irradiation conditions. Consequently, the final stage of the radiation damage evolution represents the link between the damage cascade (*radiation damage*) and the observable effects of irradiation (*radiation effects*).

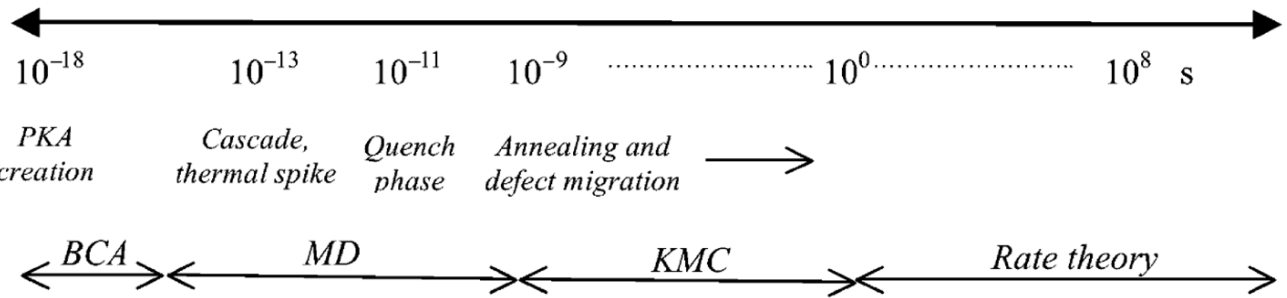


Figure 9 Time-scale for radiation damage evolution and the corresponding simulation methodology [42].

Experimentally it is possible to observe defect clusters by means of Transmission Electron Microscopy (TEM), X-ray scattering, small angle neutron scattering and positron annihilation spectroscopy [44]. However the resolution of these techniques does not allow capturing the temporal development of the cascade. Therefore computer simulations have to be adopted to achieve a better understanding of the spatial and temporal development of the cascade. Three techniques are commonly used to model the behavior of atoms in a displacement cascade: the binary collision approximation (BCA) method, the molecular dynamics (MD) method and the kinetic Monte Carlo (KMC) method.

In the present work a fully integrated Monte Carlo simulation package for the interaction and transport of particles and nuclei in matter, FLUKA (FLUktuierende KAskade), is used to estimate the radiation damage induced by protons on bulk Nb_3Sn platelets; further details on this code will be given in Chapter 5.

The diffusion mechanisms in irradiated A15 alloyed

As discussed by Flükiger [18], the diffusion in the irradiated A15 compounds is not a single vacancy diffusion⁸ mechanism due to the non-equivalence of electronic bonding of the 6c and 2a sites: the intrachain bonding between atoms on the 6c and on the 2a sites is of the metallic type while between two A nearest neighbors is of the covalent type (Staudenmann [52, 53]) and such covalent bonding is called “*overlapping region*”.

To describe the diffusion mechanism leading to a homogeneous disordering in irradiated A15 type compounds Flükiger [18] has adopted two main concepts:

- the “virtual site” previously introduced by Welch et al. [54, 55]. By means of pair potential calculations they found that the vacancy of an A atom on a 6c site is unstable and the state of lower energy corresponds to a configuration where one of the two A atoms adjacent to the single 6c vacancy is shifted towards a new site in the “*overlapping region*” which is equidistant from the next two A neighbors. This type of “*split vacancy*” [54, 55] corresponds to a non-equilibrium state thus it is called “*virtual lattice site*” by Flükiger [18, 29].
- the “focused replacement collision sequence”, i.e. the transport of matter and energy in irradiated crystals along dense crystallographic directions (Seeger [56, 57]). Regardless of the crystal structure, an interstitial atom produced by irradiation is transported several interatomic distances away from its associated Frenkel vacancy, along these “focalizing” crystallographic directions⁹

In the unirradiated state the only focusing direction where collision sequences could in principle produce A↔B site exchanges, is the <102> direction (oABAoABAo). Due to the smaller Born-Mayer interatomic potential [58] $V_{A \rightarrow B} = V_{B \rightarrow A}$ (~ 10 eV) with respect to $V_{A \rightarrow A}$ (~ 52 eV) the <102> direction excludes extended site exchanges before irradiation.

⁸ At thermal equilibrium each solid contains a certain number of vacant lattice sites. During the damage cascade a PKA has a high probability to jump into a neighboring vacancy creating, in turn, a new vacant site. As result, a very small number of vacant lattice sites is sufficient to induce a substantial diffusion [15].

⁹ A necessary condition for the occurrence of *focused replacement collision sequences* consists in the occupation of a sufficient but still small number (<0.1%) of “virtual sites”.

After irradiation, the number of occupied “*virtual sites*” increases lowering the potential $V_{A \rightarrow A}$. During the whole irradiation time the “*virtual sites*” will be many times occupied and abandoned again and, depending on the occupation of the “*virtual site*” by an A or a B atom, the new sequence of atoms in the focalizing $\langle 102 \rangle$ direction around the occupied “*virtual site*” can be oABAABAAoABAo or oABABABA0ABAo, respectively (see [Figure 10](#)).

Thus the “*virtual sites*” constitute a connection between neighboring ABA sequences allowing $A \leftrightarrow B$ exchanges over several interatomic distances and it is the necessary condition for a homogeneous decrease of the LRO over the whole crystal after irradiation at low temperatures [18]. At the same time, thermal reordering will occur, as follows from the recombination theory by Liou and Wilkes [59].

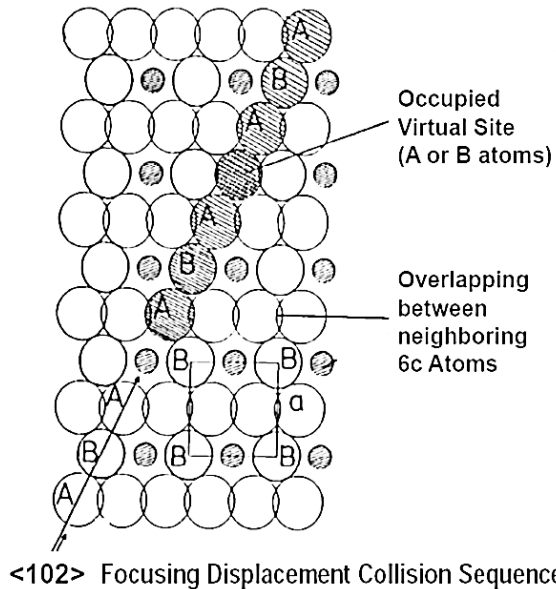


Figure 10 Focusing replacement collision sequences in $\{100\}$ plane of the A15 lattice. The small circles correspond to the overlapping region between two A atoms belonging to the chains perpendicular to the $\{100\}$ plane. The occupation of the “*virtual site*” by an A or a B atom leads to the sequences oABAABAAo or oABABABAo, respectively instead of oABAoABAo as in the unirradiated case, thus enabling $A \leftrightarrow B$ site exchanges in the $\langle 102 \rangle$ direction [18, 29].

1.3.2. Differences in the radiation damage induced by protons and by neutrons

One of the main tasks of the present work consists in comparing the damage induced by protons and neutrons. In this subsection the differences in the radiation damage induced by these two

particle types will be explained theoretically. These theoretical concepts will be recalled in Subsections 4.1.4 and 5.3.1 to explain why the same effects on J_c and T_c can be observed at proton fluences one order of magnitude lower than neutron fluences

The stopping power and the Bragg peak

As described above, both charged and uncharged particles traveling inside the matter lose their energy due to the different types of interactions with the lattice (elastic, inelastic or electronic scattering). The stopping power, $NS(E)$ (where N is the atom number density and S is the stopping power in units of energy times distance squared), refers only to the energy loss of charged particles and depends of course on the type and energy of the projectile as well as on the properties of the material it passes. It is defined as the energy loss per unit length, $-dE/dx$ (or $NS(E)$) and is given, in first approximation¹⁰, by the sum of two components:

$$NS(E) = \left(-\frac{dE}{dx}\right)_{tot} = \left(-\frac{dE}{dx}\right)_n + \left(-\frac{dE}{dx}\right)_e \quad 24$$

where $\left(-\frac{dE}{dx}\right)_n = S_n$ is the nuclear stopping power due to the elastic collisions between the charged particles with the nuclei in the target and $\left(-\frac{dE}{dx}\right)_e = S_e$ is the electronic stopping power that refers to the slowing down of a projectile ion due to the inelastic collisions between electron cloud in the medium and the charged particle moving through it.

The total distance that a projectile of initial energy E_i will travel before coming to rest is called the average total range, R , and is a convenient quantity for estimating the average penetration depth. It is given by integrating the reciprocal stopping power over the energy:

$$R = \frac{1}{N} \int_0^{E_i} \frac{dE}{[S_n(E) + S_e(E)]} \quad 25$$

In order to accurately describe the slowing down of a charged particle over the entire energy range from T_{max} to T_{min} , where T_{max} may be in MeV and $T_{min} \sim 10$ eV, the different

¹⁰ At very high energies, one has to consider in addition the radiative stopping power, which is due to the emission of bremsstrahlung in the electric field of the nuclei of the material traversed.

interaction potential functions have to be taken into account. As a result, the stopping power can be characterized according to the type of interaction and hence, according to the energy regime.

As shown in [Figure 11](#), in the high-energy regime, ($\rho \ll a$, where ρ is the distance between atom centers in the collision and a is the screening radius) the electronic stopping power prevails on nuclear stopping power, i.e. $S_e \gg S_n$ so the path follows by the projectile during its slowing down is essentially a straight line and the interactions are treated as pure Coulomb collisions; this is in contrast to the low energy regime, ($\rho \approx a$) where $S_n > S_e$ and the path of the charged particle follows a zigzag course with many large deflections, while the distance between collisions decreases as the energy decreases and the cross section increases. As will be explained hereafter, the low energy regime is the region of importance to estimate the radiation damage induced on the crystallographic structure.

Once the energy transfer cross section $\sigma(E_i, T)$ is known for either S_n or S_e , the average energy

$$\text{transfer is given by: } \langle T \rangle = \frac{\int_{T_{min}}^{T_{max}} T \sigma(E_i, T) dT}{\int_{T_{min}}^{T_{max}} \sigma(E_i, T) dT}.$$

The energy loss per unit length, or total stopping power $NS(E)$, will be given then by the ratio of $\langle T \rangle$ and of the mean free path between collisions, λ , i.e.:

$$NS(E) = -\frac{dE}{dx} = \frac{\langle T \rangle}{\lambda} = N \int_{T_{min}}^{T_{max}} T \sigma(E_i, T) dT. \quad 26$$

From a phenomenological point of view the slowing down of charged particle inside the matter can be described as follows: when a fast charged particle travels through the lattice, it ionizes atoms of the material and deposits a dose along its path due primarily to the electronic stopping power (as explained in [Figure 11](#) this is the high-energy regime, ($\rho \ll a$, $S_e \gg S_n$)). As the energy of the charged particle decreases the collisions with nuclei become more probable (i.e. the interaction cross section rises) and consequently from equation 26 follows that the total stopping power increases up to the formation of a peak in the energy deposition. This peak is called the *Bragg peak* after William Henry Bragg who discovered it in 1903; it occurs immediately before the particles come to rest.

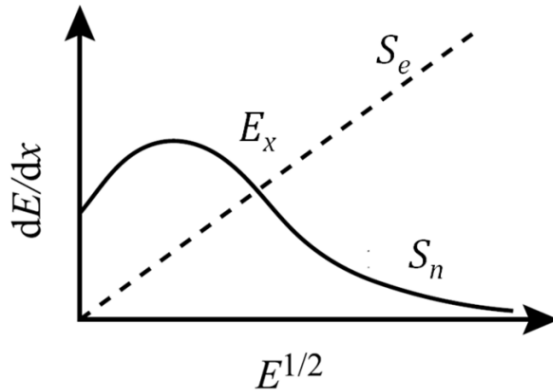


Figure 11 Energy loss from electronic and nuclear stopping as a function of energy (from G. S. Was [42]). At low energies ($T < 10^3$ eV) there is $S_n \gg S_e$, and we may assume that nearly all of the energy loss of the PKA goes toward nuclear collisions. However, as the PKA energy increases, the fraction of the total energy loss due to electron excitation and ionization increases until above the crossover energy, E_x , $S_e > S_n$.

In Figure 12 the energy deposition per unit length for 20 MeV protons in Nb_3Sn determined in this work by FLUKA simulation (see Chapter 5) is plotted against the penetration depth; in the plateau region that precedes the peak, the charged particle loses energy mainly by ionization of the target atoms. The recombination process will then restore the charge neutrality of the solid lattice.

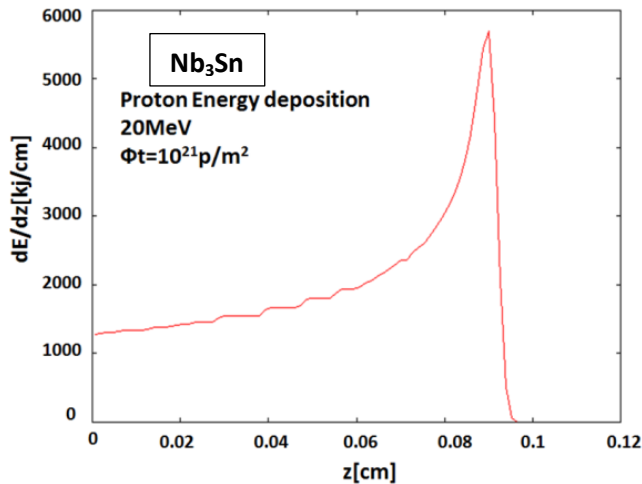


Figure 12 FLUKA simulation of total stopping power (Bragg curve) for 20MeV proton irradiation on Nb_3Sn at a fluence of 10^{21} p/m^2 . The energy loss per unit length is plotted against the penetration depth of the particle. As the projectile slows down, the stopping power increases leading to the formation of a peak in energy deposition, called the Bragg peak (this work).

As shown in [Figure 13](#), for energies in the MeV range, the nuclear stopping for protons in solids is about a factor 10^{-3} smaller than the electronic stopping but becomes important at low energy.

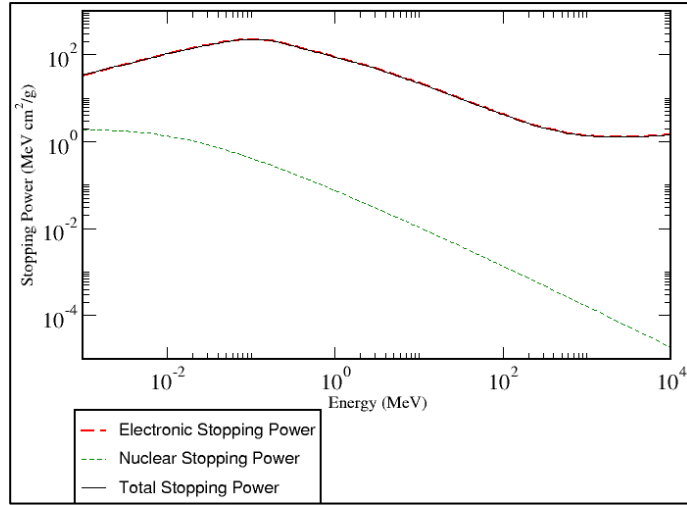


Figure 13 Electronic and nuclear stopping power for Tin after proton irradiation calculated using PSTAR program [60]

Therefore the nuclear stopping contributes to the very end of the stopping curve, as shown in [Figure 14](#), reflecting that near the Bragg peak the energy transferred to the target is able to cause a permanent disruption of the target lattice.

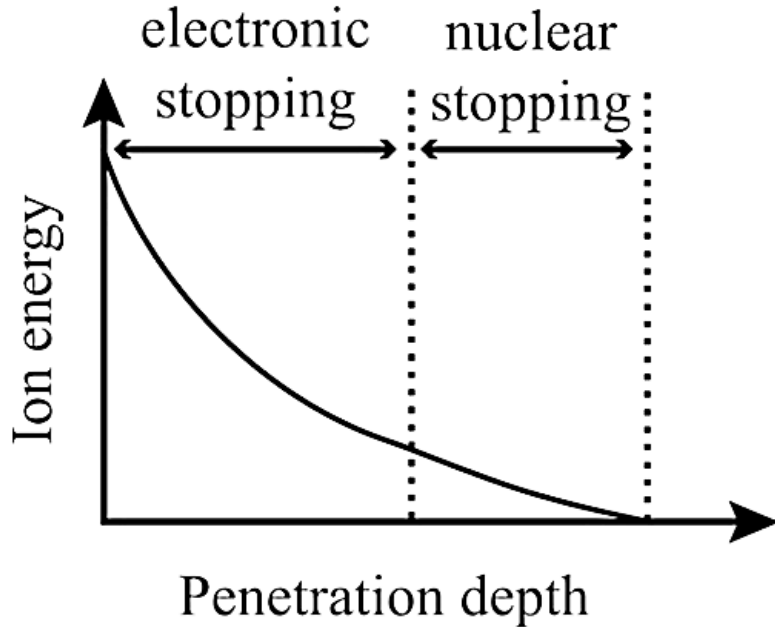


Figure 14 Regimes of electronic and nuclear stopping dominance. After G. Was [42].

Comparison between neutron and proton irradiation

To describe the major differences between proton and neutron irradiation the displacement cross section is compared to the energy of the particle responsible for the damage. The displacement cross-sections for protons and neutrons in copper obtained by two different approaches are reported in [Figure 15](#): the NRT model and a combination of the MDS and BCA methods [61]. As follows from the comparison in [Figure 15](#), the displacement cross-sections for the two types of projectiles strongly vary with energy:

- at small energies, the cross-sections for protons are given by Coulomb interaction while for neutrons they are due to the large capture cross-section;
- at high energies, the two displacement cross-sections are quite similar in size and shape. Above the so-called pion threshold (about 290 MeV) they are almost constant due to the total inelastic scattering cross-section which shows the same behavior for the two particles.

The increase in the proton displacement cross-section at smaller energies is due to the large elastic scattering cross-section, which means that the particle uses its energy most efficiently to displace atoms and not for the release of secondary particles as it happens in the inelastic case; it follows that proton damage is stronger at low energies than at high energies. This conclusion is important for the analysis of the results obtained in the present work.

Voronova and coworkers [62], studied the changes of the critical current density, J_c , of Nb_3Sn samples after irradiation with protons, α particles and fission fragments and found that the maximum value of J_c is reached for proton fluence around $5 \times 10^{20} \text{ p/m}^2$. Comparing this result with neutron irradiation data by Küpfer et al. [63], Weiss et al. [64], Sekula [65] and Bauer et al. [66] they noted that the proton fluence at which the maximum in J_c is reached is about two orders of magnitude lower than the neutron fluence. Voronova et al. [62] concluded that the difference between these magnitudes can be assigned to the difference in the cross-section for the creation of recoil atoms with a sufficient energy to form defects which in turn can effectively pin a vortex.

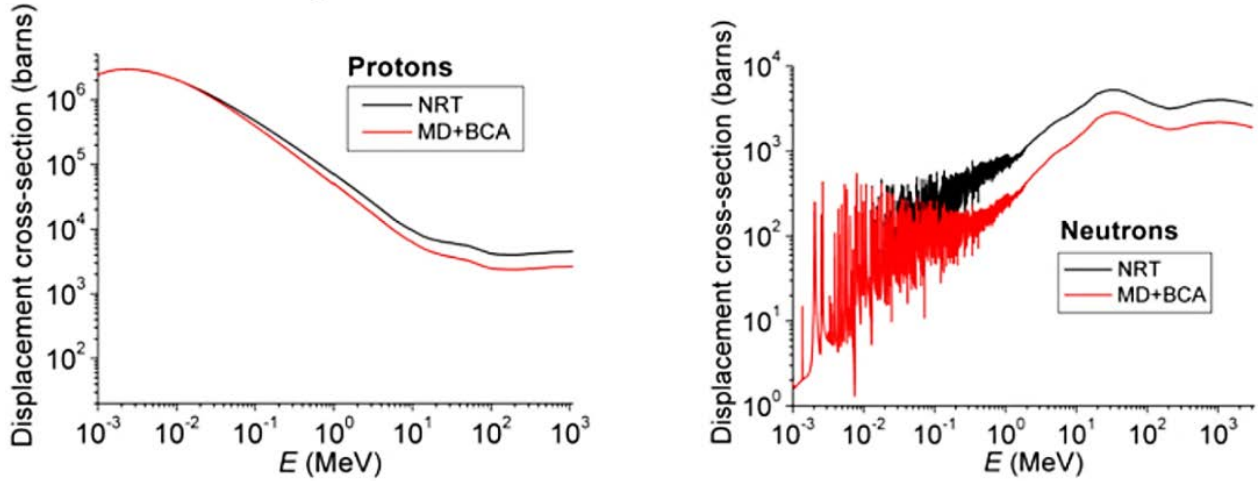


Figure 15 Displacement cross-sections of protons (left) and neutrons (right) in copper obtained by two different approaches (NRT and MD+BCA methods) [61].

Another difference between proton and neutron irradiation is the loss of their energies inside the matter which is associated to their different scattering cross-sections (i.e. their different type of interactions with the PKA). The decrease of proton energy is very fast due to the electronic interaction with the electron cloud of the target atom giving rise to a spatially non-uniform energy deposition profile (the *Bragg curve*); on the other hand, neutrons can produce spatially flat damage profiles due to their electrical neutrality. As a result the penetration depth (or *range*) for protons is shorter than for neutrons, as shown by FLUKA simulation performed in this work for Nb_3Sn in Figure 16.

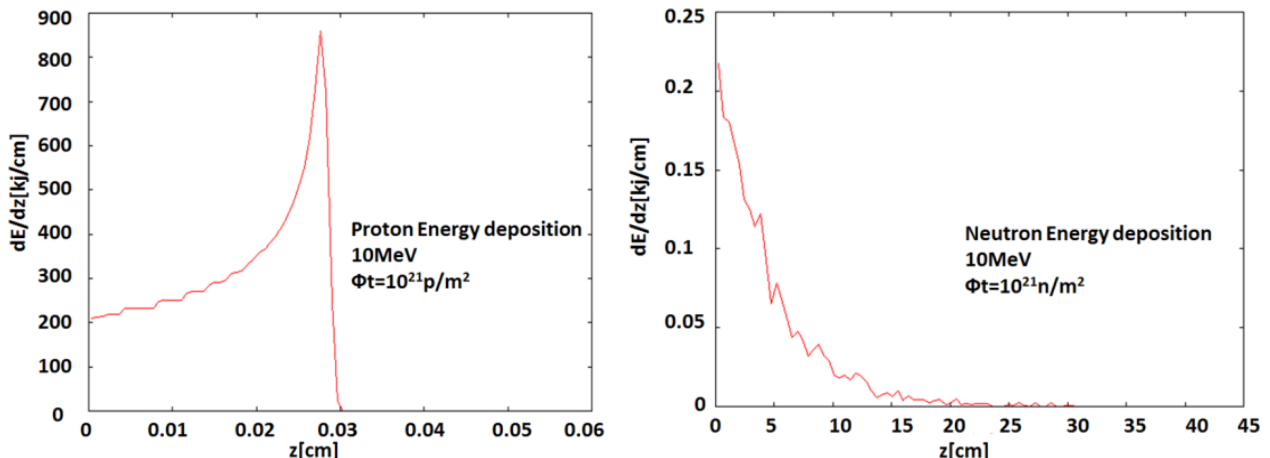


Figure 16 FLUKA simulations of the penetration depth for protons (left) and for neutrons (right) in Nb_3Sn . Note the difference in penetration depth (this work).

As reported in [Figure 17](#), the weighted average recoil spectrum, $W(E_i, T)$, described in equation 23 is characterized as follows:

- for protons: by a slow increase with energy since the Coulomb forces slowly increase as the particle approaches the target;
- for neutrons: it exhibits a delta function shape as a consequence of the hard-sphere interaction where particles and target do not feel each other until their separation reaches the hard-sphere radius, the repulsive force tending to infinity.

The result is that Coulomb interactions tend to create many PKAs with low energy while hard-sphere collisions create fewer PKAs but with higher energy.

Finally, as reported by Was and Allen [67], the damage morphology and displacement efficiency, ϵ reflect the higher damage induced by protons. Indeed neutrons produce dense cascades with a high value of the average transferred recoil energy, \bar{T} , resulting in substantial recombination during cooling or quenching phase and thus give a displacement efficiency of only 2% while protons produce small widely spaced cascades with low value of \bar{T} and many isolated Frenkel pairs that do not recombine yielding a higher displacement efficiency (25%).

Bode and Wohlleben in 1966 [68], analyzed the question whether small clusters induced by charged particle irradiation were able to act as pinning centers as it was the case for clusters with larger diameters produced after neutron irradiation. They studied the changes in the critical current density J_c after proton irradiation on Nb_3Sn layer and compared their results with neutron experiments performed by Cullen et al. [69]. They found that the fluence to create the same number of pinning centers was about two orders of magnitude higher for neutrons than for protons. They calculated the ratio between the number of incident protons and neutrons for the same enhancement of J_c and found $N_p/N_n = 3 \div 6 \times 10^{-2}$, thus indicating a markedly larger damage for protons.

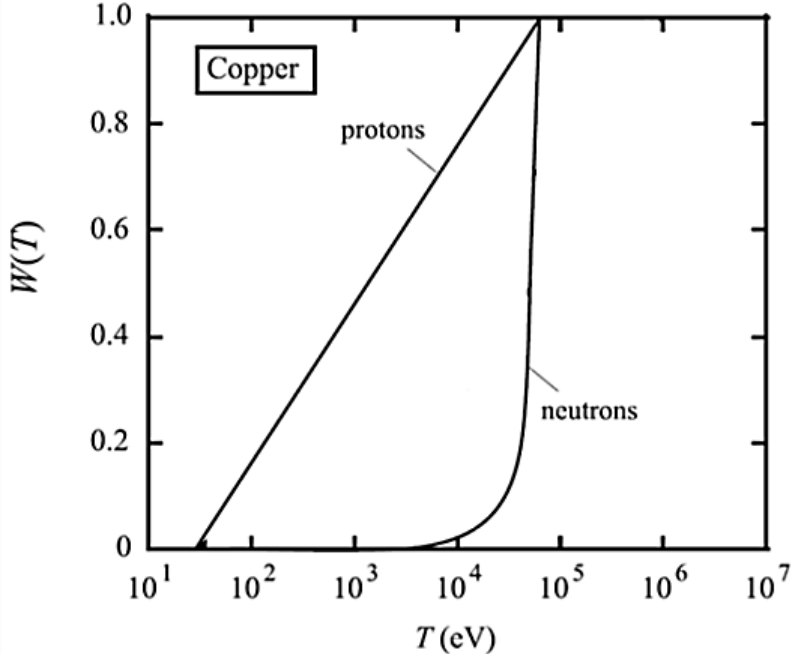


Figure 17 Weighted recoil spectra versus recoil energy for 1MeV protons and 1MeV neutrons irradiation in copper [42].

1.3.3. Radiation effects in superconductors

A large number of publications on the effects of radiation damage in superconductors has been published since 1970, the projectiles being protons, neutrons and heavy ions. All these irradiation types were found to induce a certain amount of disorder in the A15 phase, depending on the projectile. As a result the critical properties (T_c , J_c and B_{c2}) change, the lattice parameter increases, the electronic specific heat decreases and the electrical resistivity is enhanced. A flowchart of the effects of high energy radiation on A15 type compounds is reported in [Figure 18](#) [18].

Aronin [70] proposed an exponential function to describe the decrease of the Bragg Williams long range order parameter S with increasing fast neutron fluence, ϕt :

$$S(\phi t) = S(0)e^{-k\phi t} \quad 27$$

In equation 27, the factor $S(0)$ is the S value before irradiation, and k is a constant which depends on the material. Since increasing particle fluence causes a decrease of S , the mean free path l of the electrons will decrease (see also Subsection 1.2.3).

In the following an overview of the main changes induced by high energy proton and neutron irradiation on the intrinsic properties of A15 superconductors, especially for Nb_3Sn , will be given and the physical reason behind these changes will be discussed.

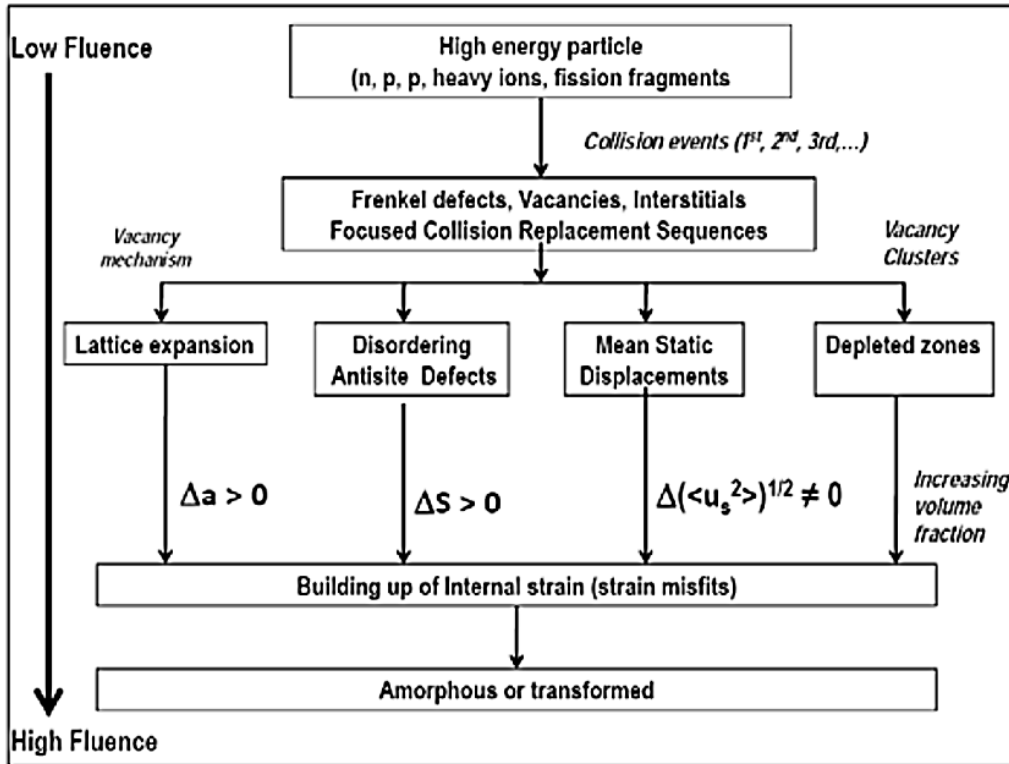


Figure 18 Schematic representation of the radiation induced effects in A15 type compounds, with increasing fluence. Extracted from Ref. [18].

Changes in T_c after irradiation

In 1974 Bett [71] reported a gradual decrease of T_c in Nb_3Sn up to a fast neutron fluence of about $2 \times 10^{23} \text{ n/m}^2$. Weiss et al. [64] found that the variation of T_c at low fluences is linear for both binary and alloyed wires: the T_c reduction is close to 4% for 14MeV neutron fluences up to 10^{22} n/m^2 and reaches about 20% for higher fluences. At the highest fluences, i.e. $4 \times 10^{22} \text{ n/m}^2$, they found that the variation ΔT for alloyed wires (- 2.9 K for Ti additions and -3.3 K for Ta additions) was slightly higher than for binary wires varies (from -2.3 to -2.6 K). As shown recently by Flükiger et al. [20], the fact that Ta and Ti occupy different lattice sites before

irradiation (Ta on Nb sites, Ti on Sn sites) may give an explanation for the observed difference in the decrease of T_c for the two types of alloyed Nb₃Sn wires. The decrease of T_c in multifilamentary Nb₃Sn wires was also observed by Hahn [72], who found for 14.8 MeV neutron irradiation an exponential fit of the form:

$$T_c(\phi t) = T_{c0} e^{-k\phi t} \quad 28$$

where T_{c0} is the critical temperature before irradiation and k is a fit parameter with values between 0.062 and 0.082 for binary wires and between 0.081 and 0.098 for alloyed wires up to a fluence of $\sim 10^{22}$ n/m². Due to the small value of k the exponential dependence of T_c with fluence given in equation 28 is almost linear at not too high fluences, in agreement with the results found by Bett et al. [71] and Weiss et al. [73].

The debate on the defect mechanisms responsible for the decrease of T_c is very complex and the question on how the radiation damage affects the critical temperature remains still open. Four main candidates are used in literature to explain the degradation of T_c with fluence, i.e.:

1) Decrease of the atomic order parameter S due to site exchanges (“antisite defects”)

The Bragg Williams LRO parameter, S , defined in Subsection 1.2.2 is a function of the occupation number and of Sn composition. Appel [40] provided a detailed theory on a uniform distribution of site exchanges in irradiated compounds based on McMillan theory [12] (strong coupling theory), the electron-phonon interaction parameter $\lambda(S)$ in his theory being a function of the long-range order parameter. A decrease of S in irradiated A15 compounds was observed in Nb₃Al by Sweedler et al. [39], in Nb₃Pt by Moehlecke et al. [74] and in V₃Si by Cox and Tarvin [75]. A homogeneous distribution of the damage in A15 type compounds was also proven on the basis of low temperature specific heat measurements before and after irradiation. Viswanathan et al. [76, 77] and Cort et al. [78] found that the superconducting transition widths of the A15 type compounds V₃Si and Nb₃Al remain narrow after neutron irradiation (≥ 1 MeV). In particular for Nb₃Al, the width of the specific heat jump, ΔT_c , increases from 0.8 K in the unirradiated state to 1.3 K after 1.3×10^{23} n/m², where the T_c/T_{c0} is equal to 0.51; for V₃Si, an increase of ΔT_c from 0.5 to 1.2 K was observed after 2.22×10^{23} n/m², where $T_c/T_{c0} = 0.4$. In both cases there is thus still a high degree of homogeneity in the LRO

parameter S . This is analogous to the case of fast quenching of A15 type compounds, where the total gradient across the sample is only $\delta S \leq 0.02$, as shown by Flükiger [18]. From X - ray diffractometry, Sweedler et al. [79] found an exponential dependence of the critical temperature of Nb_3Sn on S :

$$T_c(\phi t) = T_{c0} e^{-C(1-S/S(0))} \quad 29$$

assuming an initial value for long range order parameter $S(0) = 1$ (the experimental proof for perfect ordering in Nb_3Sn is given in the present work, see Section 4.2), they found a value of 5.0 ± 1.5 for the constant C and concluded that the decrease of T_c at doses up to 10^{23} n/m^2 (where $T_c/T_{c0} \sim 0.5$) is mainly caused by a decrease of the long-range atomic order parameter, S [79, 80].

2) The formation of depleted zones (inhomogeneous disorder)

By means of TEM analysis of neutron irradiated Nb_3Sn bronze wires, Pande [81] observed in 1977 small “disordered micro-region” of about 4 nm size, embedded in a much less disordered matrix. Since the critical temperature of these disordered regions was significantly lower than that of the matrix Pande [81] concluded that the critical temperature of the system would be strongly depressed due to the proximity effect. Consequently he suggested an inhomogeneous disorder after irradiation. However calorimetric measurements [76, 77] constitute a definitive proof for the validity of the homogeneous disordering model proposed by Sweedler et al. [82, 80]. This will be discussed in detail in the following.

3) The increase of the mean static displacements of atoms, u

Meyer et al. [83] and Testardi et al. [84] observed an increase of the mean static displacements of atoms after heavy irradiation of V_3Si single crystals by means of the channeling technique. Earlier to these observations, a weakening of the X – ray line intensities at high 2θ angles had been observed by Testardi et al. [85] and Poate et al. [86] on irradiated Nb_3Ge and Nb_3Sn . This weakening could neither be accounted for by a lowering of the LRO parameter nor by a particular choice of the temperature factor: it was found to be related to static displacements of the chain atoms from their ideal lattice

sites. Later on, the same authors determined the quantity u by means of X – ray diffraction measurements [87, 88]. After their first detection, the static displacements were invoked as being the main responsible for the initial decrease of T_c after high energy irradiation [84, 89]. Schneider et al. [88] found, however, that after proton irradiations the displacements were substantially different from zero after higher doses only. After Schneider [88] various studies were performed to clarify the correlation between the decrease of T_c and the increase of u [80, 83, 84, 90]. However since the same value of T_c correspond to very different values of u , this indicates that static displacements, which occur simultaneously to atomic site exchanges, are not the dominant factor causing the initial decrease of T_c in high T_c A15 type compounds [18].

4) The mechanical effects (stress - strain effects)

Radiation hardening of the Cu matrix after irradiation induce a pre-stress on Nb_3Sn matrix, and can thus lead to a reduction of T_c . Okada et al. [91] have experimentally found that after neutron irradiation up to $3.6 \times 10^{23} \text{ n/m}^2$ the enhancement of the pre-strain ε is about 0.2 %. However, the fluences corresponding to the maximum of J_c after neutron irradiation are about one order of magnitude smaller, which would lead to an enhancement $\Delta\varepsilon$ of 0.02 % only. It follows that up to these fluences the effect on the pre-strain is almost negligible. This is confirmed by the first principles calculations by De Marzi and coworkers [92], who found that, the variation of T_c is very small: about 0.05 K. Thus at low fluences, i.e. up to values corresponding to J_c/J_{cmax} , the additional effect of the radiation induced pre-strain on T_c can be neglected.

As will be explained in the following, the homogeneous decrease of S is the main responsible for the observed decrease of T_c up to radiation doses of $\sim 10^{23} \text{ n/m}^2$, while inhomogeneous defects, mean static displacement and mechanical effects are dominant for higher doses only, where the value of T_c is too low for being of interest for the present work.

Two main arguments can be invoked for proving the validity of antisite defects as the dominant mechanism [18]:

- a. Homogeneous distribution of antisite defects after irradiation detected by specific heat measurements.

The question about a homogeneous distribution of the damage can be answered on the basis of the known low temperature specific heat measurements before and after irradiation for the A15 type compounds Nb_3Sn by Karkin et al. [93], Nb_3Al by Cort et al. [94] and V_3Si by Viswanathan et al. [76]. For the three systems, heavy neutron irradiations up to fluences of $2 \times 10^{23} \text{ n/m}^2$ causes a very small enhancement of the transition width, ΔT_c , i.e. for a neutron fluence reducing T_c to about 50% of the initial value, the transition width ΔT_c is only enhanced by $\leq 1\text{K}$. In addition in the specific heat curves, there is no trace of the original superconducting transition temperature, T_{c0} , in any of the three systems after irradiation. This implies that the amount of depleted zones (with considerably lower T_c) is very small and cannot account for the observed decrease of the superstructure lines, i.e. indirectly that the damage is homogeneous up to 10^{23} n/m^2 .

- b. Comparison between the variation of T_c vs. the order parameter S after irradiation and after fast quenching by diffraction methods.

No direct comparison between neutron irradiation and quenching has been performed on Nb_3Sn and the data reported here concern the system Nb_3Pt , another A15 type compound. Figure 19 shows the variation of T_c for Nb_3Pt vs. the long range order parameter, S, after fast quenching from temperatures up to $1900 \text{ }^\circ\text{C}$ by Flükiger et al. [95] and after neutron irradiation ($E > 1 \text{ MeV}$) by Moehlecke et al. [96]. It follows from Figure 19 that the variation of T_c vs S is the same, regardless whether the compound was fast quenched or irradiated. Since quench induced disordering constitutes a particularly simple case, where the only possible defects are the antisite defects (up to a few %) and quenched-in vacancies ($\leq 0.02 \text{ \%}$ at 300 K), the same behavior found after quenching and after irradiation constitutes an additional argument in favor of the antisite defects mechanism for the observed decrease of T_c after irradiation up to fluences of 10^{23} n/m^2 .

Changes in B_{c2} and J_c after irradiation

Weiss et al. [64] found that after high energy irradiation the upper critical field increases up to 10^{22} n/m² and then decreases at higher fluences. The reason for the increase of B_{c2} with fluence can be explained by the increase of the residual electrical resistivity, ρ_0 . Indeed, Alterovitz et al. [97] observed that after irradiation of V₃Si bulk sample by 35 MeV protons at fluences up to 10^{21} p/m² the enhancement of ρ_0 (due to the decrease of the electronic mean free path) prevails on the decrease of T_c , thus the increase of B_{c2} follows the trend of ρ_0 . At higher fluences the tendency of ρ_0 and T_c with fluence is reversed and it is suggested that the decrease of B_{c2} at fluences beyond those corresponding to the maximum of J_c/J_{c0} is mainly due to the degradation of T_c .

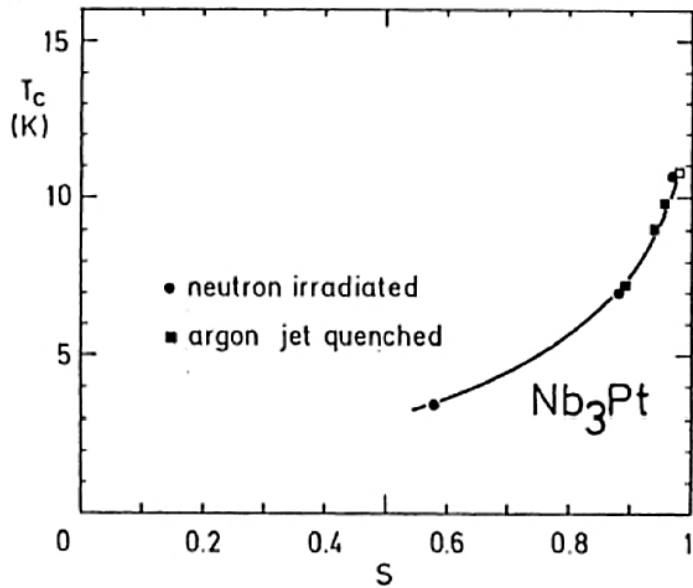


Figure 19 T_c vs. long-range order parameter S (determined by X ray diffraction) for Nb₃Pt after fast quenching from different temperatures (Flükiger et al. [95]) and after neutron irradiation (Moehlecke et al. [96]).

An analogous behavior of the critical current density with fluence was found by many authors and the existence of the maximum in J_c at which the maximum of B_{c2} occurs at almost the same fluence suggests that the enhancement in J_c was correlated to that one of B_{c2} [98, 73]. Later on, however, it has been shown by Küpfer et al. [63] that after high energy irradiation the change in B_{c2} is not the main reason for the enhancement of J_c , at least at low fluences when both these parameters increase. Indeed, these authors found that the enhancement of J_c after neutron

irradiation [99, 100, 101, 102] or protons [103, 62, 104] has to be ascribed to the radiation induced nanosize defect clusters acting as new point pinning centers: this will be described in detail in Subsection 1.4.2.

The hypothesis that the increase of J_c is due to the enhancement in the point pinning force was confirmed by Baumgartner et al. [105] and will be supported in the present work at proton fluences up to $1.4 \times 10^{21} \text{ p/m}^2$. Additional evidence was given by the observation that the value of J_c/J_{c0} is higher at high applied field thus reflecting that the increase in the critical current density is due to the enhancement of point pinning after irradiation [100, 98] (see Subsection 4.1.2).

In the high fluence regime (not treated in the present work), Brown and coworkers [100] stated that the decrease of J_c could be due to an overload in the cascade pinning that occurs after a dose at which the effects of the T_c and B_{c2} changes become significant. Snead [104] reported for Nb_3Sn wire a 98% of reduction in J_c for a high proton dose of about 10^{22} p/m^2 and established that this decrease was due to the reduction of T_c related to the disorder introduced into the lattice by protons.

1.4. Flux pinning in multifilamentary Nb_3Sn wires before and after irradiation

The most important physical parameter for applied superconductors is the critical current density under operation conditions, $J_c(B, T)$. Unlike B_{c2} and T_c , the critical current density J_c is not an intrinsic material property, i.e. it does not primarily depend upon the composition but is strongly influenced by the metallurgical state of the sample. In the mixed state, the magnetic flux of a type II superconductor penetrates in the form of fluxons¹¹ (or vortices) that remain anchored (pinned) to the defects, through an average pinning force, \mathbf{F}_p .

The flux lines experience a Lorentz force \mathbf{F}_L whenever a current flows in the superconductor, given by: $\mathbf{F}_{L(v)} = \mathbf{J} \times \mathbf{B}$ per unit volume of superconductor, where \mathbf{J} is the current density and \mathbf{B} is the flux density ($\mathbf{B} = n\phi_0$, where n is the number of flux lines per unit area). In a

¹¹ i.e. quantized flux lines of elementary magnetic flux $\phi_0 = \frac{h}{2e} = 2.0678 \times 10^{-15} \text{ Weber}$

homogeneous reversible material, the flux density is uniform and the spacing between adjacent flux lines in the Abrikosov lattice [106] is given by:

$$d = \left(\frac{1.15\phi_0}{B} \right)^{\frac{1}{2}} \quad 30$$

At low currents \mathbf{F}_p is larger than \mathbf{F}_L and vortices remain fixed to the pinning centers. At a certain current level the Lorentz force overcomes the pinning force and flux lines start to move in the direction of this force, inducing for the Faraday's law of induction an electric field. In this regime the superconductor shows an induced resistance and in this situation dissipation phenomena arise (flux flow resistance demonstrated by Kim et al [107] [108]).

The critical current density, \mathbf{J}_c , corresponds to the current at which $\mathbf{F}_L = \mathbf{F}_p$ thus is determined by magnitude of the pinning force: $\mathbf{J}_c \times \mathbf{B} = -\mathbf{F}_{p(v)}$. Pinning can be due to lattice defects (i.e. dislocations, impurities and precipitates of a second phase or grain boundaries) thus follows that superconductors characterized by strong pinning are metallurgical dirty (also called "dirty superconductors" or "hard superconductors"). As will be described in detailed in the following, the pinning defects may be superconducting or non-superconducting. The condition for these defects to be effective pinning centers is their size, which should be equal or larger than the coherence length, ξ (~ 4 nm for Nb₃Sn at stoichiometric composition [109]).

Flux pinning mechanisms

To describe flux pinning, it is necessary to know how one flux line interacts with a pinning defect and how this behavior is modified by the presence of neighboring flux lines [110]. Following this idea, D. Dew Hughes in 1974 [111] described the main flux pinning mechanisms in type II superconductors. He related the volume pinning force to the type of microstructure and with the principal interactions involved in the anchorage mechanism by means of the following relation:

$$F_p = \eta L f_p = -\eta L \frac{\Delta W}{x} \quad 31$$

where F_p is the total pinning force, f_p is the pinning force per unit length of pinned flux line and ΔW is the work done in moving unit length of flux line from a pinning center to the nearest position where it is unpinned, while x is the effective range of the pinning interaction; L is the total length of flux – line per unit volume that is directly pinned; and η is an efficiency factor determined by the extent to which its neighbors in the flux – lattice allow a flux – line to relax toward a position of maximum pinning.

These quantities are influenced by the superconducting nature of the pinning centers which determines the strength of the local interaction (i.e. small differences in the Ginzburg – Landau parameter, k , give rise to “ Δk ” pinning while non-superconductive particles to “normal” pinning); by the size, a , and spacing, l , (or “wavelength”) of the pinning microstructure compared to the superconducting penetration depth λ (i.e. if $a, l > \lambda$ there is a *magnetic* interaction while if $a, l < \lambda$ a *core* interaction); by the size of the pinning centers compared with the flux – lattice spacing, d given in equation 30 (*point* defects; *surface* defects; *volume* defects).

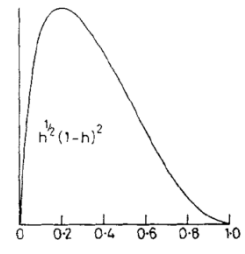
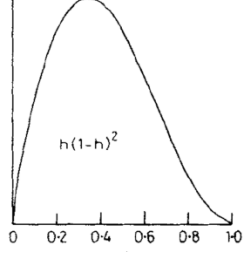
L	x	ΔW	$F_p(\mathbf{h})$	Shape of $F_p(\mathbf{h})$
Grain boundaries pinning (<i>Surface pinning</i>)	$\frac{S_v}{d}$	ξ	$\frac{-\pi\xi^2(H_{c2} - H)^2}{4.64 k^2}$ $\frac{\mu_0 S_v H_{c2}^2 h^{1/2} (1-h)^2}{4 k^2}$	
Defects cluster pinning (<i>Point pinning</i>)	$\frac{BV_f}{\Phi_0}$	$\frac{a}{2}$	$\frac{-\pi\xi^2(H_{c2} - H)^2}{4.64 k^2}$ $\frac{\mu_0 V_f H_{c2}^2 h(1-h)^2}{4.64 a k^2}$	

Table 1 Pinning functions: grain boundaries pinning (before irradiation); defects cluster pinning (second contribution to the total pinning force after irradiation). From D. Dew-Hughes [106].

Taking into account these factors the values of L , ΔW and x for specific situations can be determined and, through equation 31, the different pinning functions are obtained [111]. The pinning mechanism in multifilamentary Nb₃Sn wires before and after irradiation can be characterized by a core interaction.

As will be described in the next subsections, before irradiation grain boundaries (surface defects) are the main pinning centers while after irradiation the increase in the pinning force is explained adding a second contribution to the total pinning force due to the radiation induced defect clusters pinning (point defects).

In [Table 1](#) the pinning forces as a function of the reduced field h , $F_p(h)$, used in the present work are reported.

1.4.1. Flux pinning before irradiation

Many studies have shown that both grain boundaries and in some cases, second phase particles are effective in increasing the critical current density in type II superconductors. However Scanlan et al. [112] and Schauer and Schelb [113] found that the grain boundaries were the only defects present in sufficient density to account for flux pinning in multifilamentary Nb₃Sn wires. They measured the dependence of J_c on grain size combining the four probe technique measurement and TEM analysis; in this way they were able to provide the experimental curve for the pinning force as a function of the inverse of grain size ($1/D$), shown in [Figure 20](#). Pande and Suenaga [114], on the basis of interaction of fluxoids with dislocations forming the grain boundaries walls, derived a relationship between the pinning force F_p and grain size D in type II superconductors that approximately confirm the experimentally observed relationship by Scanlan and coworkers [112] and predicted a peak in F_p at $a_0/D \approx 0.2$, where a_0 is the lattice constant of the flux line lattice.

Three mechanisms have been used to describe the interaction between grain boundaries and flux lattice in a superconductor: the first one is based on the interaction between the grain boundary strain fields and the stress fields of the flux lines lattice; the second one is based on the

anisotropy of the critical field around the grain boundaries; the third one suggests that the electron scattering at the grain boundaries is the responsible for the pinning force [115].

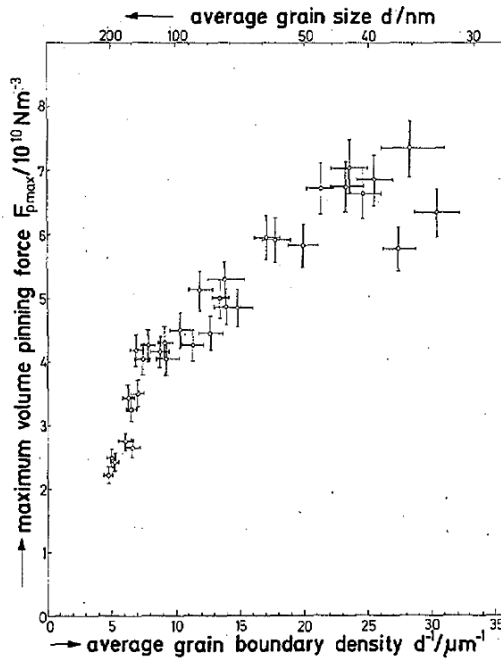


Figure 20 Pinning force maxima vs inverse average grain size for multifilamentary Nb₃Sn. Increase in pinning force is less than linear with 1/d. From W. Schauer and W. Schelb. [113].

In 1978 Das Gupta [116] measured the pinning force of a single grain boundary in Nb bicrystal and he found several indications to reject the first two models and to consider the electron scattering as the main mechanism responsible for grain boundaries pinning.

The first quantitative theory in favor of this grain boundaries pinning mechanism was formulated by Zerweck in 1981 [117]. Starting from the calculation of the mean free path and the coherence length as a function of the distance from the grain boundary he found that the elementary pinning force depends on the material purity: the pinning force is low for very pure materials ($\alpha \ll 1$), it increases when the purity decreases and reaches a maximum at $\alpha = 1$, then goes down again to zero for very dirty materials ($\alpha \gg 1$).

Yetter et al. [118] demonstrated by means of the Electron Scattering Flux Pinning model (ESFP model) that the interaction between flux lines and grain boundaries in Nb₃Sn is mainly due to the spatial variations of the electronic mean free path caused by these grain boundaries. The

results obtained by Yetter [118] are in qualitative agreement with those of Zerweck [117] with the only difference that the value of the impurity parameter at F_{pmax} is 10 times higher. The last developments of the theory of electron scattering for the grain boundary pinning force mechanism came from Welch in 1985 [119]. As a main improvement with respect to the previous works he took into account the width of the grain boundaries in the calculations of the elementary pinning force: F_{pmax} is achieved for grain boundary widths 1.5 times larger than the coherence length ξ , and for an impurity parameter $\alpha = 2$.

The two features of grain boundaries pinning determining the pinning strength acting on the flux line lattice in A15 superconductors are the grain size and the composition variation of phases near the grain boundaries. The decrease of grain size can be achieved by the variation of the heat treatment conditions or by the introduction of elements to inhibit grain growth, thus causing an improvement of the pinning through the generation of more boundaries to scatter electrons. Instead, the composition variation of the phases near the grain boundaries would increase the pinning force by the enhancement of the Ginzburg – Landau parameter k near the boundaries. This k – enhancement is usually thought to be due to the local decrease of the electronic mean free path caused by deviations from stoichiometry close to the grain boundaries [119].

Scaling law for flux pinning

The major goal of the flux pinning theory is the prediction of the functional dependence of F_p on magnetic field B and temperature T under the influence of the microstructural parameters. Fietz and Webb [120] first demonstrated in a number of Nb – based alloys that, if the temperature is changed, the pinning force obeys a scaling law for which the peak in F_p scales as $[H_{c2}(T)]^{2.5}$:

$$F_p = [H_{c2}(T)]^{2.5} f(b), \text{ where } f(b) \text{ is uniquely a function of the reduced magnetic field } b = \frac{B}{B_{c2}}.$$

The importance of this discovery is that knowing F_p at a given temperature the F_p at other temperatures can be simply found by scaling the results by $[H_{c2}(T)]^{2.5}$. The scaling behavior was subsequently identified in several other superconductors including Nb₃Sn and many pinning force model expressions were proposed in the past decades. Recently Ekin [121] unified all these

models in that it is known today as the Unified Scaling Law (USL) and the pinning force per unit length is expressed by:

$$F_p = K(t, \varepsilon_0) f(b) \quad 32$$

where the function $K(t, \varepsilon_0)$ is a prefactor that describes the pinning force dependence on reduced temperature t and intrinsic axial strain $\varepsilon_0 \equiv \varepsilon - \varepsilon_m$ defined as zero at the strain ε_m where I_c is maximum, whereas $f(b)$ is a function of the reduced field b :

$$b = \frac{B}{B_{c2}^*(t, \varepsilon_0)} \quad 33$$

where B_{c2}^* is an effective upper critical field used for scaling (or simply scaling field), which is in general not identical to the upper critical field determined experimentally, for instance by means of resistivity measurements. Similarly, the reduced temperature t is defined by an effective critical temperature $T_c^*(\varepsilon_0)$:

$$t = \frac{T}{T_c^*(\varepsilon_0)} \quad 34$$

The field dependence of the pinning force can be expressed as:

$$f(b) = b^p (1-b)^q \quad 35$$

where the low- and high-field exponents p and q must be constant for the pinning force to be shape invariant. If these parameters would exhibit a dependence on field, temperature, or strain, scaling would fail. In polycrystalline Nb₃Sn the experimentally determined exponents are often close to $p = 0.5$ and $q = 2.0$, which is consistent with pinning by core interaction between the vortices and normal conducting surfaces, as shown in [Table 1](#), thus implying grain boundary pinning as the dominant mechanism [111]. The reduced field at which $f(b)$ reaches its maximum is given by:

$$b_{max} = \frac{p}{p+q} \quad 36$$

Thus, in case of pure grain boundary pinning with the scaling exponents $p = 0.5$ and $q = 2$ the pinning force maximum occurs at $b_{max} = 0.2$.

Assuming that the temperature and strain dependence of both $K(t, \varepsilon_0)$ and $B_{c2}^*(t, \varepsilon_0)$ can be separated, equation 32 can be cast in the convenient separable form [121]:

$$F_p = C g(\varepsilon_0)h(t)f(b)$$

In the above expression C is a constant, $g(\varepsilon_0)$ and $h(t)$ are the dimensionless strain and temperature dependences respectively, and $f(b)$ is the field dependence given by equation 35.

In 1972 Kramer [122] assumed that flux motion at low fields is primarily due to depinning, while synchronous shear of the flux line lattice is the dominant mechanism at high fields where a “peak effect” in the pinning force arises.

1.4.2. Flux pinning after irradiation

It was extensively discussed in Subsection 1.3.1 that the primary effect of high energy irradiation consists in removing atoms from their lattice sites (PKA), producing large numbers of vacancies and interstitials. The energy is dissipated in the lattice as the high energy particles are slowed down, inducing mobility of these point defects which subsequently reorganize themselves into clusters and dislocation loops.

The first evidence of the radiation induced defects is given by Holdway [123], who studied fast neutron irradiated Nb₃Sn samples (up to fluences of $\sim 3 \times 10^{22} \text{ n/m}^2$) by means of Transmission Electron Microscopy (TEM). He observed disordered regions with sizes between 2 and 10 nm as well as dislocation loops with diameters between 15 and 30 nm with a loop density between 10^{20} and 10^{21} m^{-3} . A TEM study of Fähnle [102] in Nb₃Sn at $\sim 1 \times 10^{22} \text{ n/m}^2$ revealed defects with diameters of approximately 10 nm, and a density of $5 \times 10^{21} \text{ m}^{-3}$.

It follows that the atomic disorder produced by irradiation will cause non – superconducting regions (*normal* pinning) or superconducting regions (Δk pinning) with lower T_c with respect to the matrix.

From the above mentioned description given by Dew Hughes [111] it follows that when the size of a defect is small compared to the Ginzburg – Landau penetration depth, the pinning arises

primarily from the difference in free energy between the pinning center and the surrounding matrix (*core* interaction) and in this case ΔW in equation 31 is equal to the change Δg in the Gibbs function per unit length g . For normal conducting pinning centers Δg is equal to g , and hence $\Delta W = g$. For spherical pinning centers the interaction range x in equation 31 should be equal to the radius of the defect, as reported in [Table 1](#). By assuming that the length of pinned flux lines per unit volume is proportional to the total length of flux lines per unit volume B/ϕ_0 , Dew-Hughes found the field dependence reported in [Table 1](#) and described by the expression:

$$F_p \propto b(1 - b)^2 \quad 37$$

for point-like (i.e. small compared to the flux line spacing, d) defects which exert a pinning force by normal core interaction. This result corresponds to the scaling exponents $p = 1$ and $q = 2$ within the framework of the unified scaling law [124].

A sufficient density of radiation induced defects will have a significant influence on the volume pinning force F_p and changes in magnitude and functional dependence of the pinning force were reported in literature. Cullen in 1968 [125], for instance, reviewed the effects of irradiation on flux pinning in type II superconductors: neutron, proton and deuteron irradiation on Nb₃Sn prepared by a variety of techniques; neutron irradiation of Nb₃Al, V₃Ga and V₃Si. In all cases the J_c increases after irradiation, the enhancement being always larger in low J_{c0} materials. Voronova et al. [62] irradiated Nb₃Sn wires with various fluences of protons, α particles and fission fragments having an energy of 2.6 MeV and investigated the changes of $J_c(H)$ and T_c as a function of irradiation dose. They found that the variation of T_c and J_c are a consequence of different type of defects: J_c is more sensitive to clusters and its nature depends strongly on the initial state of the materials while T_c depends on the homogeneous distribution of small defects. After 14.8 MeV neutron irradiation to a fluence of 1.35×10^{22} n/m² on Nb₃Sn Guinan et al. [126] reported an increase of F_{pmax} accompanied by a shift of the reduced field b_{max} to higher values. This shift was also observed by Seibt [127] in V₃Ga irradiated with 50 MeV deuterons who reported a good agreement with the Kramer model (scaling exponents $p = 0.5$ and $q = 2$) in the unirradiated state, whereas a high-field exponent of $q = 1$ produced better agreement after irradiation to a fluence of 2.6×10^{21} n/m². According to equation 36 this corresponds to $b_{max} = 0.2$ in the unirradiated state, and $b_{max} = 0.33$ after irradiation. Küpfer et al. [63] and

Maier and Seibt [128] introduced a qualitative two mechanism model to describe the changes in the volume pinning force of irradiated A-15; according to this model, the total pinning force F_p after irradiation is given by the sum of two contributions: the first one corresponds to grain boundary pinning and the second one refers to additional pinning induced by the formation of radiation defects (point pinning). This model was recently improved by Baumgartner et al. [105] who introduced the scaling law parameters for the two contributions of the total pinning force.

CHAPTER 2: PREPARATION AND PROPERTIES OF Nb₃Sn SAMPLES

The proton irradiations at 65 MeV and 24 GeV are performed on three types of Ti and Ta alloyed Nb₃Sn industrial multifilamentary wires fabricated using the RRP and PIT techniques. The effects of the Bragg peak was studied on binary Nb₃Sn platelets which were irradiated with protons of 10 MeV.

The cross section and the heat treatments of the different wire types are reported in Section 2.1. In Section 2.2 the fabrication of the Nb₃Sn platelets performed at the University of Geneva are described and the analysis (SEM, X-ray and SQUID) to estimate the quality of these samples is shown; finally, in Section 2.3, the main differences between the Nb₃Sn wires and platelets are discussed.

2.1. Description of the RRP and PIT Nb₃Sn multifilamentary wires

2.1.1. Characteristics of the Ta and Ti alloyed Nb₃Sn wires

The present proton irradiations were performed on three different Nb₃Sn industrial multifilamentary wires with a length of approximately 5 mm and a mass of ~ 20 mg. As shown in [Figure 21](#), two wires are of the RRP (or Restacked Rod Process) type produced by Oxford Superconducting Technology (OST), one alloyed with Ta (billet #7419) and the other with Ti (billet #11976). The third one was a Ta alloyed PIT (Powder In Tube) wire by Bruker (EAS), (billet #0904). A common feature of these wires is the Nb diffusion barrier surrounding the Nb₃Sn subelements (bundles) embedded in a copper matrix for stabilization. In RRP wires, a subelement consists of Nb, NbTa or NbTi rods which are inserted in a copper matrix, together with a central Sn core. The RRP subelements are assembled in a copper can and drawn to the final diameter. Long intermediate annealings are necessary to diffuse the Sn into the copper matrix, to form Sn rich bronze, then the A15 phase. Very high A15 volume fractions, and thus J_c overall values, can be obtained with this technique. In PIT wires Nb or Nb/Ta tubes are filled

with NbSn₂, Sn and Cu powders; then the sealed tubes are inserted into a copper matrix, cold extruded and drawn into the final diameter.

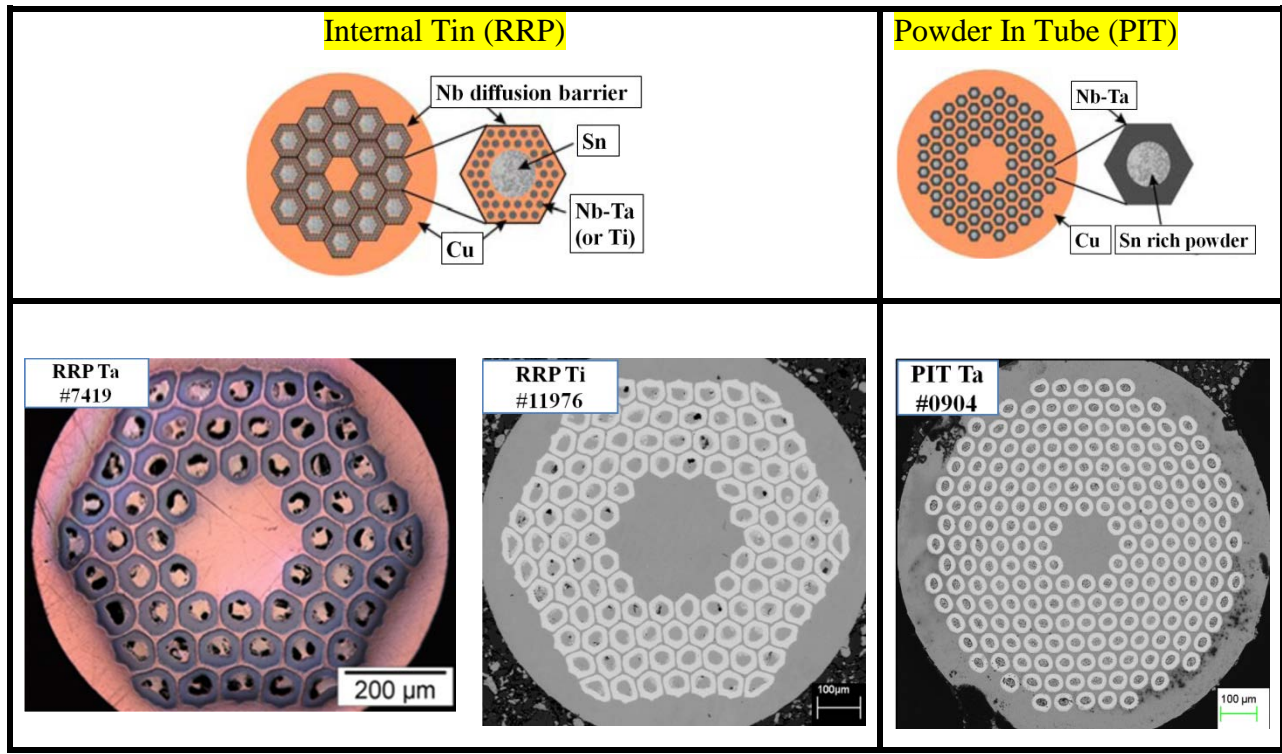


Figure 21 Cross section of the three types of multifilamentary Nb₃Sn wires: on the left the two Internal Tin (Restacked Rod Process technique, RRP) wires (Ta and Ti alloyed) and on the right the PIT wire (Ta alloyed).

The most important characteristics of the three wires are reported in [Table 2](#).

The inner and outer sub-element radii ρ_i and ρ_o required for the evaluation of the critical current density were determined from Scanning Electron Microscope (SEM) images provided by C. Scheuerlein at CERN ([Figure 22](#)).

In the SEM image the A15 region of the subelement can be recognized from the other materials (Nb diffusion barrier around each sub-element, unreacted region in the sub-element center, and copper matrix) by its gray-scale intensity. Since the magnification of the image was known, the A15 area and thus the radius are calculated by counting the pixels within a certain gray-scale range.

Wire	Diameter (mm)	Type	Sub-elements	Twist pitch (mm)	Cu-non Cu Ratio	ρ_i Err. ± 0.1 (μm)	ρ_o Err. ± 0.1 (μm)
#7419	0.8	RRP+Ta	54	12	0.92	21.0	37.1
#0904	1.0	PIT+Ta	192	24	1.24	12.3	22.5
#11976	0.8	RRP+Ti	108	14	1.02	15.3	26.7

Table 2 Main characteristics of reacted Nb₃Sn multifilamentary wires irradiated in the present work.

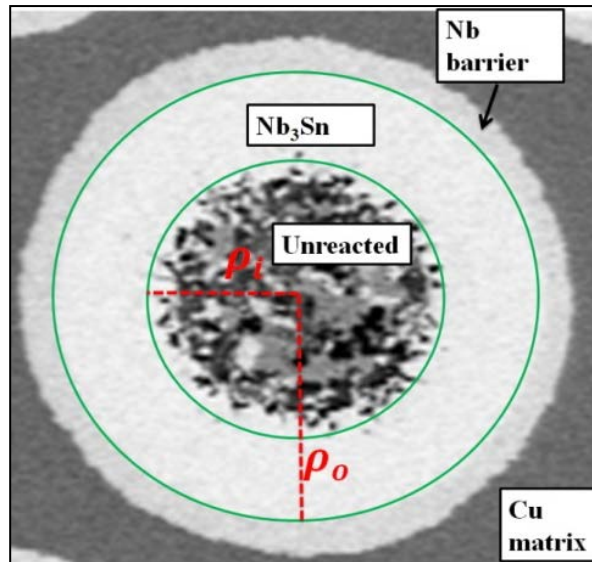


Figure 22 SEM image of a subelement of PIT Ta alloyed (#0904) wire.

2.1.2. Heat treatments

The reaction of the Nb₃Sn wires described in the subsection above was performed at the University of Geneva. The reaction temperatures and the durations of the heat treatments for all the types are listed in Table 3. After reaction the wires were cut by means of a diamond saw to 5-6 mm length, the appropriate length for magnetization measurements.

Wire type	Temperature (°C)	Duration (h)
RRP #7419 (Ta alloyed)	695	17
RRP #11976 (Ti alloyed)	210	48
	400	48
	665	50
PIT #0904 (Ta alloyed)	625	250

Table 3 Reaction heat treatments performed on the Nb₃Sn multifilamentary wires.

2.2. The fabrication of thin Nb₃Sn platelets

No study is known so far about the decrease of the LRO parameter S (and thus of T_c) due to the proton radiation damage at the location of the Bragg peaks in Nb₃Sn.

In the present work, in order to investigate the conditions at the Bragg peaks, very thin Nb₃Sn platelets were used. Further details on the Bragg peak experiment are described in Subsection 3.1.2.

The preparation of homogeneous, single phase platelets required a particular development, which will be described in the present section, where the details about the preparation of the 24 Nb₃Sn platelets for 10 MeV proton irradiation performed at Kurchatov Institute (KI) are given.

The Nb₃Sn platelets for the Bragg peak study were obtained starting from a Nb₃Sn bulk sample prepared by reacting in a HIP furnace at 1250°C under 2 kbar Ar pressure, this technique being described in the next Subsection. To study the degree of atomic ordering before and after high energy proton irradiation in A15 type compounds, a particular emphasis has to be given to the metallurgical state of the platelets (homogeneity, compositional distribution, precise determination of composition).

The ideal conditions for order parameter determination are given by 100% single phase samples with a very narrow composition distribution. These conditions are difficult to be achieved, but can be approximated by long high temperature treatments under HIP conditions. The

determination of the order parameter can in principle be performed even if additional phases are present, provided that their respective crystal structures are known. The corresponding spectra can be refined and subtracted from A15 diffraction pattern. However, a possible overlap with A15 superstructure lines would lead to seriously enhanced error limits, due to unfavourable peak/background ratios, resulting in a poor counting statistics. Another cause influencing the precision of the order parameter determination is the presence of unrecognized, small amounts of additional phases, which alter the background intensity of the superlattice lines.

2.2.1. HIP (Hot Isostatic Pressure) process to fabricate homogeneous bulk Nb₃Sn samples

To obtain dense A15 phase samples close to the stoichiometric composition Nb₇₅Sn₂₅ (25at%Sn), the heat treatment was performed under Hot Isostatic Pressure (HIP) conditions by sintering Nb and Sn powder mixture under an Argon pressure of 2 kbar. The HIP experiments were performed at the facility at the Dept. Applied Physics (GAP) of the University of Geneva. As shown by the phase diagram (see [Figure 2](#)), the choice of the sintering temperature allows to get Sn contents at compositions very close to stoichiometry.

Set-up before HIP

The mixture of Nb powder (99.9 % purity, desoxydized, (25 ÷ 45) μ m particle size; furnished by Starck) and Sn powder (Goodfellows, 99.5 % purity, 40 μ m particle size), with a ratio of Nb : Sn = 3 : 1 (see later on for further details), are mixed for almost 1 hour in a 3D mixing machine, enclosed in a Nb jacket and loaded into a stainless steel billet shown in [Figure 23](#). The billet is composed of a cylindrical stainless steel jacket with a stainless steel capsule that encases a cylindrical Nb container, covered by a Nb capsule.

The masses of Nb and Sn powders have been chosen to get a Sn composition of 24.8 at.%Sn, i.e. slightly below the stoichiometric composition of 25 at.%Sn. This choice was motivated by the necessity to get single phase samples: indeed, at 1'250 °C, the Nb rich limit of the two-phase

region A15+Nb₆Sn₅ starts very close to 25 at.%Sn, and even a small composition gradient would have caused the presence of a second phase.

To avoid oxygen being trapped inside the powder mixture during the pressing procedure, the powders and the Nb container was set into glove box allowing evacuation to 100 mm Argon and rinsing (3 cycles). After pressing, the powder inside the capsule (mass: 425 g) had a tap density of about 70%. The upper Nb cover was enclosed into a stainless steel capsule. This capsule, made of stainless steel with grooves for pumping, was pumped under 10⁻⁶ mm Hg and closed vacuum tight by electron bombardment at CERN. Before electron welding, the capsule was preheated 24 hour at 150°C under high vacuum.

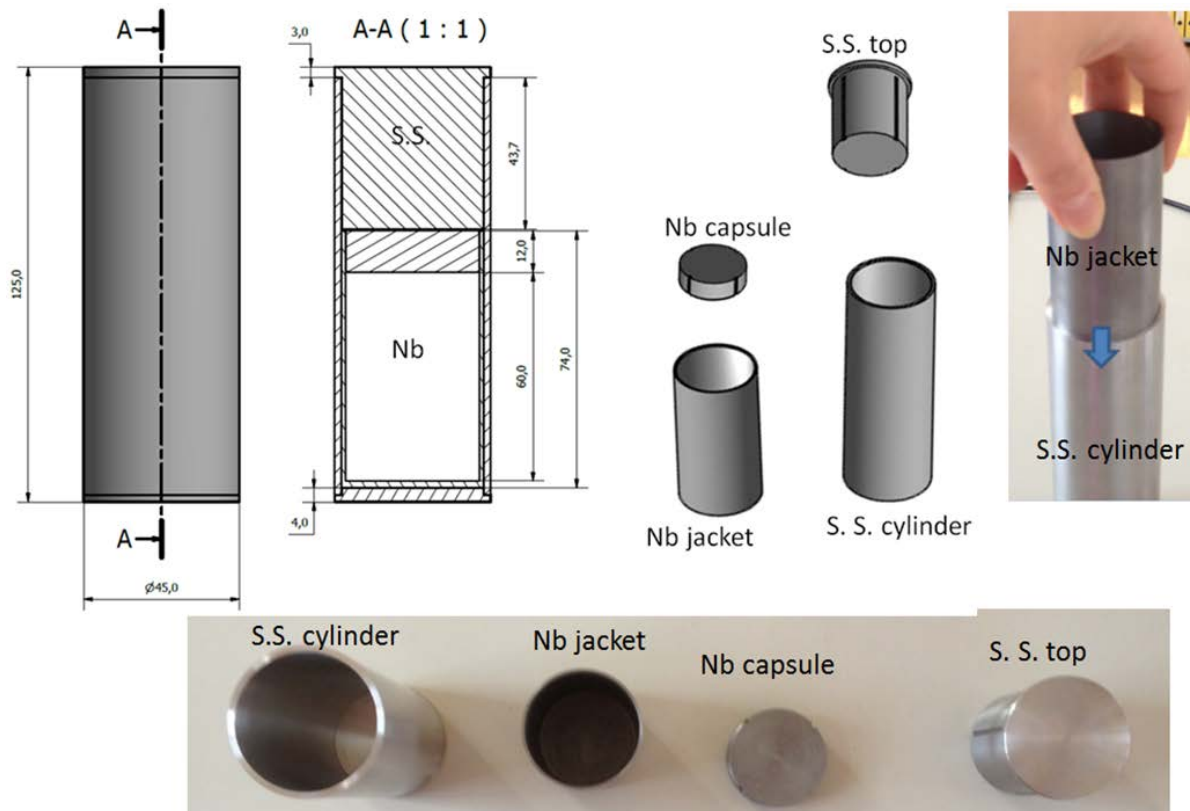


Figure 23 Billet for Nb₃Sn HIP treatment.

The HIP treatment

The HIP treatment was performed at the University of Geneva at $T = 1250^\circ\text{C}$ under an Argon pressure of 200 MPa followed by a controlled slow cooling rate to avoid thermal crack formation in the sample. In Figure 24, the 95 hours (4 days) full cycle for the HIP treatment is shown.

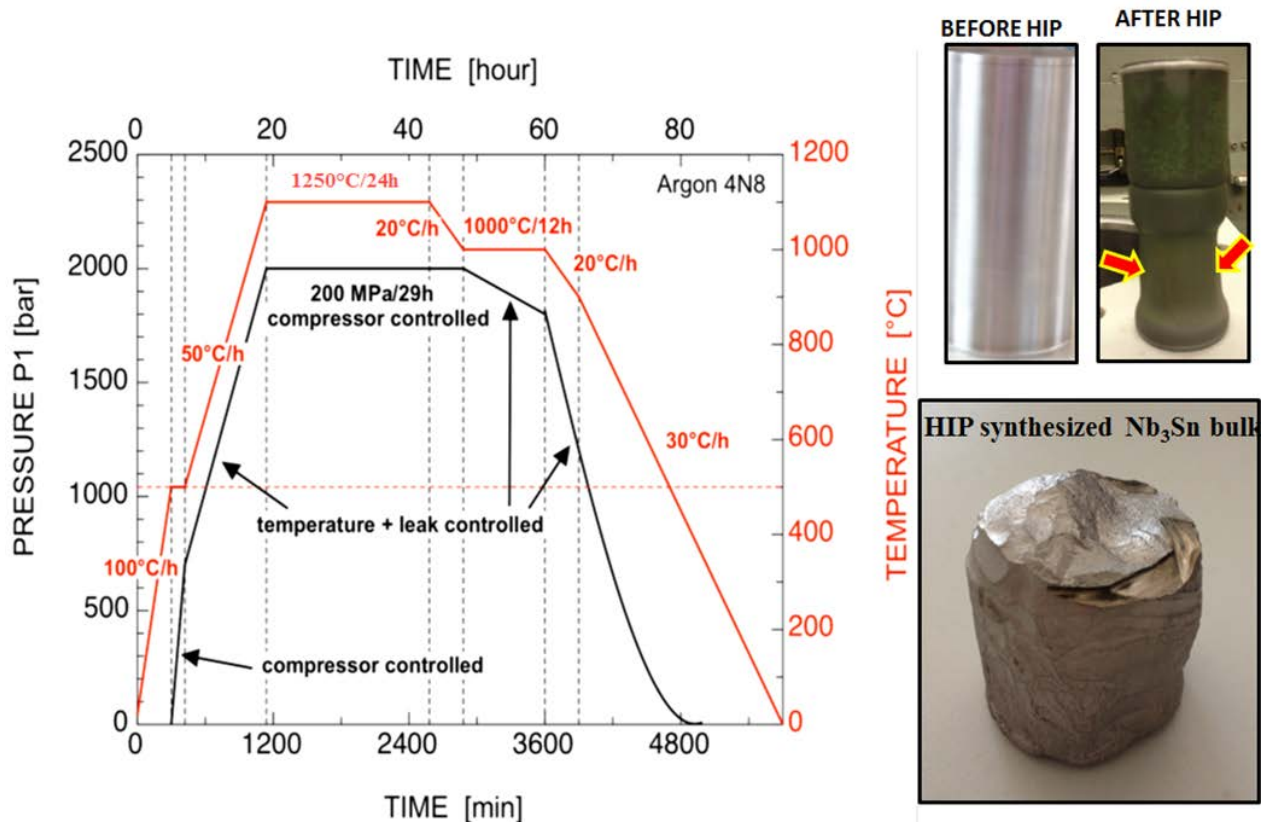


Figure 24 Cycle of Nb₃Sn HIP treatment performed at the university of Geneva (left); pictures of the Nb₃Sn bulk sample (bottom right) extracted from the billet before and after HIP (top right).

2.2.2. Cutting of thin platelets by spark – erosion

After the HIP process, the steel jacket was mechanically removed from the Nb₃Sn block. Sample pieces were cut by means of spark erosion (see Figure 25) and carefully polished with silicon carbide grinding papers from 40 to 6 μm to remove the cutting part containing Carbon and Oxygen impurities arising from the spark erosion dielectric oil. The platelets were polished

down to the final thicknesses requested for the Bragg peak experiment, e.g. 100 – 200 μm (see subsection 3.1.2 for further details).

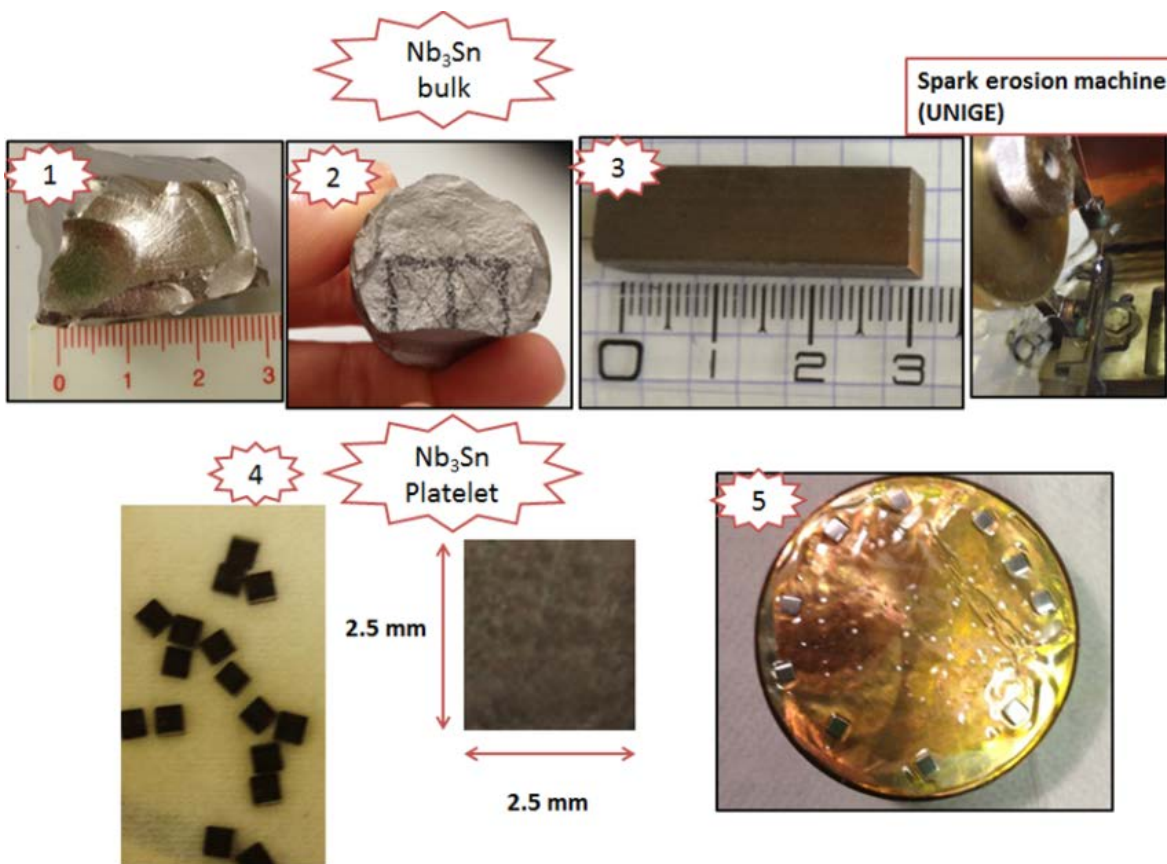


Figure 25 Main steps to prepare Nb₃Sn platelets from the bulk sample. In pictures 1 and 2 the Nb₃Sn block after extraction from the steel jacket. In picture 3 the Nb₃Sn pieces obtained from the Nb₃Sn block by means of spark erosion. In 4 and 5 the Nb₃Sn platelets before and after polishing respectively.



Figure 26 Ti boxes surrounding the Nb₃Sn platelets to avoid oxidation of the sample surface during the flash anneal treatment.

2.2.3. Flash Anneal for stress release

The polishing procedure induces a considerable stress at the surface of the Nb₃Sn platelets, which renders the precise measurement of the order parameter quite impossible. This problem was solved by submitting the polished platelets to a flash-anneal of 10 minutes at 900°C under a pressure of 10⁻⁷ mbar. To avoid oxidation of the sample surface during the flash-anneal procedure, the platelets were enclosed into a Ti box, shown in [Figure 26](#). The result of this procedure can be verified by comparing the X – ray patterns of the platelet surface before and after flash-anneal. As shown in [Figure 27](#), the asymmetric behavior of the peaks due to surface tension was completely removed.

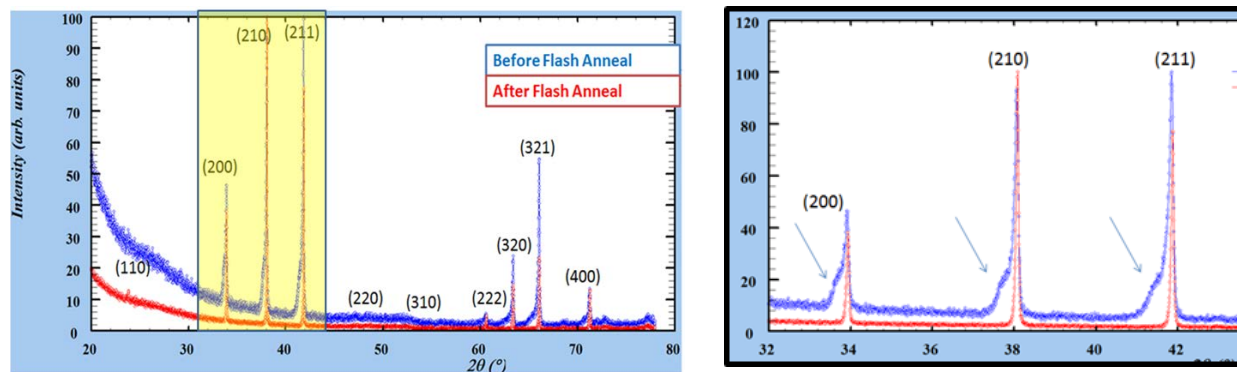


Figure 27 X-ray patterns of the Nb₃Sn platelets, before and after flash-anneal (900 °C / 10 minutes). The asymmetric behavior of the peaks due to surface tension induced by polishing is fully removed after flash-anneal.

2.2.4. Characterization of the Nb₃Sn bulk samples by SEM, X-ray and AC susceptibility measurements

To test the quality of such samples before to send them to the Kurchatov Institute (Russia) for room temperature proton irradiation at 10 MeV, the Nb₃Sn platelets were analyzed by means of SEM, X – ray and magnetization measurements at the University of Geneva (Dept. Quantum Material Physics, DQMP). A series of 4 samples was prepared by HIP processing (described above). All the platelets used in the present work were cut from that HIP sample with the best quality (sample #4), characterized in the following.

Due to the preparation the present platelets are found to contain a small amount of oxygen. By means of Hot Extraction the total amount of Oxygen was determined to 0.14 wt.% (approximately 1 at.%), that one of Carbon to 0.01wt.%. (hot extraction analysis by Pascher, Germany).

SEM analysis on a broken piece from sample #4 reveals grain sizes close to 20 μm , as shown in Figure 28.

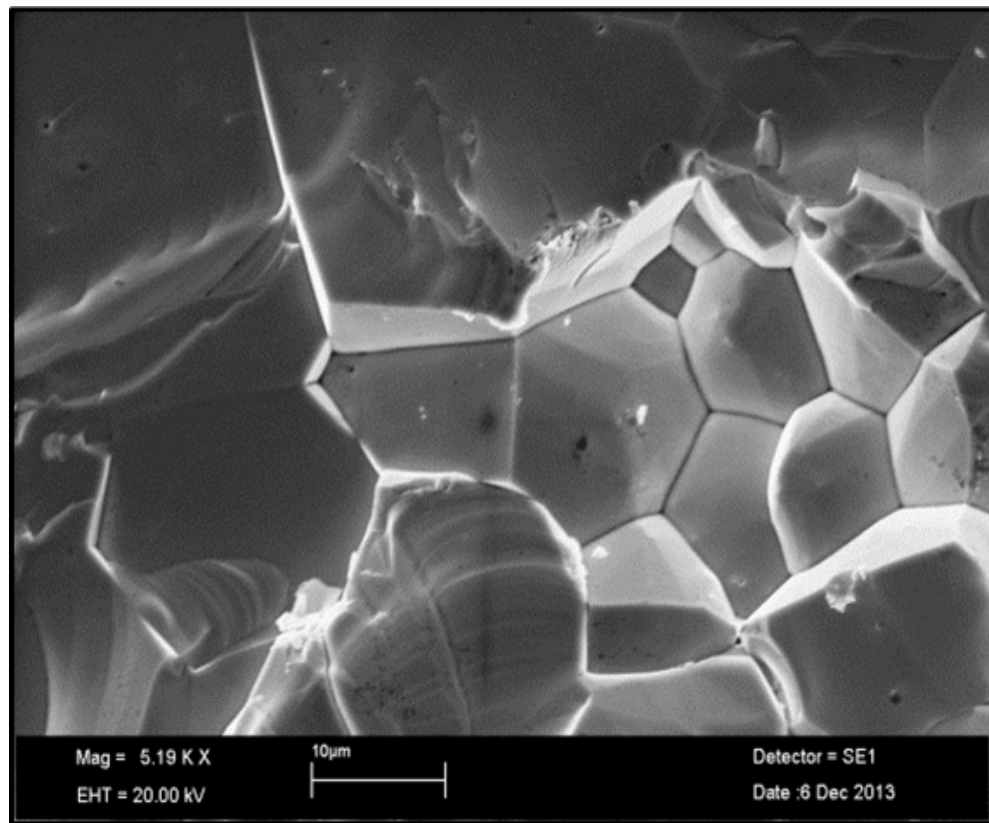


Figure 28 SEM image of the Nb₃Sn bulk sample (#4), showing average grain size of 20 μm .

The X – ray pattern of Nb₃Sn powder from the same sample is shown in Figure 29. In order to minimize the statistical error, measurements times as long as 15 hours were chosen, with 3.5 seconds per step and a rotation speed of 18 rpm. A Rietveld refinement on a large number of samples was performed to determine the LRO parameter and the lattice constant. The chemical composition, the preferred orientation (texture) as well as the microabsorption effects were taken into account during the refinement procedure (see subsection 3.3.1 for further details). To

improve the statistics needed to get reliable results from the refinement procedure, the following results are average values obtained after a dozen of X – ray measurements performed on the same sample: the long range order parameter for the 6c (chain sites) and 2a (cubic sites) sites of the Nb₃Sn phase (24.8 at%Sn) is: $S \simeq S_a = S_b = 0.98 \pm 0.02$. This value corresponds to a state of atomic ordering very close to perfect ordering, with the occupation factors $r_a = 0.997 \pm 0.002$ and $r_b = 0.991 \pm 0.002$ and the lattice constant is $5.291 \pm 0.003 \text{ \AA}$. Further details will be given in Subsection 4.2.1.

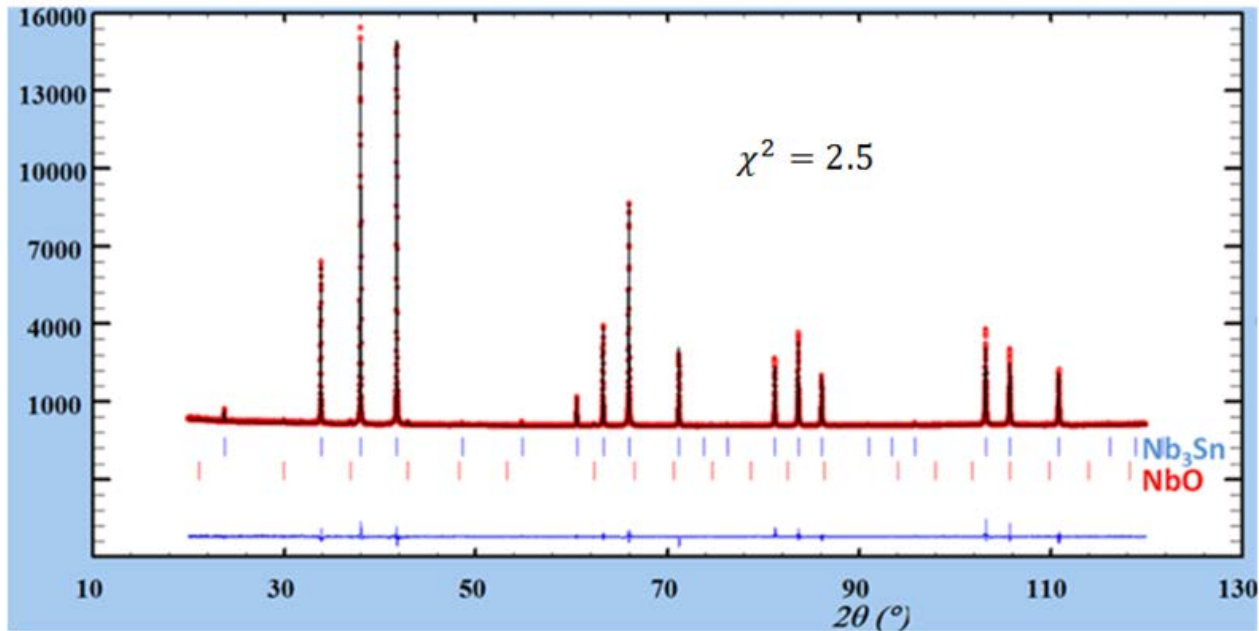


Figure 29 Rietveld refinement on Nb₃Sn powder (sample #4). Time scan: 15 h; time/step: 3.5 s.

The critical temperature of the Nb₃Sn platelets from sample #4 was determined by VSM magnetic measurement in zero field by means of a SQUID magnetometer (Quantum Design MPMS XL, Unige) and was estimated to be 17.9 K as the upper value of the transition, as shown in Figure 30. The upper critical field at 0 K was extrapolated to $B_{c2}(0) = 25.97 \text{ T}$ using the Werthamer-Helfand-Hohenberg (WHH) theory [129] on the VSM (Vibrating Sample Magnetometer) magnetization measurements (up to 5 T) in Zero Field Cooling (Figure 31).

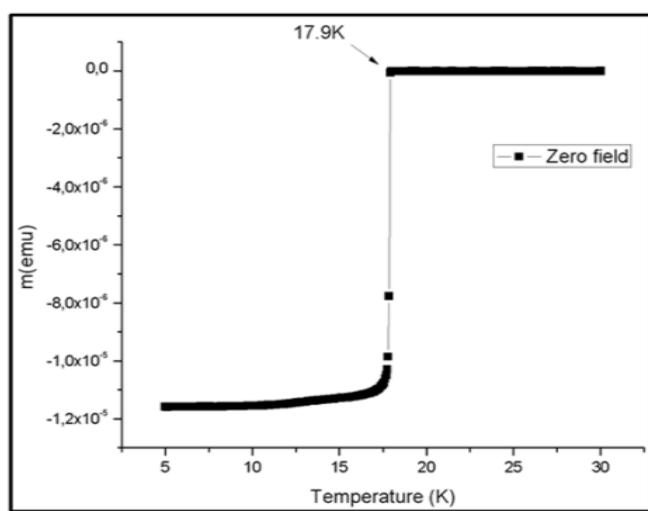


Figure 30 VSM magnetization measurement in zero field for the Nb₃Sn platelet (sample #4).

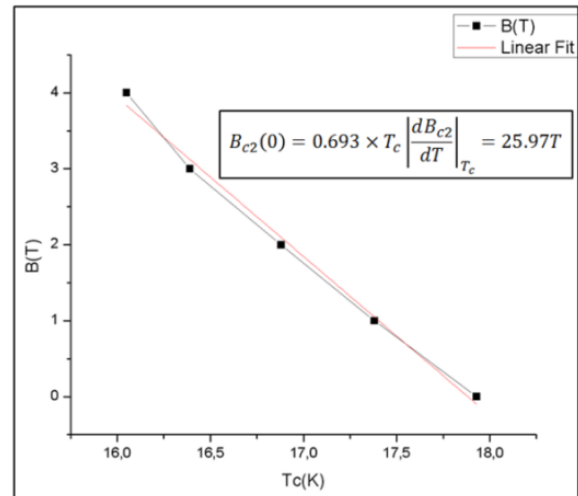


Figure 31 Initial slope for Nb₃Sn bulk sample #4. The WHH [129] method is used to extrapolate the B_{c2} at 0 K.

2.3. Main differences between bulk and multifilamentary Nb₃Sn wires

In addition to the higher homogeneity in HIP processed bulk Nb₃Sn, the main difference between Nb₃Sn wires and bulk samples consists in the different size of the grain boundaries, i.e.: ~20 μm for bulk samples and ~100 nm for the commercial multifilamentary wires. It follows that the critical current density in Nb₃Sn bulk sample is about two orders of magnitude lower than in the wires, as shown in Figure 32 where the critical current densities obtained at 4.2 K are compared.

As shown in Figure 33, J_c for the bulk sample at higher temperatures shows a “peak effect” that is not detected in the wires [130, 131]. It can be suggested that the absence of the peak effect in the wires could be attributed to the absence of the Bragg Glass phase in the $H(T)$ phase diagram.

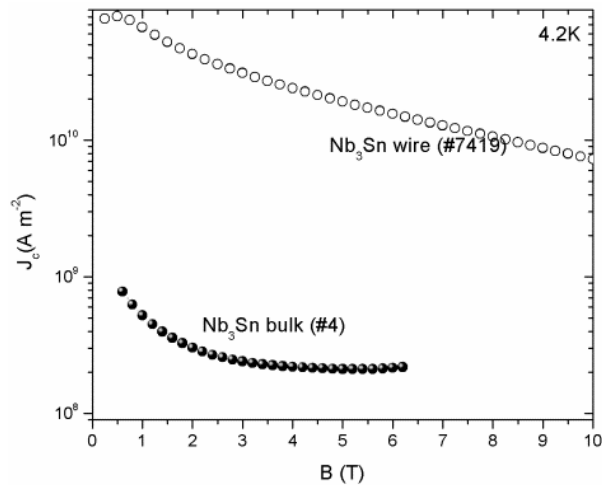


Figure 32 J_c comparisons at 4.2K between Nb₃Sn wire (Ta alloyed wire, #7419) and Nb₃Sn bulk (binary, #4).

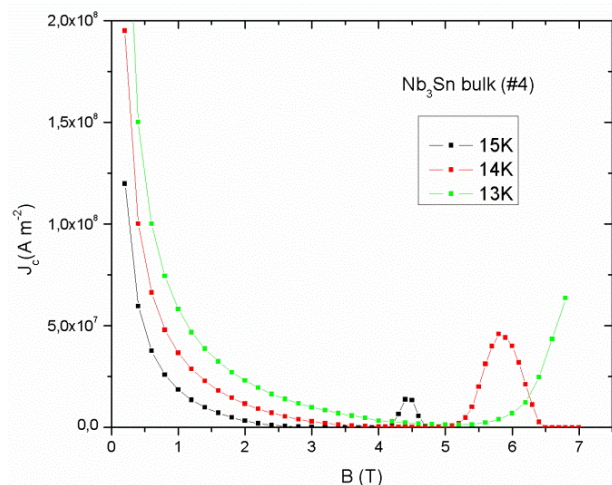


Figure 33 J_c for Nb₃Sn bulk sample (#4) at high temperature: the peak effect [thanks to T. Baumgartner, ATI Vienna, for this measurement]

CHAPTER 3: MEASUREMENTS and PROTON IRRADIATION EXPERIMENTAL SET-UP

In this chapter the procedure adopted to perform the proton irradiation experiments and the measurements accomplished on the Nb_3Sn wires and platelets before and after irradiation are described in detail. In Section 3.1 the experimental set-up and the irradiation facilities are reported. The VSM and AC susceptibility measurements to obtain the critical current density, J_c , and the critical temperature, T_c , respectively, are discussed in Section 3.2 while the diffraction measurement to get the Bragg-Williams LRO parameter, S , by means of Rietveld refinement is described in Section 3.3.

3.1. High energy proton irradiation experimental set-up

In the next subsections some details on the characteristics of proton irradiation and on the experimental set-up for the three facilities are provided; a few remarks about the sample activation and the safety condition to adopt here at CERN are discussed.

3.1.1. Proton irradiation of Nb_3Sn wires

Room temperature irradiation at 65 MeV and 24 GeV with the maximum proton fluences of $1.0 \times 10^{21} \text{ p/m}^2$ and $1.38 \times 10^{21} \text{ p/m}^2$ were accomplished at the cyclotron of the Université Catholique de Louvain-La-Neuve (UCL) and at CERN (IRRAD1), respectively. More details on the set-up for these irradiation facilities have been described by Otto et al. [131] and the main features will be summarized in the following. These proton radiation loads are well beyond those indicated by F. Cerutti and A. Lechner [2] on the basis of FLUKA simulations for the whole HL-LHC operation time; indeed they estimated that at 3000 fb^{-1} the maximum fluence, calculated for the case with W shielding, is more than $3 \times 10^{19} \text{ p/m}^2$. As shown in [Figure 34](#) the proton

energies for the present experiment were chosen in order to cover the region of the spectrum where the maximum fluence is expected.

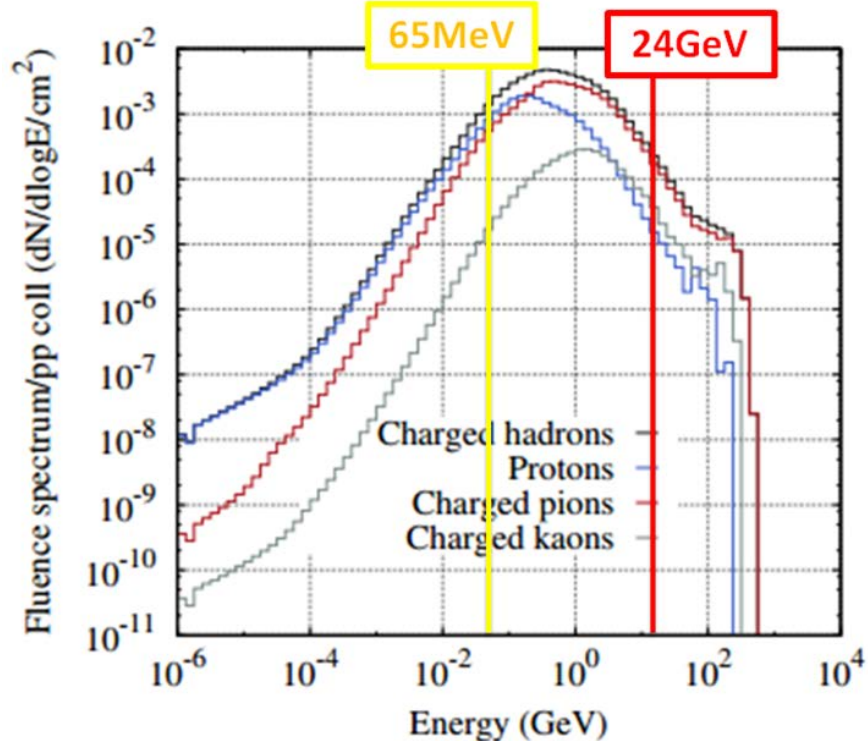


Figure 34 Proton energies used in the present experiments with respect to the energy spectrum calculated with FLUKA code by Cerutti and Lechner [2]

In addition from FLUKA simulations performed by the author follows that for all proton energies, the wire diameter (about 1 mm, see Subsection 2.1.1) is small with respect to the proton penetration depth (Table 4) thus the Bragg peak is located outside the wire.

However, from the new calculations with W shield by Lechner et al. [2], even if only 1.7% of the total dpa (1.8×10^{-4} dpa in the innermost winding) is due to protons, the secondary ions generated by the interactions between the primary radiation with the W shield includes new Bragg peaks.

Thus, as will be explained in the next subsection, the "Bragg peak experiment" is aimed to study the effects of proton irradiation (as an example of charged particles) on Nb₃Sn (A15) structure when the Bragg peak occurs inside the material.

E [MeV]	Penetration depth [cm]
10	3×10^{-2}
20	9.8×10^{-2}
30	1.8×10^{-1}
65	7.3×10^{-1}
24×10^3	55

Table 4 Proton penetration depth for different proton energies in Nb₃Sn calculated by means of FLUKA simulation

Irradiation temperature

In the present work proton irradiations were performed at room temperature while in LHC upgrade the operation temperature should be of 1.8 K. It is known that at 1.8 K vacancies do not show any mobility and site exchanges can only occur by the energy transmitted by the multiple collisions. The question arises whether the experimental condition adopted in the present work, i.e. an irradiation temperature, T_{irr} , slightly above 300 K are suitable to describe the real condition of the quadrupoles in HL-LHC. This question has been answered by Söll et al. [133] who showed that the self-annealing effects between 4.2 K and 300 K are almost negligible.

Indeed, Söll et al. [133] observed that after neutron irradiations ($E > 0.1$ MeV) of Nb₃Sn wires at 4.6 K up to a fluence of 3.9×10^{22} n/m², the T_c reduction was of 0.8 K. Sweedler et al. [79] reported a similar decrease in T_c after neutron irradiation at >150 °C up to 10^{22} n/m² ($E > 1$ MeV). Meier-Hirmer and Küpfer [134] irradiated V₃Si single crystals with fast neutrons at 240 °C and they found that the decrease of T_c with increasing fluence is substantially reduced for $T_{irr} = 240$ °C [134] when compared with data taken at $T_{irr} \leq 150$ °C by Sweedler et al. [79].

The observed lower decrease of T_c after heavy irradiation fluences with higher T_{irr} values (i.e. very far from room temperature irradiation) has its origin in thermal recombination effects during irradiation. These results indicate that changes in superconducting properties of Nb₃Sn after room temperature irradiation can be compared to the effects of 1.8 K irradiation.

Experimental set up

Proton irradiations at 65 MeV up to fluences of 1×10^{21} p/m² have been performed at the Cyclotron of Université Catholique de Louvain (UCL) in Belgium. An aluminum sample holder positioned in a water cooled Cu holder was used to irradiate the Nb₃Sn wires. The surface of the beam produced by the cyclotron is delimited by a collimator with a diameter of 3.4 cm and the beam intensity homogeneity inside the collimator area, measured by means of alanine dosimeter and read with Bruker e-scan Alanine Dosimeter Reader (estimated error of 2%), varies less than 20% from the peak intensity. The proton current was monitored with a Faraday cup from which the proton fluence was calculated. The total irradiation duration to achieve the final fluence of 10^{21} p/m² has been of 14 hours and the estimated temperature increase induced by radiation was less than 10 °C.

Proton irradiations at 24 GeV up to fluences of 1.38×10^{21} p/m² have been performed at the Proton Synchrotron (PS) at CERN, IRRAD1 facility [135]. The Nb₃Sn wires are inserted in paperboard sample holders and fixed with adhesive Kapton tape; the beam homogeneity inside the active area of sample holder (5 mm²) was 97%. The accumulated proton dose has been determined by measuring the activation of aluminum samples that were irradiated simultaneously with the Nb₃Sn wires and the total irradiation duration to achieve 1×10^{21} p/m² has been of about 2 years. Due to the relatively low proton fluence with respect to that one produced with the UCL facility, the temperature increase induced by 24 GeV proton irradiations can be neglected.

For both the facilities the beam direction was chosen perpendicular to the wire axis.

3.1.2. Proton irradiation on Nb₃Sn platelets: the Bragg peak experiment

In view of the quadrupoles in the HL-LHC upgrade accelerator it is important to have a complete characterization of the damage induced by the radiation environment. As mentioned above, in the irradiation experiment on the wires at energies of 65 MeV and 24 GeV, the Bragg peak is located outside the Nb₃Sn wires (diameter ≤ 1 mm), see Table 4.

However, the high energy protons and secondary ions enter into the quadrupole of LHC Upgrade under various angles and for a certain amount of these charged particles the Bragg peaks will be located inside the inner windings of the quadrupole, thus inside the superconductor and also inside the stabilizing copper.

As shown in [Figure 35](#), the damage caused by the charged particles at the location of the Bragg peak will be more important than that one caused by the protons just traveling through the wire (steady loss region). It follows that both kinds of damage have to be considered separately: a homogeneous damage in *the steady loss region* and an inhomogeneous one (i.e. higher damage localized in a smaller volume of the sample) in *the Bragg peak region* (see [Figure 35](#)).

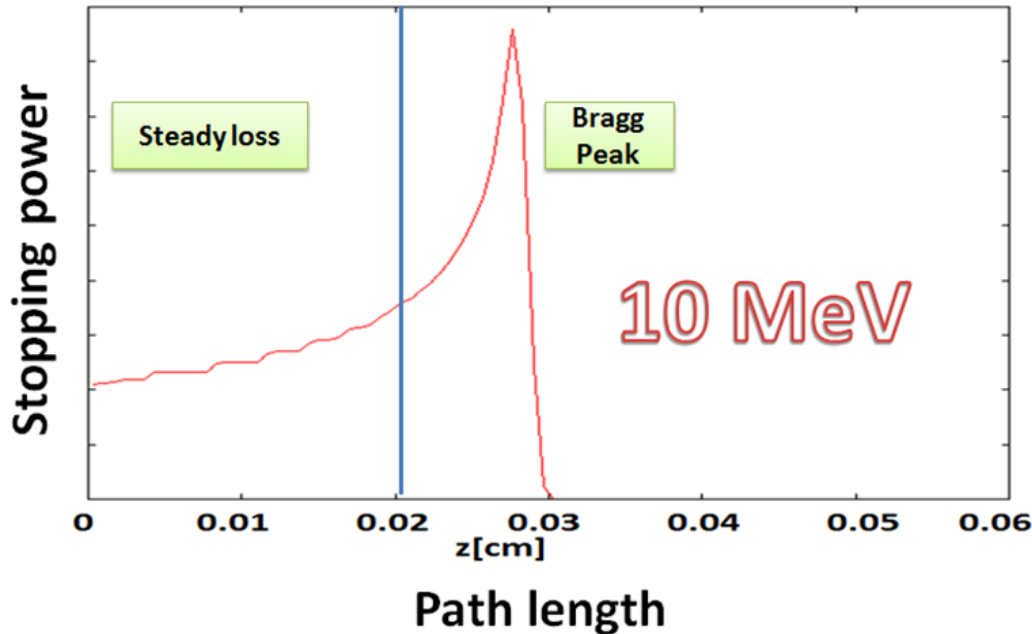


Figure 35 The expected proton penetration depth in Nb_3Sn platelets following FLUKA calculations at 10 MeV. We will refer to the initial part of the stopping power as *Steady loss* and the region around the maximum of the proton energy loss as *Bragg Peak*.

It should be noted that the calculation of dpa values in the inner quadrupoles of HL-LHC behind the W shield have been performed by F. Cerutti, A. Lechner, L. Esposito et al. [136], who studied the thermal stability conditions for the irradiated quadrupoles. In contrast the calculation

of the dpa values of irradiated wires were determined in the frame of the present work, the study of the corresponding physical properties of irradiated Nb_3Sn wires being our main goal.

At present, little is known about the two quantities that characterize the local damage at the Bragg peak penetration depth, i.e. the radius of the damage zone at the Bragg peak location (in the superconductor and in the Cu stabilization matrix) and the effect of the transmitted energy (in the Bragg peak zone) to the Nb_3Sn filaments as well as its local effect on both the crystal structure and on the superconducting properties.

The Bragg peak experiment is aimed to answer these questions and is performed irradiating with 10MeV protons stacks of Nb_3Sn platelets as will be described hereafter.

Following these ideas two situations are encountered by protons when traveling through the matter:

1. Steady energy losses (Bragg peak outside the Nb_3Sn platelets). The Bragg peak is outside the Nb_3Sn platelets. For this special case, the damage behavior is analyzed in an analogous way to that one caused by neutron irradiation: the damage is homogeneous. However, due to the proton charge, the effect is much stronger than for neutron irradiation; the maximum values of J_c/J_{c0} being expected at considerably lower fluences than those found for neutron irradiation.
2. Energy loss at the Bragg Peak (Bragg Peak inside the Nb_3Sn platelets). Here the whole energy is transmitted to the matrix at the Bragg peak location, a locally confined region. A much higher damage is expected in these inhomogeneously distributed regions.

The lowering of atomic order parameter and of T_c values are the quantities to be investigated in both cases.

NRC KI facility and arrangement of the Nb₃Sn platelets during proton irradiation

Proton irradiation on Nb₃Sn platelets at 10 MeV up to fluences of $1 \times 10^{22} \text{ p/m}^2$ have been performed at the cyclotron of the National Research Centre in Kurchatov Institute (NRC KI, Russia).

The direction of the proton beam is perpendicular to the Nb₃Sn platelets and the distance between the beam and the target sample in the beam channel is 3 m.

The shape of the beam is Gaussian but beam restoring by scanning is used to achieve uniformity of irradiation. Thus, the actual distribution is uniform with “Gaussian” edges and the beam diameter is 2 cm. The energy spread is less than 1 % and the angular spread in the channel is 1.5 degrees. Beam restoring adds to this value about 0.5 degrees thus the overall angular spread is 2 degrees.

The stack of Nb₃Sn platelets (details discussed later in this paragraph) is wrapped securely by a 20 μm thick Al foil and is located in the central part of the beam in the corners of square with edges 5-10 mm.

In [Figure 36](#) a schematic drawing of the target unit and of the sample holder are shown. The samples are directly cooled by water. The energy loss in the Al foil (100 μm), the residual water (10 μm) and the wrapping foils (20 μm) is estimated to be around 1 MeV. Dosimetry is performed by charge measurement (Faraday cup).

The thickness of each platelet and its arrangement with respect to the proton beam were planned taking into account the penetration depth for 10 MeV, the thinnest platelet being just located at the position of the Bragg peak: from FLUKA simulation [1], the proton penetration depth is 300 μm . In [Figure 37](#) the sequence and the thickness of the platelets are reported for each proton fluence.

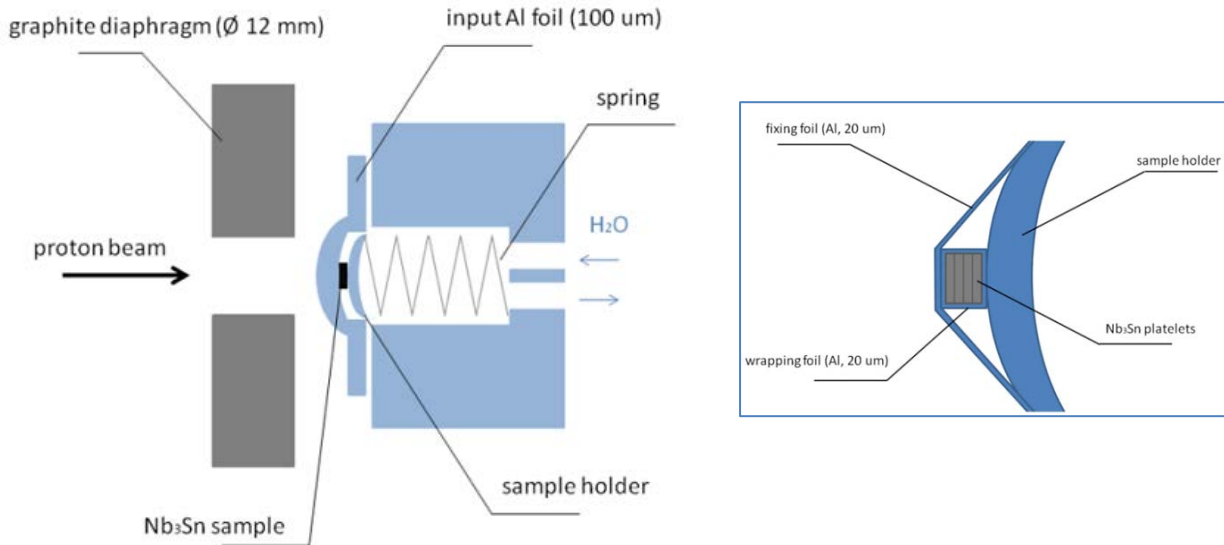


Figure 36 Schematic drawing of the target unit (left) and of the sample holder (right) for the irradiation of Nb₃Sn platelets. The residual cooling water layer (10 µm thick) between platelets and sample holder is not shown here.

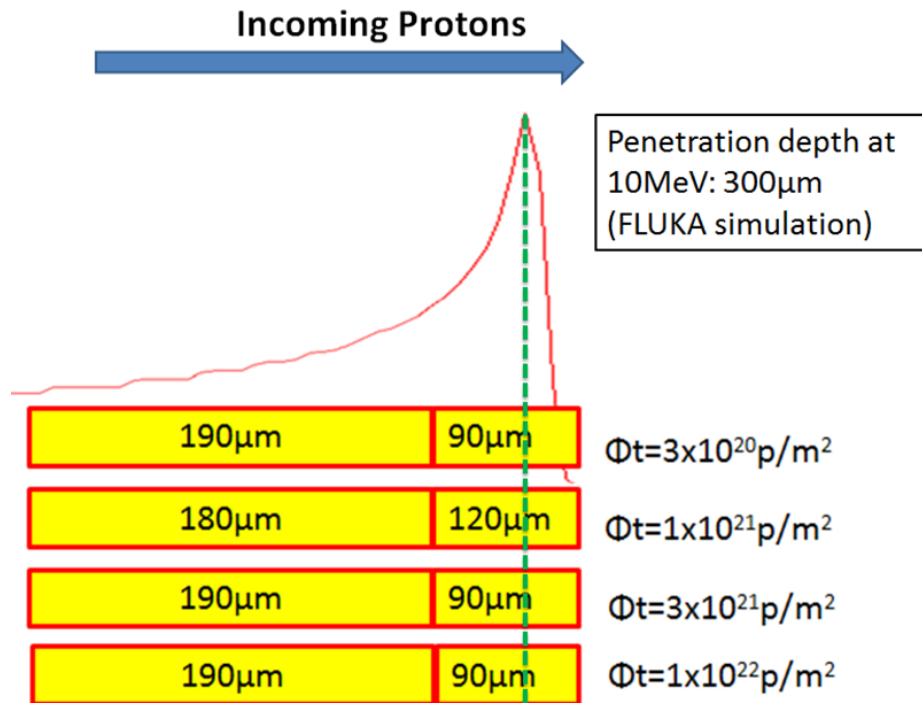


Figure 37 Planning of the arrangement of Nb₃Sn platelets for 10MeV proton irradiation (penetration depth in Nb₃Sn from FLUKA simulation: 300 µm)

However, for the experiment, the calculated penetration depth is corrected at the Kurchatov Institute taking into account the thickness of cooling H_2O as well as the Al needed for holding the samples. In addition during the experiment many platelets were broken and thus the planned measurements, shown in [Figure 37](#), were reduced to three fluences: 3×10^{20} , 3×10^{21} and $1 \times 10^{22} \text{ p/m}^2$. In [Figure 38](#) the configuration of the platelets and Al envelope with respect to the proton beam is shown.

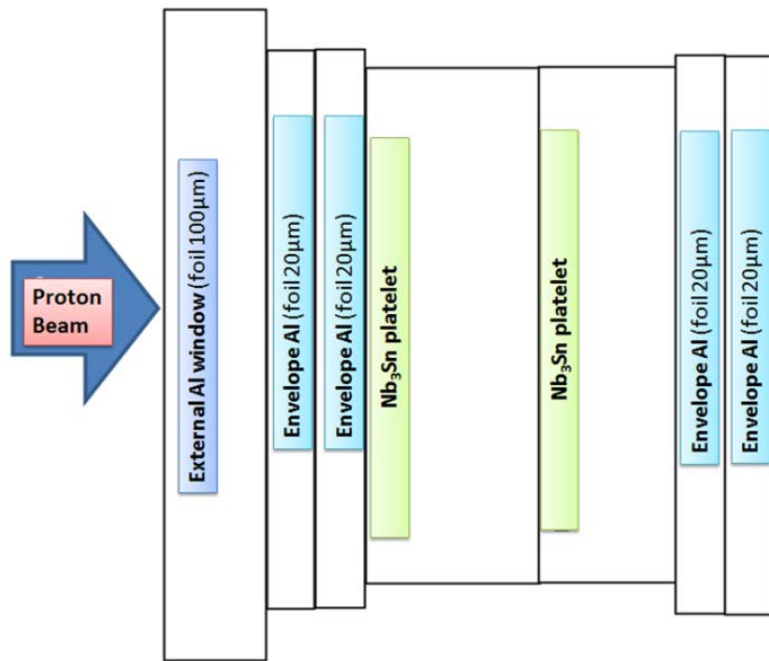


Figure 38 Configuration of the Nb_3Sn platelets and Al foils with respect to the proton beam. (Courtesy of Alexander Ryazanov)

3.1.3. Radioactivity on Nb_3Sn wires and thin platelets (safety condition at CERN)

Before measuring the irradiated Nb_3Sn wires and platelets a careful determination of the radioactivity of such sample has to be done (allowed dose limit: $1 \mu\text{Sv/h}$).

To this aim, FLUKA simulations have been accomplished by Otto and coworkers [132]. They estimated the activation and the ambient dose equivalent rate at 10 cm distance ($H^*(10)$) of $\text{Nb}_3\text{Sn}/\text{Cu}$ RRP wires (#7419 and #11967). This simulation was performed assuming an overall wire composition of 0.59 vol.% Cu, 0.28 vol.% Nb, 0.13 vol.% Sn and either 0.09 vol.% Ta or 0.02 vol.% Ti and a mass of 21 g. The simulation results obtained for 3 proton energies

(35 MeV, 1.4 GeV and 24 GeV) after a fluence of 10^{19} p/m² are shown in [Figure 39](#) for the Ta alloyed RRP wire.

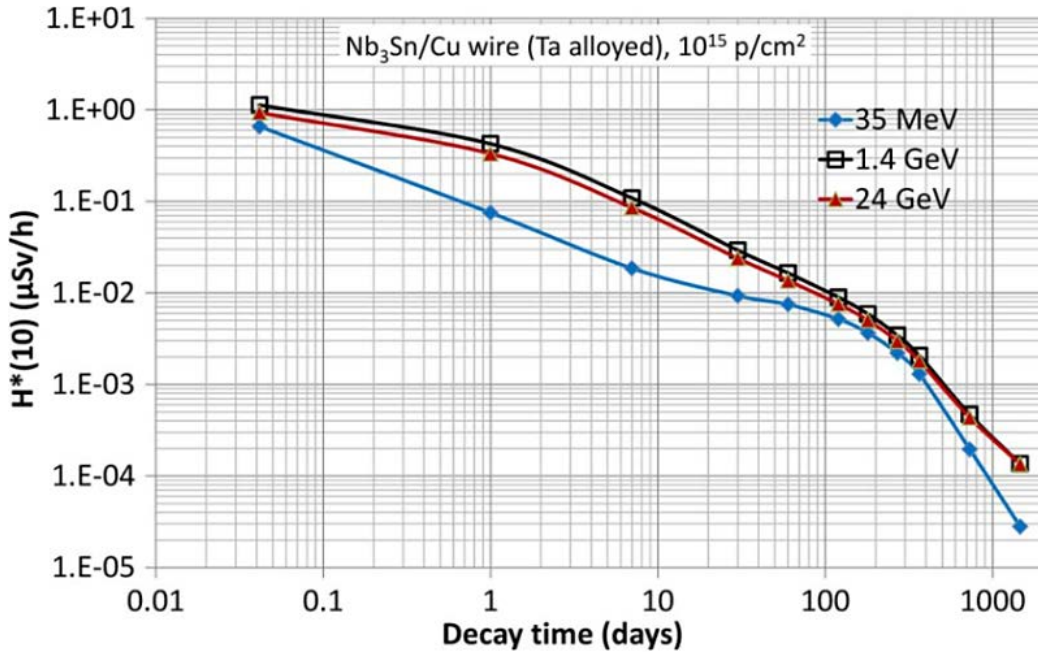


Figure 39 Calculated decay time dependence of the ambient dose equivalent rate at 10 cm distance ($H^*(10)$) of Nb₃Sn/Cu RRP type wire #7419 with a mass = 21 mg, after irradiation to a maximum fluence of 10^{19} p/m² accumulated during 5 days. From Otto et al. [136].

For identical irradiation conditions no significant difference was observed in the activation of Ti and Ta alloyed wires. At higher fluence (10^{21} p/m²) the waiting time to get an activation dose at 10 cm, $H^*(10)$, below the legal limit of 1 $\mu\text{Sv/h}$ was 100 days. It was observed that 35 MeV proton irradiation leads to significantly lower Nb₃Sn wire activation when compared to 1.4 GeV and 24 GeV irradiation.

Considering a thickness of 0.25 mm, a diameter of 15 mm (side of about 10 mm) and a mass of 440mg the time needed to reach $H^*(10) = 1 \mu\text{Sv/h}$ of 10^{21} p/m² can be approximately found to 15months.

3.2. Magnetization measurements

In this section VSM (Vibrating Sample Magnetometer) and AC susceptibility measurements adopted to obtain respectively the critical current density J_c and the critical temperature T_c of Nb₃Sn wires before and after proton irradiation are described. These measurements were performed at CERN by David Richter.

The determination of the critical current density after proton irradiation by magnetization offers a number of advantages over transport measurements. First of all, assuming the same proton fluence and decay time, the radioactive dose rate of short magnetization samples is more than one order of magnitude lower than for longer transport samples, thus reducing the problem of radiation protection during handling and storage of the samples. Magnetization measurements are not sensitive to possible crack formation occurring during the handling of the brittle Nb₃Sn. From an operative point of view magnetization measurements can be performed in temperature and field ranges which are normally not accessible (in small samples) by means of transport measurements due to the high critical currents (≥ 1000 A). In addition, the stability problems associated with transport measurements in a gas cooled mode are avoided [124]. Finally, it is possible to irradiate small samples with higher proton fluences; indeed the proton beam can be focused to a smaller cross section, resulting in a more homogeneous proton intensity distribution across the sample [132].

3.2.1. VSM measurements to obtain J_c

The magnetization hysteresis of the superconducting wires at different temperature, from 4.2 K up to 14 K, was acquired by means of a Vibrating Sample Magnetometer (VSM) manufactured by Cryogenic, Ltd., London & Oxford and modified at CERN by David Richter.

The measurements were performed in a He gas flow by sweeping the applied field perpendicular to the wire axis, between 0 and 10.5 T with steps of 250 mT while increasing and decreasing the field (rate of 500 mT / min for each step). The temperature was monitored with three Cernox thermometers. The signal is detected by an astatic pair of pick-up coils located inside the

Variable Temperature Insert (VTI) within the bore of the superconducting magnet. The coils are arranged to give zero resultant external magnetic field when a current passes through them and to have zero e.m.f. induced in them by an external magnetic field. The signal is detected by a lock-in amplifier. The magnetometer has an automated gas handling system, and the sample is loaded through an airlock [137].

The VSM is based upon Faraday's law according to which an e.m.f. is induced in a conductor by a time-varying magnetic flux. A sample magnetized by a homogeneous magnetic field is vibrated sinusoidally at a small fixed amplitude with respect to stationary pick-up coils [138]. The magnetic dipole moment of the sample will create a magnetic field around the sample, called magnetic stray field [139]. As the sample is moved up and down, this magnetic stray field is changing as a function of time, $\partial\mathbf{B}(t)$. The resulting field change $\partial\mathbf{B}(t)$ at a point \mathbf{r} inside the detection coils, according to Faraday's law, induces a voltage, detected by the pick-up coils and given by:

$$V(t) = \sum_n \int_A \frac{\partial\mathbf{B}(T)}{\partial T} \cdot d\mathbf{A} \quad 38$$

where \mathbf{A} is the area vector of a single turn of the coil and the summing is done over n turn of the coils. $\mathbf{B}(T)$ is given by the dipolar approximation assuming small dimensions of the magnetized sample in comparison to its distance from the detection coils:

$$\mathbf{B}(r) = \frac{\mu_0}{4\pi} \left(\frac{\mathbf{m}}{r^3} - \frac{3(\mathbf{m} \cdot \mathbf{r}) \cdot \mathbf{r}}{r^5} \right) \quad 39$$

And

$$\frac{\partial\mathbf{B}_i(t)}{\partial t} = \frac{\partial\mathbf{a}(t)}{\partial t} \cdot \nabla_r \{B(r)\}_i$$

$\mathbf{a}(t)$ is the position vector of the dipole and $\{B(r)\}_i$, $i=1,2,3$ the i -th component of \mathbf{B} at \mathbf{r} due to dipole \mathbf{m} (emu, $1 \text{ emu} = 10^{-3} \text{ A m}^2$). $V(t)$ is amplified by a lock-in amplifier. For stationary pick up coils and a uniform and stable external field, the only effect measured by the coils is that due

to the motion of the sample. The voltage $V(t)$ is thus a measure of the magnetic moment, \mathbf{m} , of the sample [138].

Knowing the magnetic moment of the sample (\mathbf{m}), the critical current density in the A15 layer, ($J_c(A15)$) before and after proton irradiation, is evaluated with the approximation method described in the following section; the upper critical fields before irradiation, B_{c20} , and their increment after irradiation were determined by means of the pinning force analysis which will be described in Subsection 4.1.3.

Evaluation procedure to obtain J_c

The critical current density was obtained from the measured magnetic moment \mathbf{m} . Under the hypothesis that a type II superconductor is fully penetrated and that the critical current density, J_c , is constant in the entire sample volume (Bean model [140]) the magnetic moment as a function of the critical current density J_c is given by:

$$\mathbf{m} = J_c \frac{1}{2} \int \mathbf{r} \times \mathbf{e}_j(\mathbf{r}) d^3r \quad 40$$

where $\mathbf{e}_j(\mathbf{r})$ is the local direction of the current. The proportionality factor between \mathbf{m} and J_c is hence determined by the sample geometry and the magnetization history.

For the multifilamentary Nb_3Sn wires under investigation (RRP and PIT type) the basic superconductor geometry is a helical tube (i.e. several twisted hollow sub-elements). Since the evaluation of the proportionality factor for this geometry is very complex, the problem is simplified assuming each subelement as parallel superconductive hollow cylinder. This condition is only ensured if the twist pitch length is much greater than the wire diameter and the subelement cross section not too different from a circular geometry.

Assuming that the coupling between the subelements is negligible, the critical current density is:

$$J_c = \frac{3}{4} \frac{m_{irr}}{NL(\rho_o^3 - \rho_i^3)} \quad 41$$

where N is the number of subelements, L is the sample length, ρ_o and ρ_i are the outer and inner radii of the hollow cylinder (see Subsection 2.1.1) and m_{irr} is the irreversible magnetic moment

of the sample defined as: $m_{irr} = \frac{m_+ - m_-}{2}$ and m_+ and m_- are the magnetic moments measured during decreasing and increasing applied field, respectively (Figure 40). In Figure 41 the critical current density before irradiation evaluated with the described method for the three wires under study is shown.

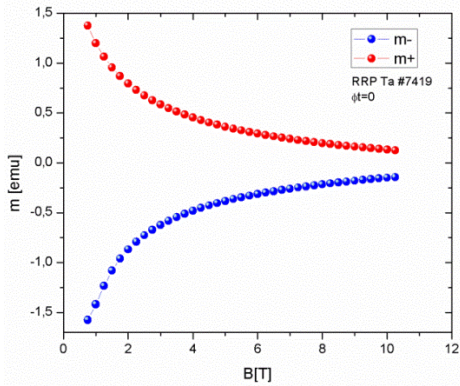


Figure 40 Upper and lower branch of the hysteresis curve at 4.2K for RRP Ta alloyed wire (#7419) before irradiation.

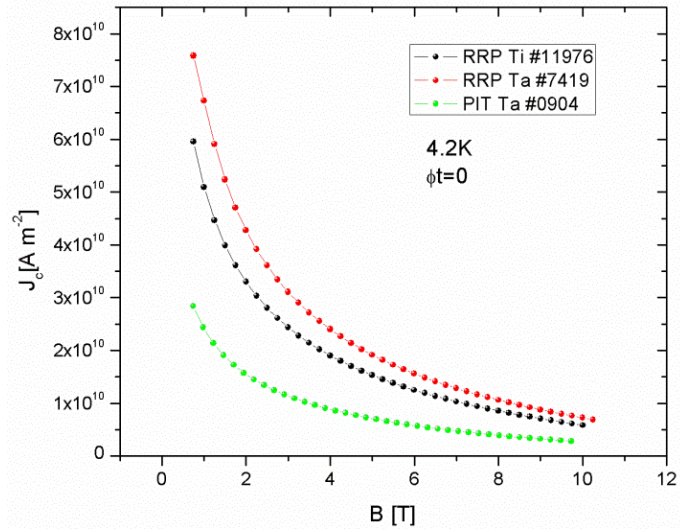


Figure 41 Critical current densities at 4.2K before proton irradiation for the three wires under study: RRP Ti alloyed (#11976), RRP Ta alloyed (#7419), PIT Ta alloyed (#0904) (see Figure 21 and Table 2).

In agreement with T. Baumgartner [124], the self-field correction can be neglected in this model. Indeed, by a computer simulation and measuring a four-quadrant magnetization loop he found a negligible self-field (B_{sf}) of ~ 0.14 T.

3.2.2. AC susceptibility measurements to obtain T_c

The AC susceptometer option of the VSM previously described uses a small primary excitation coil to apply an AC field (with amplitude of 2 mT and a frequency of 40.8 Hz) to the sample

wire. Inside the primary coil, secondary pick-up coils are wound in the opposite directions and electrically connected in series. The pick-up coils occupy opposite halves of the primary coil volume. The sample is placed in one of the pickup coils (the sample coil) while the other pickup coil (the reference coil) is left empty [141].

The ac voltage V across the secondary coil is: $V = -\frac{d\phi}{dt}$, where ϕ is the net flux through the entire secondary loop (both the sample and reference coil). It includes contributions from both the applied field and the field due to the sample magnetization. Since the two pick-up coils are wound in opposite directions and connected in series, the net secondary flux due to the applied field will be small, the signal V being thus mainly due to the sample magnetization M . This signal is measured using a Lock-In amplifier with the in-phase and out-of-phase components of the signal that are proportional, respectively, to the real and imaginary components of the AC susceptibility of the sample, $\chi = -\frac{dM}{dH_{ext}} = (\chi' - i\chi'')$.

The real part of χ , χ' , reflects the screening properties of the superconductive sample, i.e. it corresponds to the energy difference between the normal state and the superconductive state, while the imaginary part of χ is proportional to the AC energy losses (i.e. the energy that is converted into heat).

Evaluation procedure to obtain T_c

From the real part of the AC magnetic susceptibility the critical temperature T_c was estimated as the midpoint of the transition: $T_c = \frac{T_1+T_2}{2}$, where T_1 and T_2 are the temperatures measured respectively at the off-set and on-set of the transition, as shown in [Figure 42](#).

For the PIT wires a double transition in the critical temperature has been measured reflecting the different temperature in the small and large grains (see Subsection 4.1.1 for further details).

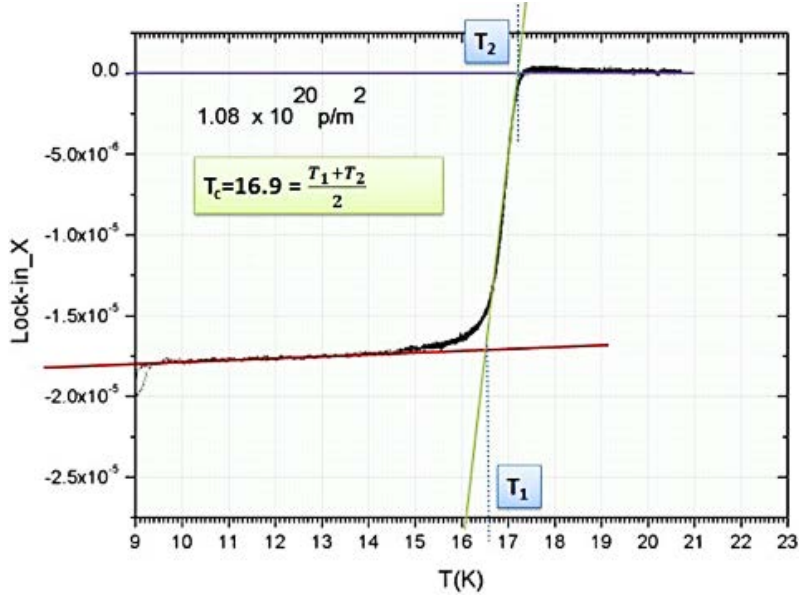


Figure 42 Evaluation of the critical temperature T_c for RRP Ti alloyed wire after proton irradiation at 24 GeV and fluence of $1.08 \times 10^{20} \text{ p/m}^2$

3.3. Diffraction measurements

The Bragg Williams LRO parameter, S , of the powdered Nb_3Sn sample #4 (see Section 2.2) before irradiation was determined by means of a Rietveld refinement procedure using the *Full Prof* software [33] on X – ray diffraction patterns of polycrystalline Nb_3Sn (from sample #4). The measurements were performed with the automatic diffractometer (λ_{Cu}) with $\text{CuK}\alpha_1$ Bragg Brentano geometry (configuration $\theta - 2\theta$) at the University of Geneva. Due to relative low peak intensities of X – ray diffraction patterns, very long exposure times had to be used to acquire sufficiently strong peak intensities to perform the refinement with a small statistical error; thus the measurements lasted about 15 hours with 3.5 seconds per step and with a sample spinning speed of 18 rpm.

Due to activation of the samples after irradiation, measurements could not be performed at the University of Geneva; it was thus decided to collaborate with the Kurchatov Institute (NRC-KI). However the local safety prescriptions did not allow to measure irradiated fine powders and the only possible alternative was to perform the diffraction measurements on Nb_3Sn platelets in their Synchrotron Radiation Source by Y. Zubavichus and coworkers.

Even if the intensity of diffraction pattern acquired with a synchrotron source is much higher than those obtained with a Bragg-Brentano diffractometer, the data are affected by preferential orientation because the samples cannot be rotated during the measurement.

To overcome texture problems and thus to determine with higher precision the Bragg Williams LRO parameter after 10 MeV proton irradiation, additional measurements were performed at NRC-KI in the resonant mode (REXD).

3.3.1. X-ray diffraction measurements at Unige (before irradiation)

Evaluation procedure to obtain S by Rietveld refinement

As will be explained in detail later on, the accuracy in the determination of S depends on several factors: the chemical composition, the atomic scattering factors, the preferred orientation and the microabsorption effects. All these features were taken into account during the refinement procedure to assure the reliability of the results.

To perform a good least – square minimization for a correct value of the LRO parameter, it is important to avoid false minima and divergence in early stages of the refinement. For this purpose it is essential to provide the best possible starting model collecting all the information available on the sample (cell parameters, atomic positions, occupation factors), on the diffractometer and on the experimental conditions of the data collection (zero-shift and resolution function of the instrument). In the *Full Prof* software these information are enclosed in the .pcr file, shown in [Figure 43](#), where 19 parameters were inserted to refine the phase of the Nb_3Sn powder after formation at 1'250°C (see Subsection 2.2.1 for further details on the Nb_3Sn phase formation); among these parameters two of them were used to refine the scale factor and the lattice constant of NbO phase. NbO phase was added to reflect the real state of the measured Nb_3Sn powder. Indeed, due to the preparation using very fine initial powders which already contained a certain amount of oxygen, our samples are found to contain a small amount of oxygen. By means of Hot Extraction by the Mikroanalytisches Labor Pascher (Germany), the total amount of oxygen was determined to 0.14wt.% (approximately 1 at.%), that one of Carbon

to 0.01wt.%. As shown in [Figure 43](#), special numbers named *codeword* are used to control the refined parameters: for example, a zero codeword means that the parameter is not being refined.

```
!
! 19 !Number of refined parameters
!
! Zero Code Sycos Code Sysin Code Lambda Code MORE ->Patt# 1
! 0.00000 181.0 0.00000 0.0 0.00000 0.0 0.000000 0.00 1
!
! Microabsorption coefficients for Pattern# 1
! P0 Cod_P0 Cp Cod_Cp Tau Cod_Tau
! 0.0000 0.00 3.0000 0.00 0.1630 191.00
!
! Data for PHASE number: 1 ==> Current R_Bragg for Pattern# 1: 3.51
!
Nb3Sn_1
!
! Mat Dis Ang Pr1 Pr2 Pr3 Jbt Irf Isy Str Furth
! 4 0 0 0.0 0.0 1.0 0 0 0 0 0
! ATZ Nvk Npr More
! 100.000 0 5 0
!
! P m 3 n
! Atom Typ <--Space group symbol
! Nb1 NB X Y Z Biso
! 0.25000 0.00000 0.50000 0.56000
! 0.00 0.00 0.00 101.00
! 0.00 0.00 0.00 61.00
! Sn1 SN 0.25000 0.00000 0.50000 0.56000
! 0.00 0.00 0.00 101.00
! -61.00
! Sn2 SN 0.00000 0.00000 0.00000 0.56000
! 0.00 0.00 0.00 101.00
! 1.80537 0 0 0
! -71.00
! Nb2 NB 0.00000 0.00000 0.00000 0.56000
! 0.00 0.00 0.00 101.00
! 0.20946 0 0 0
! 71.00
!
! -----> Profile Parameters for Pattern # 1
! Scale Shape1 Bov Str1 Str2 Str3 Strain-Model
! 0.31641E-06 0.50000 0.00000 0.00000 0.00000 0.00000 0
! 11.00000 0.000 0.000 0.000 0.000 0.000
! 0.013073 -0.000176 0.015243 0.000000 0.000000 0.000000 0.000000 0
! 31.000 41.000 51.000 0.000 0.000 0.000 0.000
! a b c alpha beta gamma #cell Info
! 5.288 5.288 5.288 90.000000 90.000000 90.000000
! 21.00000 21.00000 21.00000 0.00000 0.00000 0.00000
! Pref1 Pref2 Asy1 Asy2 Asy3 Asy4
! 1.00000 0.00000 0.00000 0.00000 0.00000 0.00000
! 0.00 0.00 0.00 0.00 0.00 0.00
!
```

Figure 43 The .pcr file. Green rectangular frame: values to be refined for the different parameters; red oval frame: the codewords values; blue triangles: the numbers of atoms.

Three microabsorption coefficients were introduced in the structural model, in order to obtain positive values for the isotropic temperature factor (further details are given below) and a set of linear constraints were inserted in the typical .pcr file to connect the atoms involved in the site exchange mechanism (see [Figure 44](#)). The reduction of the degree of freedom by inserting a linear combination between the occupation numbers was necessary to avoid divergences during the refinement process.

The structural parameters were not all refined at the same time to avoid that some of them affect strongly the residuals (these must be refined first) while others produce only little improvement

and thus should be held fixed until the latest stages of the analysis. Thus, the parameters to refine should follow the sequence: scale factor, atomic positions, peak shape and asymmetry parameters, atom occupancies, isotropic temperature factor, microabsorption parameters.

As explained in Subsection 1.2.2, the occupation factor is one of the most important refineable parameter that influences the determination of the S value. Therefore the condition for site exchange between atoms has to be introduced into the model for obtaining meaningful values for the occupation numbers ([Figure 44](#)). It must be noticed here that “*site exchange*” means the mutual exchange of the site between two atoms and it should not be confused with the displacement definition that occurs when an atom moves from its original site to occupy the site of another atom or a vacancy. The starting values of the occupation numbers were chosen accordingly with the chemical composition, 24.8at. %Sn. This value for the chemical composition was found to be the best one giving the lower values for the agreement factors.

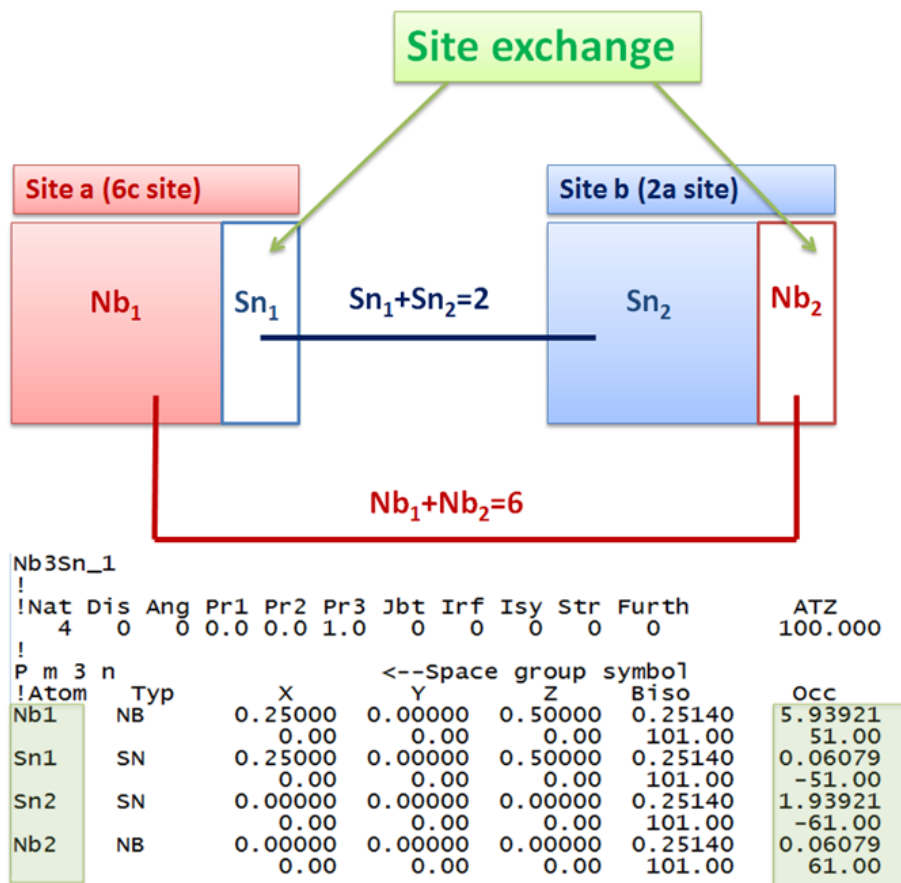


Figure 44 The site exchange between Nb and Sn atoms (on the top) and the refined occupation numbers (on the bottom). The values of the occupation numbers were chosen so that: $\text{Nb}_1 + \text{Nb}_2 = 6$ and $\text{Sn}_1 + \text{Sn}_2 = 2$.

Factors influencing the determination of S during the refinement procedure

As pointed out by Flükiger [18], the most important criterion for the accurate determination of the order parameter is the relative intensity of the A15 *superstructure* lines, represented by the term $n^*S(f_B-f_A)$ in [Figure 45](#), where $n=0,1,2,\dots$. The *superstructure* lines in A15 structure are: (110), (220), (310), (411), (422), (510), (530) and (620) reflections (see also Sweedler et al. [39]).

As previously explained in Subsection 2.2.4, it is obvious that if the form factor for the B atom, f_B , approaches that one for A atom, f_A , the determination of the order parameter from X – ray diffractometry becomes more and more uncertain, the intensity of the superstructure lines tending to zero.

hkl	S Contribution to F	hkl	S Contribution to F
110	$2S(f_B - f_A)$	420	$S(f_B - f_A) + (3f_A + f_B)$
200	$S(f_B - f_A) + (3f_A + f_B)$	421	$S(f_B - f_A) - (3f_A + f_B)$
210	$S(f_B - f_A) - (3f_A + f_B)$	332	$S(f_B - f_A) + (3f_A + f_B)$
211	$S(f_B - f_A) + (3f_A + f_B)$	422	$2S(f_B - f_A)$
220	$2S(f_B - f_A)$	510,431	$2S(f_B - f_A)$
310	$2S(f_B - f_A)$	520,432	$S(f_A - f_B) + (3f_A + f_B)$
222	$3S(f_B - f_A) - (3f_A + f_B)$	521	$S(f_B - f_A) + (3f_A + f_B)$
320	$S(f_A - f_B) + (3f_A + f_B)$	440	$2(3f_A + f_B)$
321	$S(f_B - f_A) + (3f_A + f_B)$	530,433	$2S(f_B - f_A)$
400	$2(3f_A + f_B)$	600,442	$S(f_B - f_A) + (3f_A + f_B)$
411,330	$2S(f_B - f_A)$	610	$S(f_B - f_A) + (3f_A + f_B)$
		611,532	$S(f_B - f_A) + (3f_A + f_B)$

Figure 45 Contribution of the long-range order parameter, S, to the structure factor, F, for stoichiometric compounds of the A15 structure [18]

Other factors influencing the determination of the Bragg – Williams LRO parameter are the presence of additional phases, the homogeneity in the composition, the residual stresses, the thermal and irradiation history, the microabsorption and the preferred orientation (or texture) [32].

It is very difficult to prepare a 100 % single phase sample of Nb₃Sn. One reason is due essentially to the affinity of this compound for the oxygen, which is picked up during the handling of the powder (see Subsection 2.2.4) before the HIP process, giving rise to the formation of a second phase of NbO. Fortunately the additional lines of NbO phase do not overlap with those of Nb₃Sn: for a good analysis, it is sufficient to introduce this phase in the refinement procedure and refine both the phases at the same time.

Microabsorption is a problematic factor affecting accuracy in Quantitative Phase Analysis (QPA) via XRD. This effect occurs when the sample contains phases with different mass absorption coefficients and/or particle size distributions. Consequently the intensities of reflections from the heavily absorbing phases are suppressed while those from lighter absorbers are effectively enhanced. This subsequently misrepresents the derived relative abundance of the phases. A detail discussion of the effect can be found in Zevin and Kimmel [142]. For those samples where the effects of microabsorption are present Brindley has defined the so-called particle absorption factor as:

$$\tau_\alpha = \frac{1}{Vol_k} \int_0^{Vol_k} \exp[-(\mu_\alpha - \mu)D] dVol_k \quad 42$$

where μ_α is the Linear Absorption Coefficient (LAC) of phase α , μ is the average LAC of the entire sample and D is the effective dimension of the particle and Vol_k is the particle volume¹².

Given the limitations of current microabsorption correction algorithms, the best approach is to minimize the effect, where possible, before data collection is undertaken. Examination of 42 shows that this can be achieved in two ways, namely:

- 1) Reduction of particle size.
- 2) Reduction of the absorption contrast. Sometimes this can be simply achieved through a change in the wavelength used to collect the diffraction data [143].

¹² There are several limitations in the Brindley correction that arise from the range of applicability of the model (for coarse sample, μD is typically in the range 0.1 to 1.0) and the difficulty in defining an appropriate value for D .

In the *Full Prof* software, the problem of microabsorption leading to negative values of the temperature factor (B_{iso}) was solved by Pitschke et al. [144] introducing the refinement parameters, P_0 and C_p in the formula:

$$P(h) = P_0 + C_p \frac{\tau}{\sin \vartheta_h} \left(1 - \frac{\tau}{\sin \vartheta_h} \right). \quad 43$$

The best values for τ , P_0 and C_p are found to be around 0.16, 0.00 and 3.00 respectively.

A complete description of the preferred orientation is given by the orientation distribution function (ODF) that is based on the probability to find a particular crystallite orientation within the sample. For an ideally random powder the ODF is the same everywhere (ODF=1) while for a textured sample the ODF will have positive values both smaller and larger than unity [143].

In *Full prof* two preferred orientation functions are currently implemented:

1. The exponential function:

$$P_h = G_2 + (1 - G_2) \exp(G_1 \alpha_h) \quad 44$$

where G_1 and G_2 are refineable parameters and α_h is the acute angle between the scattering vector and the normal to the crystallites (*platy habit*).

2. Modified March's function:

$$P_h = G_2 + (1 - G_2) \left[(G_1 - \cos \alpha_h)^2 + \frac{\sin^2 \alpha_h}{G_1} \right]^2 \quad 45$$

where G_1 and G_2 are refineable parameters¹³. The parameter G_2 represents the fraction of the sample that is not textured [33].

Due to the high number of parameters already present in the model it was difficult to find a reasonable outcome to investigate the preferred orientation from these algorithms, a more direct method had been adopted.

This method consists in the evaluation of the intensity-ratios of two reflections for which the LRO contributions to the structure factor are identical¹⁴, (see [Figure 45](#)): I_{200}/I_{211} ; I_{420}/I_{211} ,

¹³ This expression is adapted to both fiber and platy habits: $G_1 < 1$: platy habit (α_h is the acute angle between the scattering vector and the normal to the crystallites); $G_1 = 1$: no preferred orientation; $G_1 > 1$: Needle-like habit (α_h is the acute angle between the scattering vector and the fiber axis direction)

I_{332}/I_{211} , ... (I_{211} corresponds to the highest intensity). Following this procedure, no preferred orientation has been revealed.

Empirical method to extrapolate the S value

In addition, an empirical method based on the X-ray experimental pattern acquired by means of Bragg-Brentano diffractometer has been developed mainly for two reasons:

1. to provide an additional proof that the S value found by Rietveld refinement on the powder diffraction data is not affected by preferential orientation;
2. to compare the results with those obtained from synchrotron data analysis (see “Synchrotron analysis after proton irradiation” in Subsection 4.2.1).

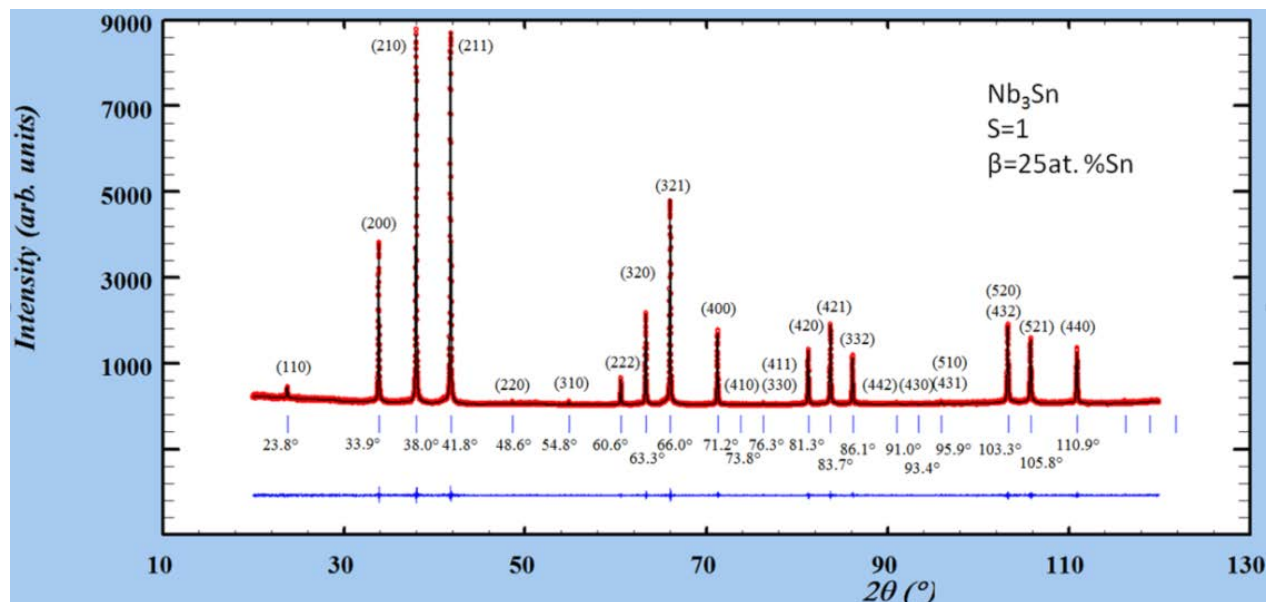


Figure 46 Theoretical Nb_3Sn pattern for $S=1$ obtained with *Full Prof* software.

¹⁴ In some cases, these ratios could be brought closer to the calculated values by repeated crushing and repacking of the powders.

This technique consists in comparing the measured intensity ratios with those calculated with a *Full Prof* simulation (described hereafter) as a function of S and thus verifying that the Rietveld refined S value is in agreement with the one extrapolated from the plot in [Figure 47](#).

Indeed the *Full Prof* simulation, developed in the present work, allows obtaining the Nb_3Sn theoretical diffraction pattern (thus the theoretical intensity ratios) as shown in [Figure 46](#).

The theoretical pattern of Nb_3Sn was obtained by means of a “fictitious” refinement performed by means of *Full Prof* software as follows: the .pcr file has been written assigning the theoretical values of the chemical composition ($\beta=25\text{at.\%Sn}$), the isotropic temperature factor ($B_{\text{iso}}=0.4$) and the lattice constant ($a=5.289\text{\AA}$). The set of the occupation numbers ($\text{Nb}_1, \text{Sn}_1, \text{Nb}_2, \text{Sn}_2$) have been introduced in the .pcr file for each value of S (=1; 0.9; 0.8; ..., 0) as:

$$\begin{aligned} \text{Nb}_1 &= 6\beta(S - 1) + 6 \\ \text{Sn}_2 &= 2\beta(1 - S) + 2S \\ \text{Sn}_1 &= s - \text{Sn}_2 \\ \text{Nb}_2 &= n - \text{Nb}_1 \end{aligned} \quad 46$$

Equations 46 come out directly from equation 2 (in Subsection 1.2.2), where $S = S_a = S_b$ ($\beta=25\text{at.\%Sn}$) and s and n are the sum of the Sn and Nb atoms (see [Figure 44](#)), i.e. $s=\text{Sn}_1+\text{Sn}_2=2$ and $n=\text{Nb}_1+\text{Nb}_2=6$, respectively.

Thus the theoretical patterns for each S values can be acquired launching the .pcr file with the ideal conditions just described above. From the .hkl files the ratio I_{hkl}/I_{211} have been calculated and plotted as a function of S, in [Figure 47](#).

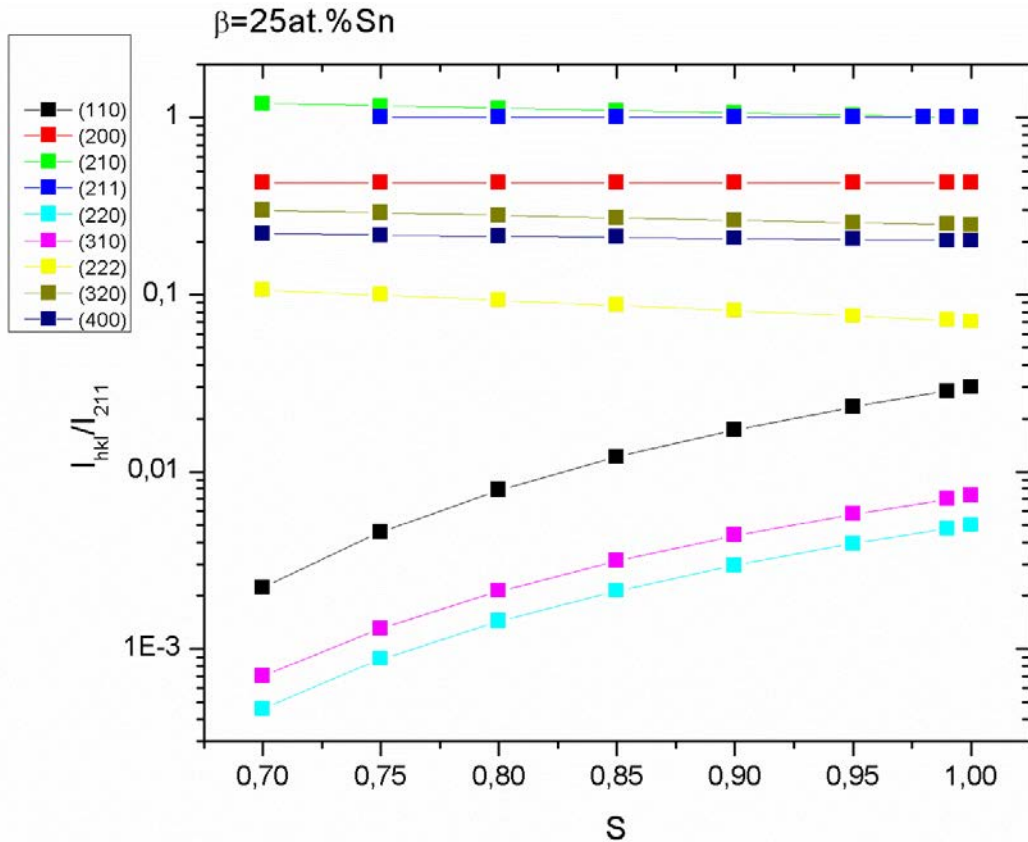


Figure 47 Simulated intensity ratios I_{hkl}/I_{211} as a function of S.

3.3.2. Synchrotron measurements at NRC-KI (after irradiation)

The Synchrotron measurements were performed at the “Structural Materials Science” Beamline at the NRC-KI Synchrotron Radiation Source by Y.V. Zubavichus and coworkers. A detailed description of the facility is described by Chernyshov et al. in [145].

The following parameters, reported in an internal report [145], were used to measure in the transmission geometry (Debye-Scherrer) the irradiated Nb_3Sn platelets (bulk #4):

- Beam size $200\times200\text{ }\mu\text{m}$; X-ray wavelength $\lambda=0.688862\text{ \AA}$ (normal mode) and $\lambda=0.653400\text{ \AA}$ (resonant mode, at the proximity of Nb K-edge);

- Monochromatization by a Si(111) channel-cut monochromator to $\Delta E/E \sim 2 \cdot 10^{-4}$;
- Sample-to-detector distance of 200 mm;
- FujiFilm ImagingPlate 2D position-sensitive detector;
- 30 min exposure time.

In order to improve the statistics and suppress texturing effects, a specific system to scan continuously the position of the sample with respect to the beam along x,y,φ-coordinates during X-ray exposure has been developed at the NRC-KI.

Raw 2D diffraction patterns were integrated using the Fit2D code. A pattern of polycrystalline Si (NIST SRM 640c) was used to calibrate geometry parameters, such precise sample-to-detector distance and tile of the detector plate.

The Rietveld refinement for all diffraction patterns were performed at NRC-KI using the Jana2006 code.

CHAPTER 4: RESULTS AND DISCUSSION

In this chapter the results obtained from the measurements and the evaluation procedures described in Chapter 3 are presented and discussed.

4.1. Results on Nb_3Sn wires

The initial values of the critical parameters for the three types of wires under study are reported in [Table 5](#).

Sample	J_{c0} (A15 layer) [10^9 Am^{-2}] 10 T; 4.2 K	T_{c0} [K]	B_{c20} [T] 4.2 K
RRPTi #11976	5.858	17.1	23.86
RRP Ta#7419	7.276	17.6	23.44
PIT Ta SG #0904	2.812	17.2	24.26
PIT Ta LG #0904	---	18.1	21.10

Table 5 Characterization of the Nb_3Sn wires prior to proton irradiation

For the PIT Ta alloyed wire reacted at 625 °C for 250 hours, two T_{c0} and B_{c20} values correspond to the two A15 regions with different grain sizes (see [Figure 48](#)), as results from a recent high field specific heat study by Senatore and Flükiger [147]: the larger grains (with a higher Sn content) show higher T_c , but lower B_{c2} values. As discussed in Subsection 4.1.3 the B_{c20} values given in [Table 5](#) for PIT wires have been calculated using pinning force function that takes into account the two small and large grained regions with different T_c and B_{c2} values.

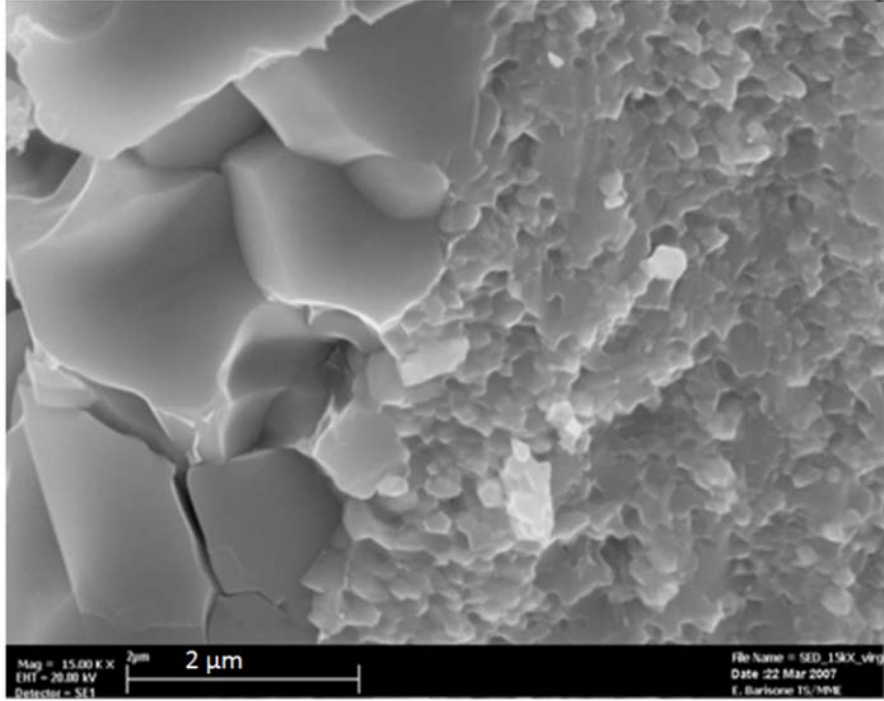


Figure 48 A SEM view (x 15000) of a PIT strand (B215) fractured sample reacted at 675°C during 84 hours showing both large (left) and small (right) grains by Boutboul et al. [147]

4.1.1. Decrease of T_c after proton irradiation

The linear decrease of T_c with fluence after proton irradiation at 24 GeV and 65 MeV is shown in Figure 49. The decrease of T_c at 24 GeV is larger for the RRP Ta alloyed wires than for the Ti alloyed wire in agreement with Weiss et al. [64] (see Subsection 1.2.3).

The linear decrease in Figure 49 was fitted by the relation $T_c = T_{c0} - k_T \Phi t$, where T_{c0} is the critical temperature in the unirradiated state (see Table 5) and k_T is the slope $dT_c/d\Phi t$, given in Table 6 for each Nb₃Sn wire. The k_T values are almost the same for the same sample at different energies. As will be explained in Subsections 4.1.4 and 5.3.1, the negligible difference between the slopes for the same sample irradiated at 65 MeV and at 24 GeV indicates that the damage induced by the two proton energies is similar.

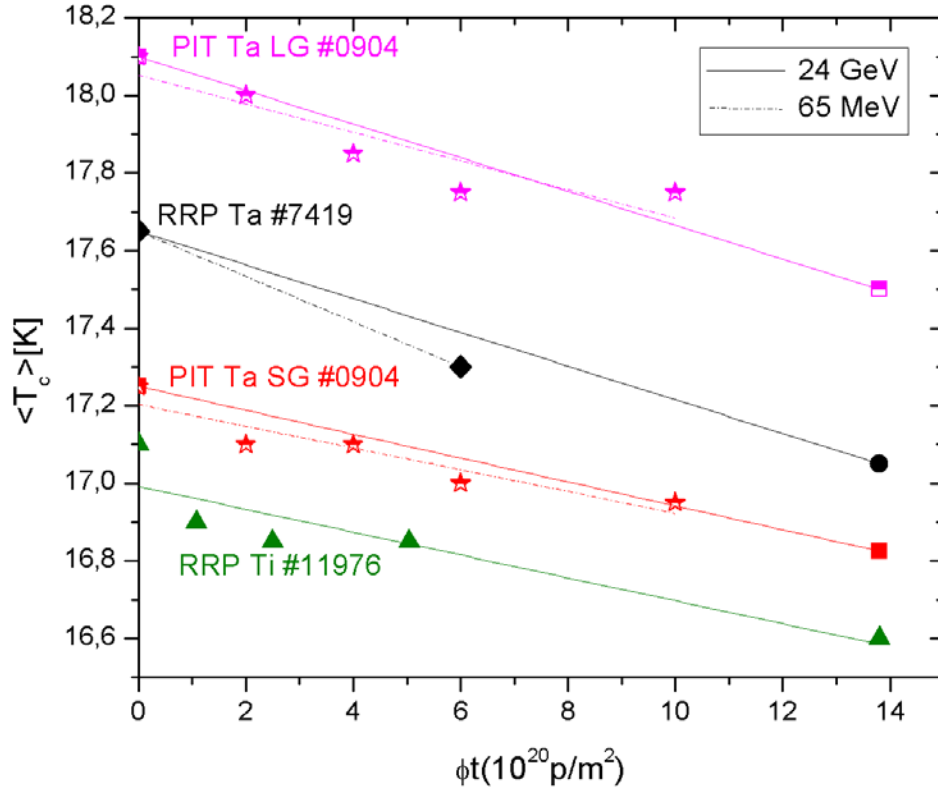


Figure 49 Linear decrease of the critical temperature with proton fluence for different types of Nb₃Sn wires. Full line refers to 24 GeV proton irradiation instead dashed lines to 65 MeV proton irradiation. From Spina et al. [149].

The small changes in the transition width, of the order of 0.2 K, indicate that the damage produced by proton irradiation is homogeneous, too, in analogy to neutron irradiation [77].

Wire type	24 GeV (IRRAD1)		65 MeV (UCL)
	K _T [10 ⁻²⁰ K p ⁻¹ m ²]	K _T [10 ⁻²⁰ K p ⁻¹ m ²]	
#7419	0.04±0.01		0.06±0.01
#0904SG	0.03±0.01		0.03±0.01
#0904LG	0.04±0.01		0.04±0.01
#11976	0.03±0.01		----

Table 6 Fit Parameters for the linear decrease of T_c with fluence.

4.1.2. Enhancement of J_c after proton irradiation

The critical current densities of Nb₃Sn wires before and after proton irradiation, $J_{c0} = J_c(0)$ and $J_c = J_c(\Phi t)$, respectively were obtained by means of magnetization measurements (see Subsection 3.2.1) using equation 41. All the wires at the proton energies 65 MeV and 24 GeV show an increase of the ratio J_c/J_{c0} , up to the highest fluence achieved in this work: i.e. $1.38 \times 10^{21} \text{ p/m}^2$. In Figure 50 and in Figure 51, the ratio J_c/J_{c0} is plotted as a function of fluence and for different applied fields, B , for the wires after irradiation with 65 MeV and 24 GeV protons, respectively.

The value of J_c/J_{c0} has not yet reached its maximum for any of the irradiated wires; the highest value at $8 \times 10^{20} \text{ p/m}^2$ for the Ta alloyed PIT wire irradiated at 65 MeV seems to indicate a peak within the error bar (5%), but further investigations above $1.4 \times 10^{21} \text{ p/m}^2$ would be needed to decide whether this is a maximum or not.

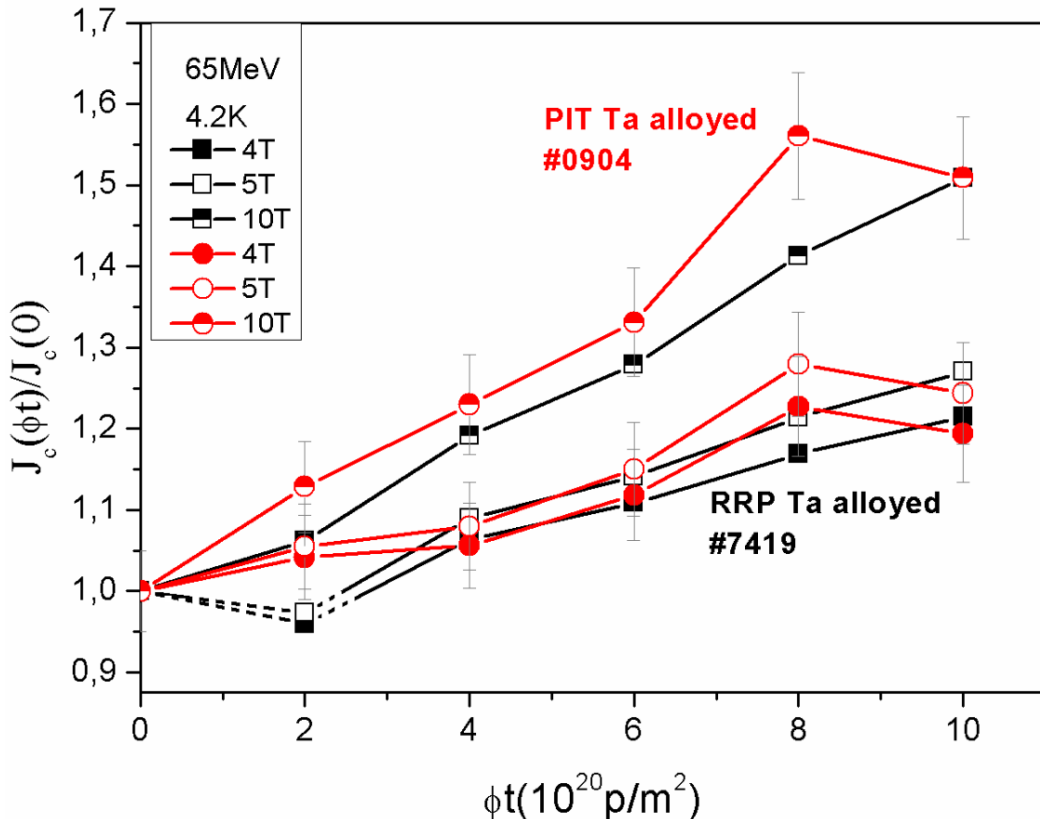


Figure 50 Enhancement of the critical current density with fluence after 65 MeV proton irradiation. The small decrease of J_c/J_{c0} (dashed line) up to $\sim 2 \times 10^{20} \text{ p/m}^2$ is due to flux jumps. From Spina et al. [150].

After proton irradiation, no difference was found between the two Ta alloyed PIT and RRP wires despite their different fabrication technique, thus demonstrating the importance of the alloying element on the radiation damage. Indeed, as shown in [Figure 51](#), the Ti alloyed RRP wire exhibits at 10 T and 24 GeV the highest increase of J_c/J_{c0} , reaching two times its initial value at the highest applied fluence while the maximum increase at the same applied field and proton energy for Ta alloyed wire reached only 1.5 and 1.7 for RRP and PIT respectively. The behavior for Ti and Ta alloyed wires is not the same due to the very different displacement cross section: Ti element have a smaller atomic weight with respect to that of Ta: 47.867 uma instead of 180.948 uma.

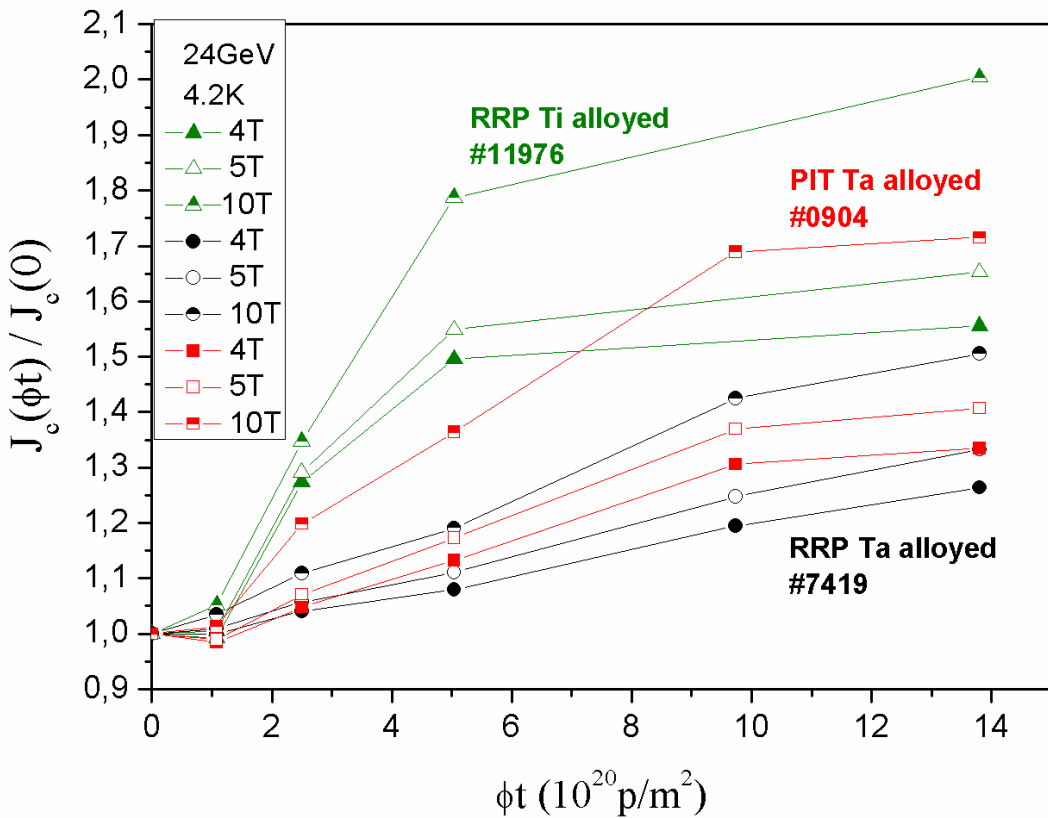


Figure 51 Enhancement of the critical current density with fluence after 24 GeV proton irradiation. From Spina et al. [149].

As mentioned above, a similar enhancement of J_c/J_{c0} is observed at 65 MeV and 24 GeV, as shown in [Figure 52](#) and in [Figure 53](#).

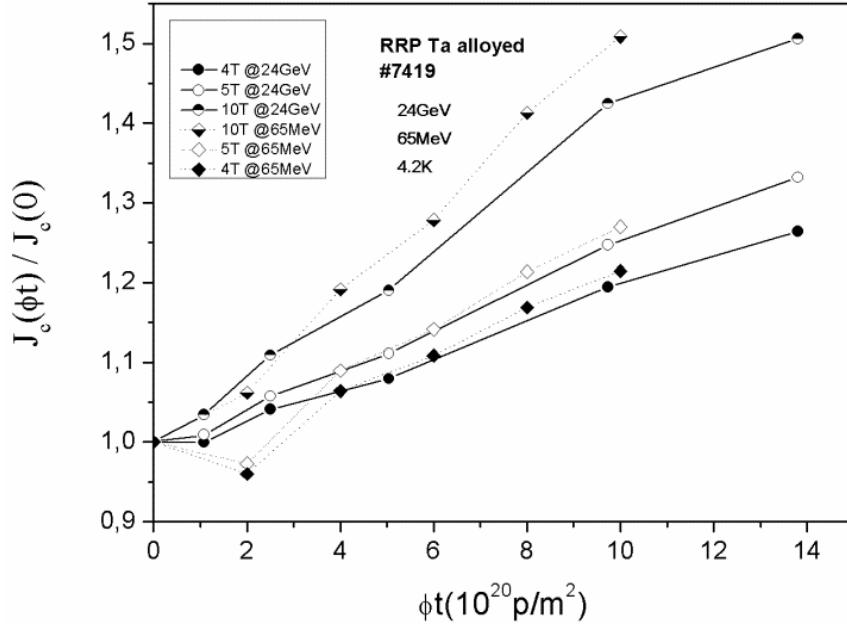


Figure 52 Comparison of the enhancement factor J_c/J_{c0} for the two RRP Ta alloyed wires (#7419) after proton irradiation at 65 MeV and 24 GeV.

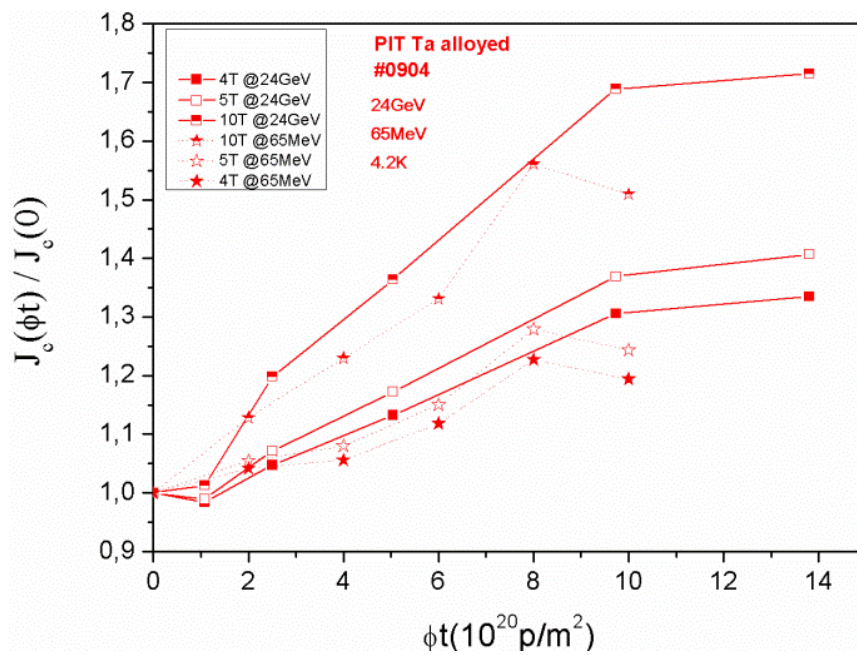


Figure 53 Comparison of the enhancement factor for the two PIT Ta alloyed wires (#0904) after proton irradiation at 65 MeV and 24 GeV.

This comparable enhancement of J_c/J_{c0} at different energies is reasonable if we consider that for both energies, the wires diameters (about 1 mm) are small with respect to the proton penetration depth. For the lower proton energies used in the present work, (65 MeV), the penetration depth determined by FLUKA simulation is 7.3 mm [Table 4](#): the Bragg peak is clearly located outside the wires. In addition, it follows from FLUKA calculation on Nb₃Sn that the displacement per atom (dpa) values for very low thickness (1mm) show only a little difference with proton energy: the dpa is equal to 8×10^{-4} and 1×10^{-3} at 65 MeV ([Figure 54](#)) and 24 GeV ([Figure 55](#)), respectively. As previously mentioned, another argument in favor of a comparable damage at different energies is the similar slope, k_T , of the various T_c vs. Φt curves (see [Table 6](#) and Subsection 4.1.4).

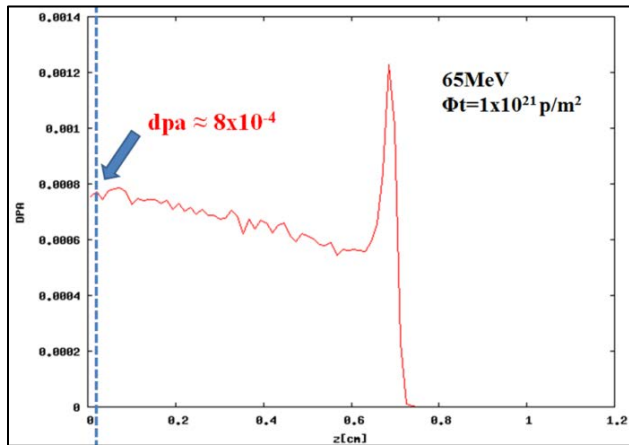


Figure 54 FLUKA simulation for dpa values obtained on Nb₃Sn after proton irradiation at 65 MeV and $1 \times 10^{21} \text{ p/m}^2$. The dashed line indicates the thickness of the wire (1mm).

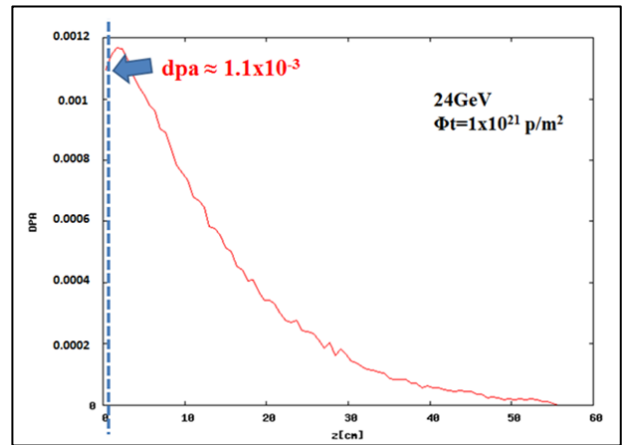


Figure 55 FLUKA simulation for dpa values obtained on Nb₃Sn after proton irradiation at 24 GeV and $1 \times 10^{21} \text{ p/m}^2$. The dashed line indicates the thickness of the wire (1mm).

The higher value of J_c/J_{c0} at high applied field is a consequence of the higher enhancement of J_c at small fields reflecting the enhancement of the pinning force after irradiation. Indeed, taking into account the absolute variation in J_c , $\Delta J_c = J_c - J_{c0}$, in [Figure 56](#), it can be seen that: ΔJ_c (4T) > ΔJ_c (10T) thus J_c/J_{c0} (4T) < J_c/J_{c0} (10T). It follows that the larger enhancements

of J_c/J_{c0} at higher field constitutes an evidence that the increase in J_c is due to the increase of pinning (see the following Subsection for further details).

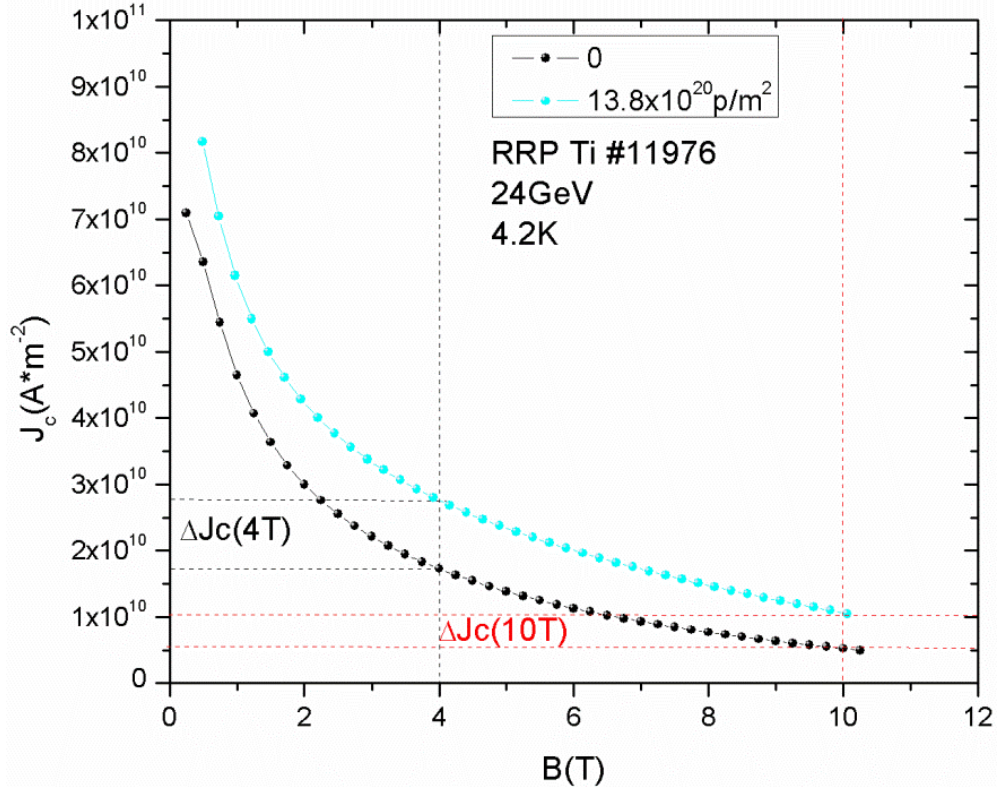


Figure 56 Behavior of the critical current density $J_c(B)$ before and after irradiation for RRP Ti wire (#11976) at 24 GeV and 4.2 K.

4.1.3. Quantitative pinning force analysis

From the available literature data, it follows that high energy irradiation causes a decrease of T_c as well as an increase of both J_c and B_{c2} . The question arises whether the damage mechanism that produces the enhancement of B_{c2} is also responsible for that one of J_c . Several authors, however, stated that the change in B_{c2} is not the main reason for the increase of J_c after high energy irradiation. They showed that the enhancement of J_c after neutron irradiation [100, 101, 102, 99] or protons [150, 62, 104] is in reality dominated by the radiation induced nanosize defect clusters acting as new point pinning centers.

Thus, to study the enhancement of J_c after proton irradiation the behavior of the pinning force with fluence was analyzed.

After irradiation the maximum of the volume pinning force is shifted towards higher values of the applied field, B , as shown in [Figure 57](#) and [Figure 58](#) for RRP wires #7419 and #11976 with Ta and Ti alloyed respectively.

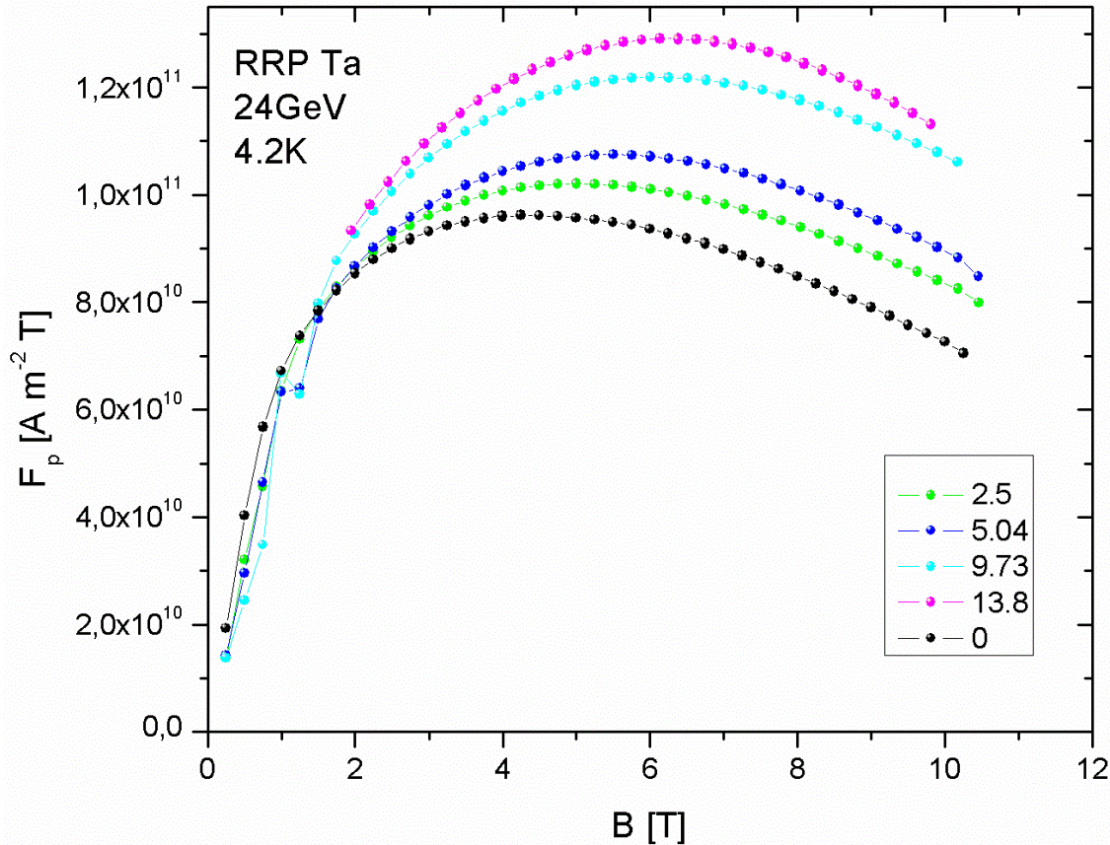


Figure 57 Volume pinning force at 4.2 K as a function of the applied field B for various fluences for RRP Ta alloyed wire #7419 after proton irradiation at 24 GeV.

The analysis of the pinning force before and after proton irradiation performed in this work can be divided in two major parts:

- (I) before irradiation the volume pinning force is analyzed with the usual relation for grain boundaries pinning;
- (II) after irradiation the volume pinning force is analyzed introducing a *two-mechanism* model to take into account the contribution of the radiation induced defects in

addition to that due to grain boundaries. The fitting procedure is performed assuming that the pinning due to grain boundaries does not change after irradiation. This assumption is justified by the fact that the condition at the grain boundaries before irradiation is already non-periodic.

It should be noted here that the analysis of the pinning force for PIT wires required a more careful analysis with respect to that for the RRP wires, as a consequence of the presence of the two different grain morphologies cited above (*two-size model*).

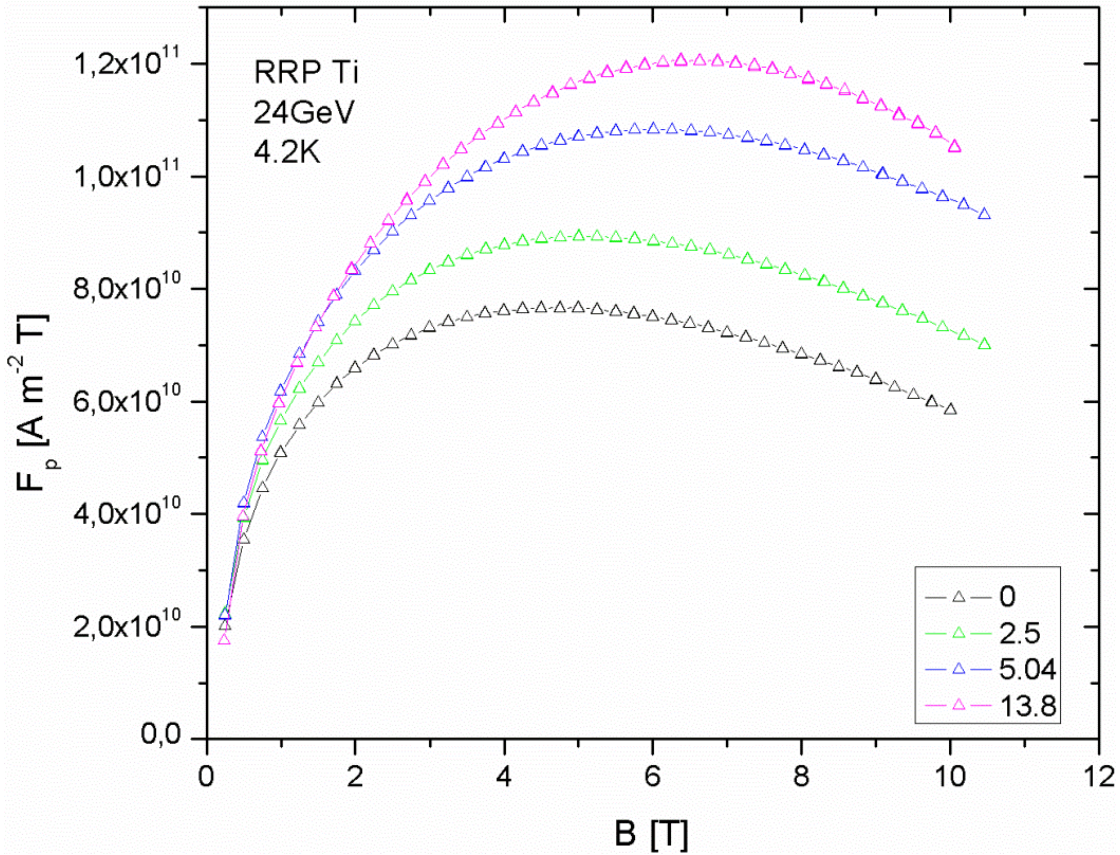


Figure 58 Volume pinning force at 4.2 K as a function of the applied field B and various fluences for RRP Ti alloyed wire #11976 at 24 GeV.

Analysis of the pinning force for RRP wires

Before irradiation the experimental data, $F_p^{exp} = J_c B$, are fitted with the usual scaling law for the volume pinning force:

$$F_p \left(\frac{B}{B_{c20}} \right) = c_{unirr} \left(\frac{B}{B_{c20}} \right)^p \left(1 - \frac{B}{B_{c20}} \right)^q \quad 47$$

where B is the applied field, p and q are fixed to 0.5 and 2 respectively (grain boundary pinning [111]) and c_{unirr} and B_{c20} are taken as fitting parameters. The initial values for the upper critical field, B_{c20} , were determined at all temperatures based on the data sets obtained at 4.2, 6, 8, 10, 12 and 14 K and the results at 4.2 K are reported in [Table 5](#).

After irradiation the volume pinning force is analyzed with a *two-mechanism* model which was developed starting from the ideas developed in the past by K  pfer [63], by Maier and Seibt [128], which were recently quantified by Baumgartner [99] who introduced the scaling law parameters in these models.

In our model, we have assumed that the pinning force due to grain boundaries doesn't change after irradiation. This was performed by replacing the only prefactor introduced in the model of Baumgartner by two different prefactors: one for the contribution of grain boundary pinning and the second one for the contribution of point pinning.

The experimental data have thus been fitted for each fluence using the equation:

$$F_p \left(\frac{B}{B_{c2}} \right) = c_{unirr} \left(\frac{B}{B_{c2}} \right)^{p_1} \left(1 - \frac{B}{B_{c2}} \right)^{q_1} + c_{irr} \left(\frac{B}{B_{c2}} \right)^{p_2} \left(1 - \frac{B}{B_{c2}} \right)^{q_2} \quad 48$$

where B is the applied field, p_1 and q_1 are fixed to 0.5 and 2 (grain boundary pinning [111]) and p_2 and q_2 are fixed to 1 and 2 (point pinning [111]) respectively.

For the pre-factor c_{unirr} , the same value was chosen as before irradiation, introducing in this way the assumption that the grain boundary pinning does not change after irradiation, while B_{c2} and c_{irr} are the fitting parameters. Since this condition was not included in the model of Baumgartner et al. [99], the following results on the defects cluster contribution to the total pinning force after irradiation (described by the β factors, see below) cannot be directly compared.

The results of these fitting procedures are shown in [Figure 59](#) and [Figure 60](#).

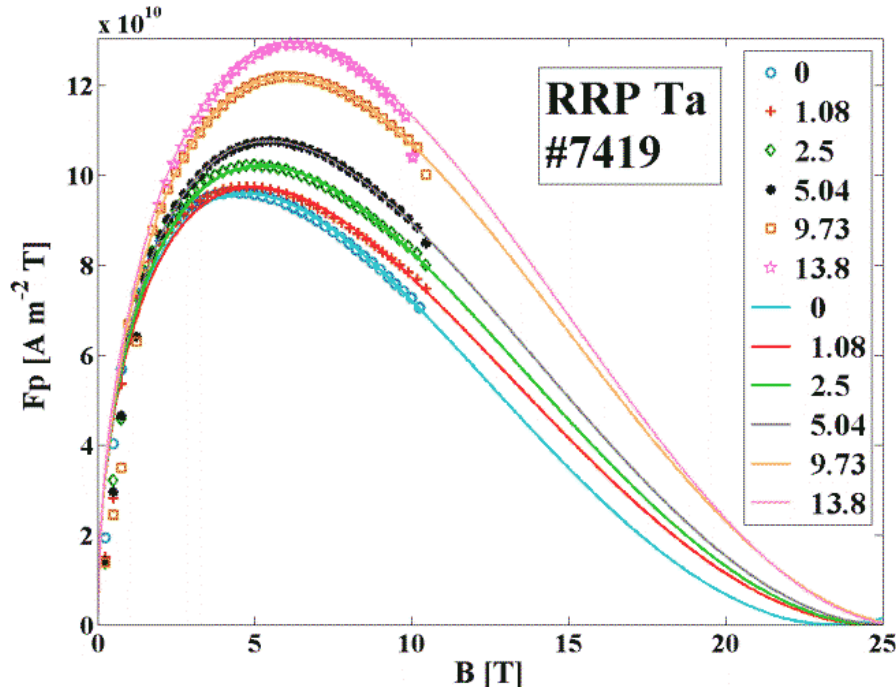


Figure 59 Fitting of the pinning force at 4.2K before and after proton irradiation at 24GeV for the RRP Ta alloyed wire (#7419). From Spina et al. [150].

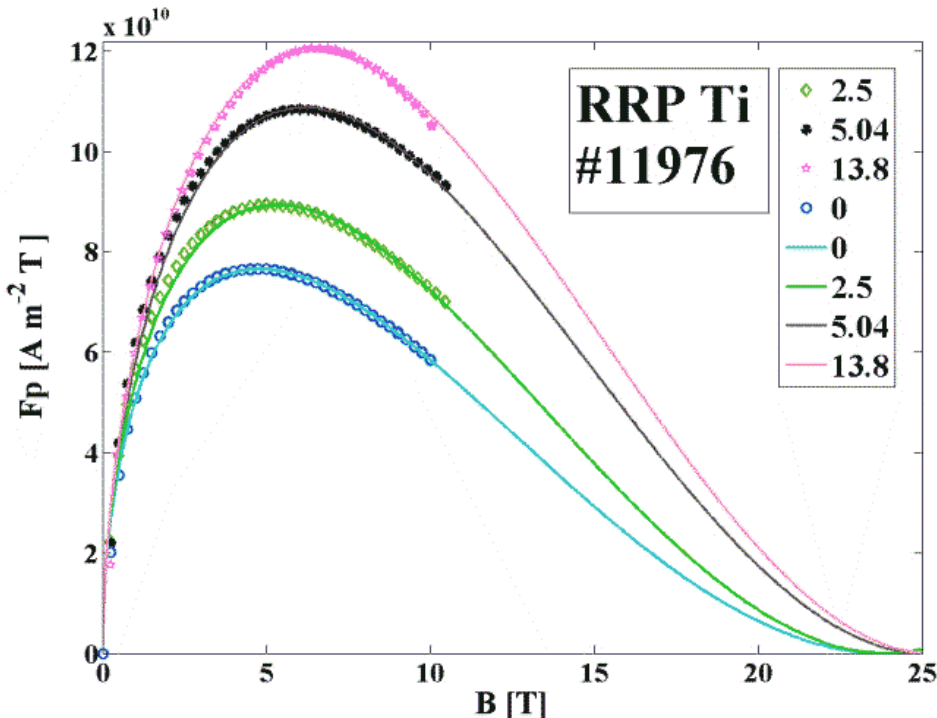


Figure 60 Fitting of the pinning force at 4.2K before and after proton irradiation at 24GeV for RRP Ti alloyed wire (#11976). From Spina et al. [150].

The total pinning force for RRP Ta alloyed wire #7419 after irradiation at 24 GeV and $13.8 \times 10^{20} \text{ p/m}^2$ is shown in [Figure 61](#), as well as the two components:

- Grain boundary pinning: $F_p^{g.b.} = c_{unirr} \left(\frac{B}{B_{c2}} \right)^{p_1} \left(1 - \frac{B}{B_{c2}} \right)^{q_1} = c_{unirr} f_p^{g.b.}$
- Point pinning: $F_p^{p.p.} = c_{irr} \left(\frac{B}{B_{c2}} \right)^{p_2} \left(1 - \frac{B}{B_{c2}} \right)^{q_2} = c_{irr} f_p^{p.p.}$

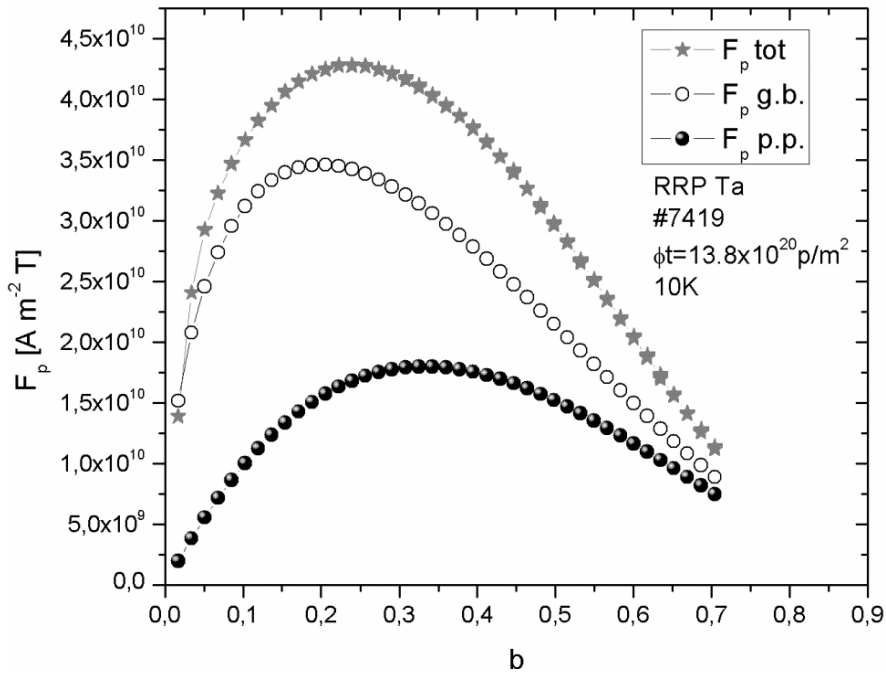


Figure 61 The two contributions to the total pinning force as a function of the reduced field $b=B/B_{c2}$ for the RRP Ta alloyed wire (#7419) after irradiation at 24 GeV and $13.8 \times 10^{20} \text{ p/m}^2$.

The two functions for the grain boundary pinning, $f_p^{g.b.}$ and $f_p^{p.p.}$, as well as the two pre-factors c_{unirr} and c_{irr} are normalized with respect to the maximum values ([Figure 62](#)):

$$|f_p^{g.b.}| = \frac{f_p^{g.b.}}{f_{pmax}^{g.b.}};$$

$$|f_p^{p.p.}| = \frac{f_p^{p.p.}}{f_{pmax}^{p.p.}};$$

$$|c_{unirr}| = c_{unirr} \cdot f_{pmax}^{g.b.};$$

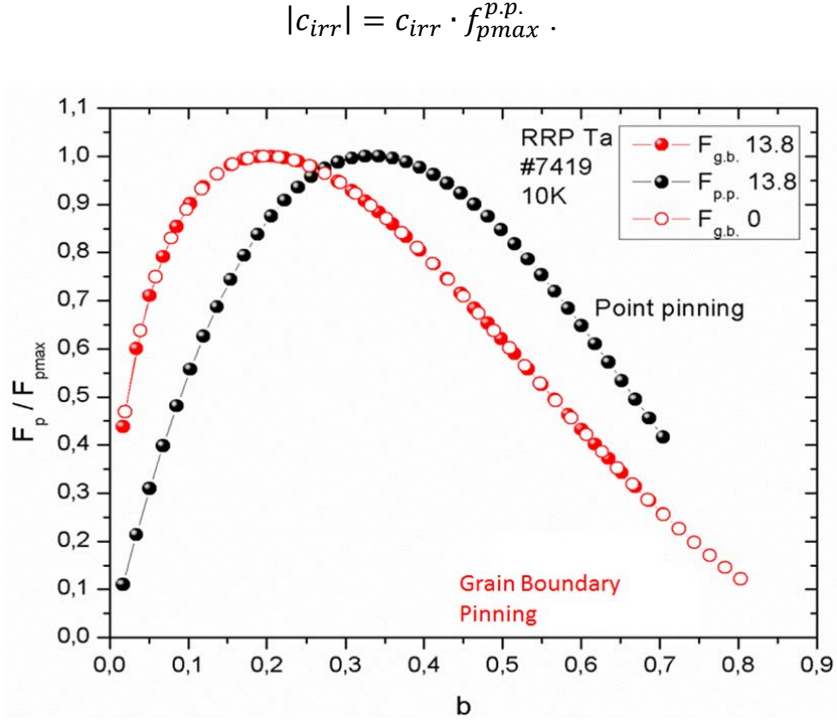


Figure 62 Normalized pinning force vs. reduced field b : the black curve is the point pinning contribution due to radiation induced defects clusters and the full circle red curve is the grain boundaries pinning contribution. For clarity, the curve for the volume pinning force before irradiation is reported also on the same graph (blank circle red curve).

In order to quantify the influence of the two contributions to the volume pinning force after irradiation the equation 48 is rewritten as:

$$|F_p| = k(\alpha|f_p^{g.b.}| + \beta|f_p^{p.p.}|) \quad 49$$

where $k = |c_{unirr}| + |c_{irr}|$ and α and β are defined as $\alpha + \beta = 1$. For the coefficients of the pinning force, one finds:

- Grain boundary coefficient: $\alpha = \frac{|c_{unirr}|}{k}$
- Defects cluster coefficient: $\beta = \frac{|c_{irr}|}{k}$.

The variation of the β coefficient with proton fluence is reported in [Figure 63](#) for the two types of alloyed RRP wires. It illustrates the higher enhancement of J_c/J_{c0} found for irradiated Ti alloyed wire with respect to the Ta alloyed one.

The two $\beta(\phi t)$ functions are fitted with the relation:

$$\beta(\phi t) = 1 - \exp\left(-\left(\frac{\phi t}{(\phi t)^*}\right)^n\right) \quad 50$$

where $(\phi t)^*$ is a characteristical proton fluence and n is the exponent required to adjust the curvature of the function. The fitting parameters values are reported in [Table 7](#).

	$(\phi t)^*[10^{20} p/m^2]$	n
RRP Ta (#7419)	44.95	0.936
RRP Ti (#11976)	56.67	0.4895

Table 7 Fitting parameters of the $\beta(\phi t)$ function for the two types of alloyed RRP wires (Ti and Ta alloying).

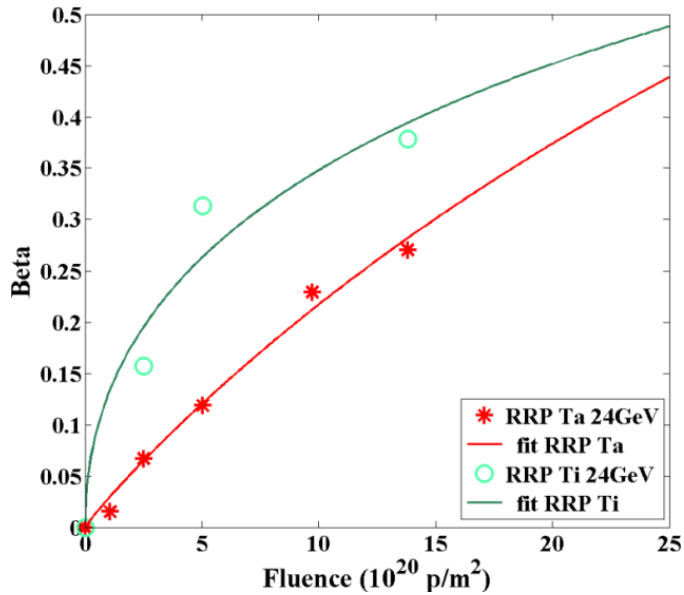


Figure 63 Variation of the coefficient β vs Φt for Ta and Ti alloyed RRP wires after proton irradiation at 24 GeV.

By means of this analysis the variation in B_{c2} in the RRP wires is estimated to be $\sim 5\%$ for Ti and $\sim 10\%$ for Ta alloyed wires, shown in [Figure 64](#). These results lead to an important conclusion: the variation of B_{c2} has little effect on the measured J_c enhancement; indeed, even

assuming an enhancement of B_{c2} by 10 %, for the Ti alloyed wire, the change in J_c would be of the order of 10 % at 10 T, which is much smaller than the measured enhancement of 100 %.

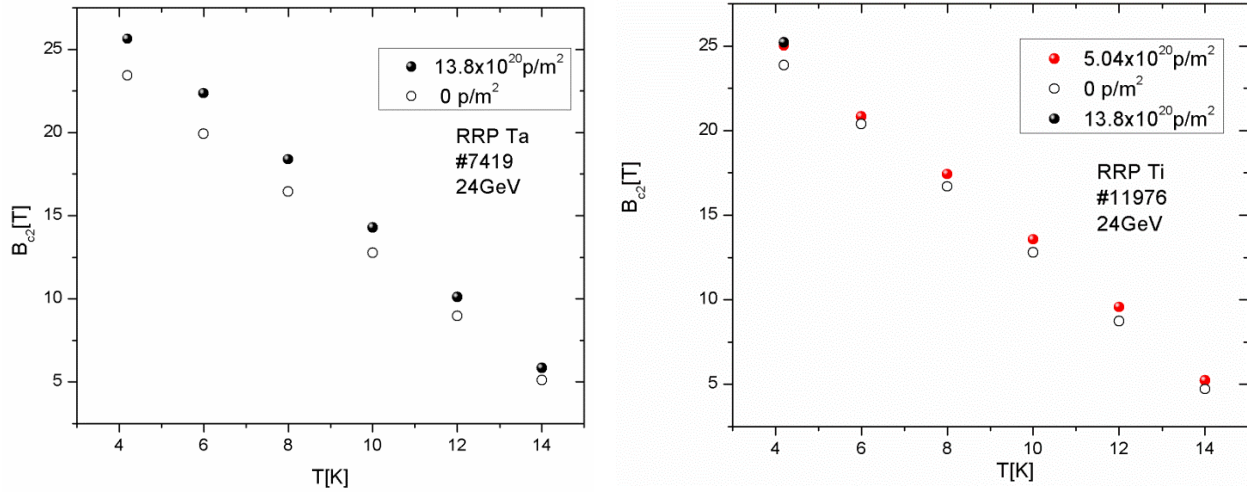


Figure 64 B_{c2} vs. T before and after proton irradiation for RRP Ta (left) and RRP Ti (right) wires.

Finally, it was found that before and after irradiation the normalized pinning force as a function of the reduced field, b , scales with temperature (Figure 65).

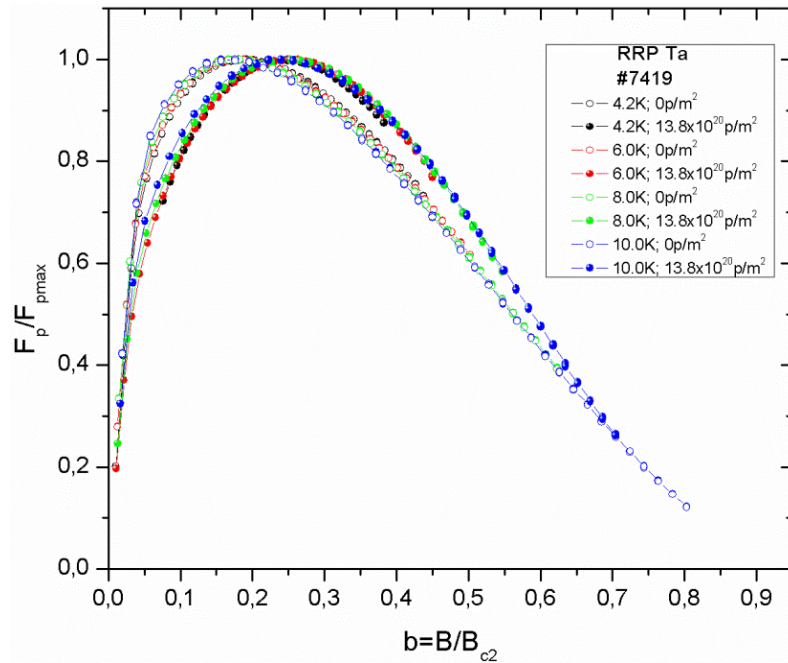


Figure 65 Scaling behavior for a RRP Ta alloyed Nb_3Sn wire before and after proton irradiation at $1.38 \times 10^{21} \text{ p/m}^2$.

Analysis of the pinning force for PIT wires

As observed by means of high field specific heat and magnetization measurements by Senatore and Flükiger [147] there are two A15 phases grain morphologies in PIT wires: a region with small grains of about 200 nm in size characterized by lower T_c and higher B_{c2} values and another region with larger grains (about 1-2 μm in size) characterized by higher T_c and lower B_{c2} values. It is known that large grains do not contribute to the pinning force anyway to take into account their different values in B_{c2} a two-size model was developed to describe the pinning force before irradiation.

Thus, before irradiation the experimental data for PIT wires, $F_p^{exp} = J_c B$, were fitted using the equation:

$$F_p^{g.b.} \left(\frac{B}{B_{c2}} \right) = c_{small} \left(\frac{B}{B_{c2}^{small}} \right)^{p_s} \left(1 - \frac{B}{B_{c2}^{small}} \right)^{q_s} + c_{large} \left(\frac{B}{B_{c2}^{large}} \right)^{p_l} \left(1 - \frac{B}{B_{c2}^{large}} \right)^{q_l} \quad 51$$

where p_s and q_s were fixed to the theoretical values for grain boundaries pinning, i.e. 0.5 and 2 respectively, and p_l and q_l to 0 and 2. In Dew Huges's theory [111] $p = 0$ and $q = 2$ corresponds to a volume pinning force with a core interaction of normal pinning centers that is only expected to operate at high fields as the inter flux lines spacing decreases: in this way the large grains do not contribute to the total pinning force.

To reduce the number of freedom in equation 51 a relation between B_{c2}^{small} and B_{c2}^{large} was set through the following three steps:

- The estimation of $B_{c2}^{small}(0K)$ and of $B_{c2}^{large}(0K)$ are accomplished applying the WHH theory:

$$B_{c2}(0) = 0.693 T_c \left| \frac{dB_{c2}}{dT} \right|_{T_c} \quad 52$$

where T_c values are those measured with AC susceptibility (Figure 49) and the slopes of $B_{c2}(T)$ (i.e. $\left| \frac{dB_{c2}}{dT} \right|_{T_c}$) were estimated as the average value of the results obtained by

Senatore et al. [146]: i.e. $\left| \frac{dB_{c2}}{dT} \right|_{T_c}$ equal to 2.465 and 2.0 for small and large grains respectively.

b. Thus, the temperature dependence of B_{c2}^{small} and B_{c2}^{large} was obtained with the usual relation:

$$B_{c2}(T) = B_{c2}(0) \left(1 - \frac{T}{T_c}\right)^n \quad 53$$

where the factor n was fixed to 1.52.

c. Finally, inserting equation 52 in equation 53, the ratio of $B_{c2}^{small}/B_{c2}^{large}$ was defined.

Thus equation 51 becomes:

$$F_p^{g.b.} \left(\frac{B}{B_{c2}} \right) = c_{small} \left(\frac{B}{nB_{c2}^{large}} \right)^{p_s} \left(1 - \frac{B}{nB_{c2}^{large}} \right)^{q_s} + c_{large} \left(\frac{B}{B_{c2}^{large}} \right)^{p_l} \left(1 - \frac{B}{B_{c2}^{large}} \right)^{q_l} \quad 54$$

where c_{small} , c_{large} and B_{c2}^{large} were used as fitting parameters.

Following this procedure the pinning force before irradiation for PIT wires was analyzed by means of a relation given by the sum of two grain boundaries pinning forces: the “*effective*” grain boundary pinning force (fine grains) and the “*fictitious*” grain boundaries pinning force (coarse grains).

The results found before irradiation with the *two-size* model for the PIT Ta wire are reported in **Table 8**. To test the goodness of the *two-size* model the perfect agreement with the usual scaling law (single mechanism, equation 47) is shown in **Figure 66**.

sample	T[K]	B_{c2}^{small} [T]	B_{c2}^{large} [T]	c_{small}	c_{large}
PIT Ta #0904	4.2K	24.26	21.1	11.52	0.4188
PIT Ta #0904	6K	21.17	18.69	9.373	0.3725
PIT Ta #0904	8K	17.74	16.02	6.678	0.3955
PIT Ta #0904	10K	13.97	13.07	4.378	0.309
PIT Ta #0904	12K	10.13	10.06	2.321	0.2376

Table 8 Fitting parameters obtained with the *two-size* model applied on the PIT (#0904) wires before proton irradiation.

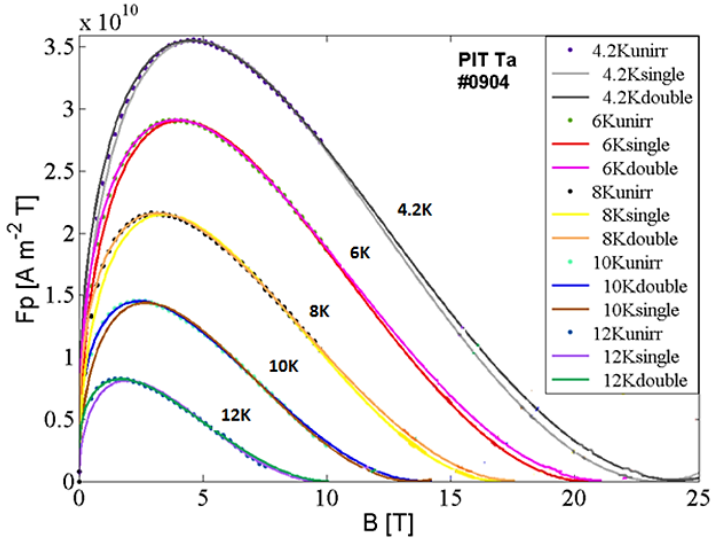


Figure 66 Pinning force before irradiation for PIT Ta alloyed wire (#0904): the *two-size* model is in perfect agreement with the usual pinning force (*single* model).

After irradiation the pinning force was fitted introducing the *two-mechanism* model as previously described for the RRP wires and the results at 4.2 K are shown in Figure 67.

It is interesting to note that with respect to RRP wires (see Figure 59 and Figure 60) the difference between the intensity of the pinning force before irradiation and after irradiation for PIT wire (Figure 67) is markedly higher. The reason behind this stronger increase after irradiation in the PIT wire can be probably assigned to the formation of defect clusters also in the large grains that consequently begin to contribute to the volume pinning force.

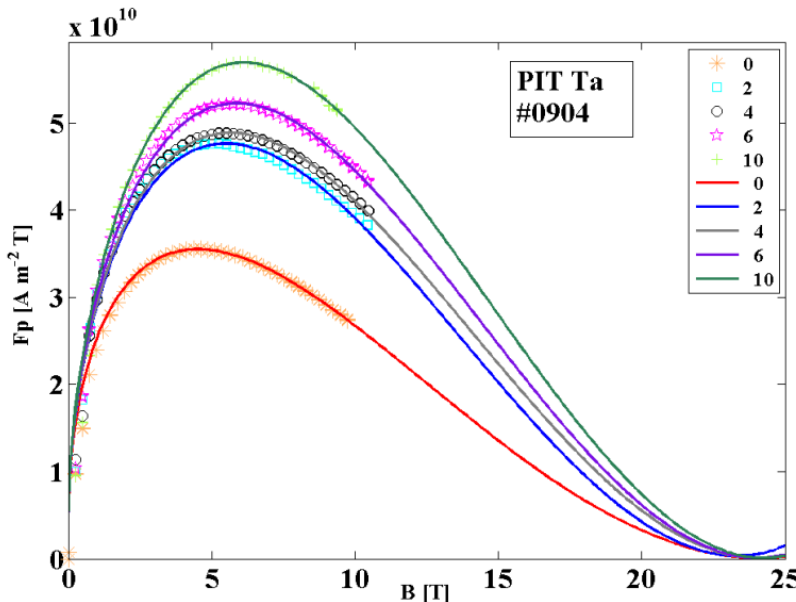


Figure 67 Pinning force at 4.2K for Ta alloyed PIT wire (#0904) after proton irradiation at 65MeV.

The variation of the β coefficient for the point pinning force with the proton fluence for the Ta alloyed PIT wire after proton irradiation at 65 MeV is shown in [Figure 68](#) and the characteristical proton fluence(ϕt)^{*} is equal to $58.7 \times 10^{20} \text{ p/m}^2$ while the exponent n is 0.4421.

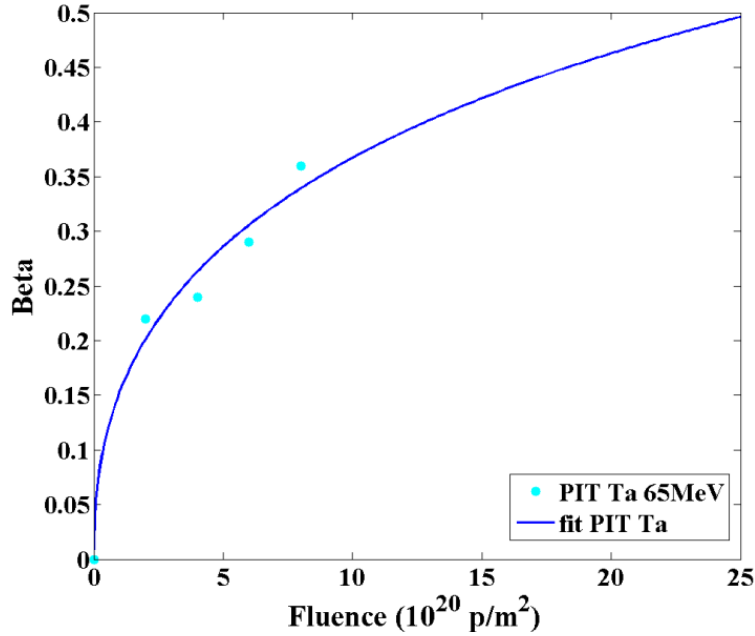


Figure 68 $\beta(\phi t)$ function for PIT Ta alloyed wire at 65MeV.

4.1.4. Comparison between proton and neutron irradiation on Nb_3Sn wires

In order to compare the effects on J_c and T_c at a certain value of proton and/or neutron fluence, the characteristics damage energy (E_D) of each reactor, should be known. Indeed, as described in Section 1.3, E_D is the energy available to generate atomic displacements by elastic collisions and thus the radiation damage effects.

The theoretical determination of E_D is complex and requires the access to specific computer codes. Recently, an experimental method was proposed for estimating the ratio between the E_D values for two different sources, based on the relation between the changes in T_c and the variation in atomic ordering (see Subsection 1.2.3) [152]. Thus, the value of the ratio between

the slope of the $T_c(\phi t)$ curves (*slope ratio*), can be used to compare the effects at various proton and neutron fluences.

As shown in [Table 9](#) the *slope ratio* between the two proton facilities (IRRAD1 and UCL) was found to be ~ 1 while that one between the two proton facilities and the neutron reactor (TRIGA) was ~ 0.1 .

WIRE Type	$T_c(\phi t)$ Slope ratio		
	IRRAD1(24GeV)/UCL(65MeV) (Proton – Proton)	TRIGA(1MeV)/IRRAD1(24GeV) (Neutron – Proton)	TRIGA(1MeV)/UCL(65MeV) (Neutron – Proton)
RRP Ta #7419	0.8 \pm 0.01	0.09 \pm 0.01	0.07 \pm 0.01
PIT Ta SG #0904	1.0 \pm 0.01	0.12 \pm 0.01	0.12 \pm 0.01

Table 9 Slope ratio to compare different sources: TRIGA (neutron reactor) and IRRAD1 and UCL (proton sources)

Two main conclusions follow from this calculation of the radiation damage:

1. Despite the very different energies, the two proton sources (IRRAD1 and UCL) produced the same damage (being the $T_c(\phi t)$ *slope ratio* ~ 1) explaining the similar behavior found in the increase of J_c/J_{c0} at 65 MeV and 24 GeV (see [Figure 52](#) and [Figure 53](#));
2. Being the $T_c(\phi t)$ *slope ratio* TRIGA/UCL and TRIGA/IRRAD1 ~ 0.1 , the same damage is induced at proton fluences being one order of magnitude lower than neutron fluences. Indeed, comparing the results on J_c and T_c obtained after proton (present work) and neutron irradiation (by Baumgartner et al. [99]) on the same Nb₃Sn wires a comparable enhancement of J_c/J_{c0} as well as the same decrease of T_c (see [Figure 69](#)) was observed at neutron fluences more than one order of magnitude higher than proton fluences, reflecting the higher damage induced by protons with respect to neutrons.

After proton irradiation at 65 MeV and 24 GeV up to the maximum fluence of 1.38×10^{21} p/m² from the relation between T_c and S given by Sweedler et al. [79] and starting with the initial value of $S=0.98\pm0.02$ determined by X – ray refinement it follows that after proton irradiation the variation of the Bragg Williams LRO would be below 1%, in agreement with the recent

estimation by Baumgartner *et al.* [124]. This suggests that the same variation ΔS of the long-range atomic order parameter induced by neutron is obtained at proton fluences one order of magnitude smaller.

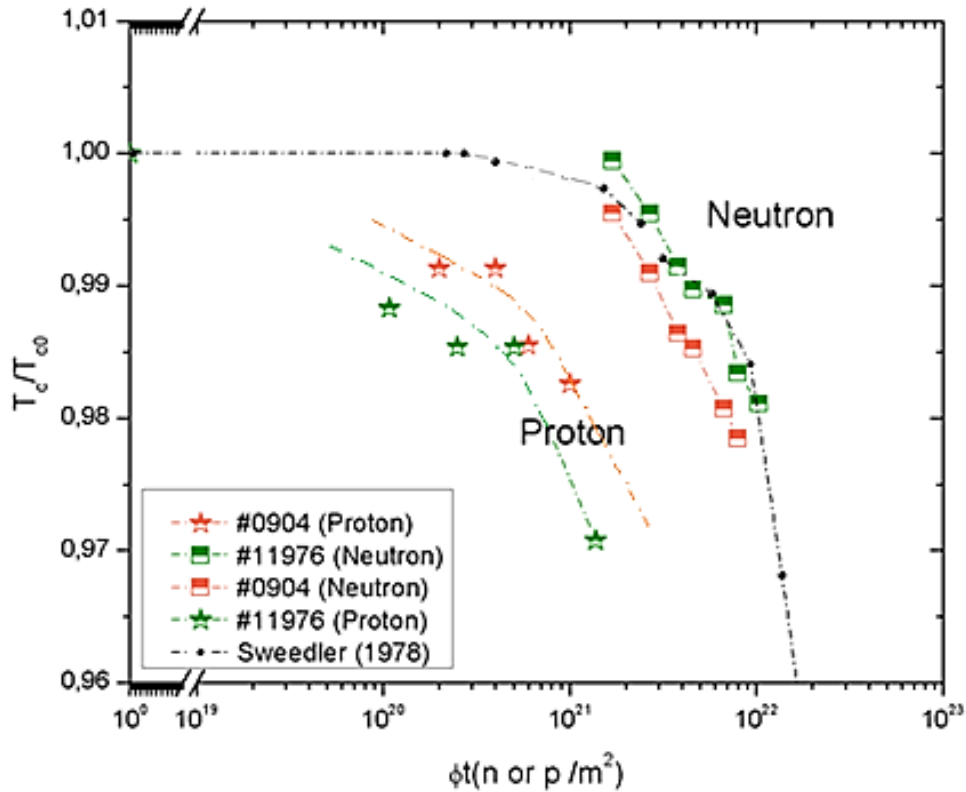


Figure 69 Comparison between the decrease of T_c with fluence after proton (star [149]) and neutron (square [124] and circle [79]) irradiation.

4.2. Results on Nb₃Sn platelets

In this section the results obtained on the Nb₃Sn platelets by means of diffraction and magnetization measurements performed at the University of Geneva and at the Kurchatov Institute will be described. A particular attention will be given to the change in the Bragg Williams LRO and in the crystallographic parameters (lattice constant and microstrain) after proton irradiation at 10 MeV.

4.2.1. The Bragg – Williams LRO parameter

Precise value of the long – range order parameter have been determined in a large number of A15 type compounds, as for example Nb₃Ir, Nb₃Pt [153] or Nb₃Al [154]. The case of Nb₃Sn is particular: due to the small difference between the form factors of Nb and Sn (f_{Nb} and f_{Sn}) which is a consequence of the proximity of Nb and Sn in the periodic system ($\Delta Z = 9$). The relative intensity of the superlattice reflection (110) is quite low, resulting in a ratio I(110)/I(211) as low as 0.14 for perfect ordering. This low ratio in the relative intensity of the superlattice reflections for Nb₃Sn compound increases the uncertainty ΔS . It follows that the determination of a precise order parameter for Nb₃Sn requires not only homogeneous and very well defined samples, but also an excellent X – ray counting statistics, the error reaching ± 0.04 in low quality Nb₃Sn samples. Sweedler et al. [79] reported perfect ordering of S=1 for Nb₃Sn before irradiation (corresponding to the very low electrical resistivity), but gave no details of the diffraction data were given, neither about the line intensities nor about the refinement procedure. Other authors [156][155, 156] studying irradiation effects on Nb₃Sn assumed perfect ordering, too, based on the data of Sweedler et al. [79].

The present work thus constitutes the first complete Rietveld refinement of the Bragg – Williams long – range order parameter in Nb₃Sn by means of X – ray diffractometry data.

Rietveld Refinement (Full Prof software) before proton irradiation

As previously reported (Subsection 2.2.4), the Bragg-Williams long range order parameter before irradiation (Nb₃Sn sample #4) $S = S_a = S_b = 0,98 \pm 0,02$ was estimated through the Rietveld Refinement procedure (described in Section 3.3) and it is an average values obtained after a dozen of X – ray measurements performed on the same sample.

This value corresponds to a state of atomic ordering very close to perfect ordering: S_a is associated to an occupation factor of Nb in 6c sites of $r_a = 0,997 \pm 0,003$ and S_b is associated to an occupation factor of Sn in 2a sites of $r_b = 0,991 \pm 0,003$.

This result justifies *a posteriori* the value assumed by Sweedler et al. [79]: S=1 on Nb₃Sn before irradiation.

From a least-square fit, the lattice constant, a , and the isotropic temperature factor, B_{iso} , were found to be $5,291 \pm 0,003$ Å and $0,407 \pm 0,003$ Å respectively. These experimental values are in good agreement with the theoretical one: $B_{iso}^{th} = 0.4$ Å estimated in Subsection 1.2.2 and $a=5,289 \pm 0.01$ Å found by Devantay et al. [16] for Nb₃Sn at the stoichiometric composition (25 at.%Sn).

The agreement factors for the Rietveld refinement performed in the present work are reported in Table 10. The excellent values for these factors ensure the goodness of the refinement procedure and thus of the results.

Agreement Factor	Value	Expected limit
R _{exp}	6.46	<15
GofF	1.59	<2
χ^2	2.5	~1

Table 10 Agreement Factors. The slightly higher value for the χ^2 has to be assigned to the preferential orientation that was not taken into account during the refinement procedure due to the high number of parameters in the model (see Subsection 3.3.1).

In order to exclude the influence of texture effects, the Bragg Williams LRO parameter has also been estimated with the simple method described in Subsection 3.3.1 (See “Empirical method to extrapolate the S value”). By means of such extrapolation, averaging on the peaks (110), (211), (222), (320), (321), (400), (332) and (440), it was found that $S^{empirical} = 0.979$, i.e. it is in perfect agreement with the refined value.

Synchrotron analysis after proton irradiation

To investigate the effects at the Bragg peak (see Subsection 3.1.2) on the microscopic structure and thus, to get some information on the variation of the lattice constant, of the microstrain and

of the Bragg Williams LRO parameter, a set of three pairs of Nb₃Sn platelets have been irradiated with 10 MeV protons at the Kurchatov's cyclotron U-150 at different fluences:

- Platelets with thicknesses of 0.18 (steady loss) and 0.12 mm (Bragg peak) irradiated at a fluence of 3×10^{20} p/m²;
- Platelets with thicknesses of 0.20 (steady loss) and 0.18 mm (Bragg peak) irradiated at a fluence of 3×10^{21} p/m²;
- Platelets with thicknesses of 0.20 (steady loss) and 0.18 mm (Bragg peak) irradiated at a fluence of 1×10^{22} p/m²;
- Pristine platelet with thickness of 0.18 mm has been measured for consistency of the results (see later on).

In the following the sample in the steady loss and in the Bragg peak regions will be indicated as #1 and #2 respectively. The description of the general arrangement of the Nb₃Sn platelets with respect to the proton beam has already described in Subsection 3.1.2. Due to the lack of the important information about the distribution of the energy deposition inside the two samples (-dE/dx) from which it would have been possible to estimate the exact position of the Bragg peak inside samples #2 we tried to figure out where the Bragg peak should be located taking into account from FLUKA simulation the dpa vs the proton penetration depth and the thickness of the two samples sent to the Kurchatov Institute. Thus, in [Figure 70](#) the estimated position of the two platelets (#1 and #2) with respect to the stopping power at 10 MeV for each proton fluence is shown.

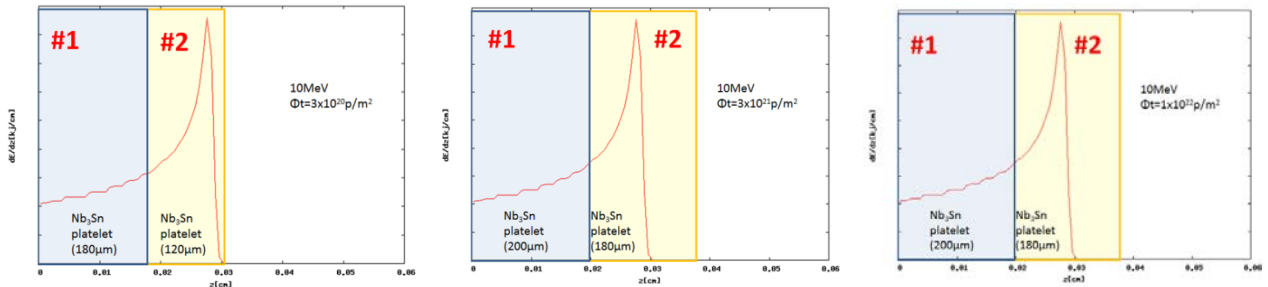


Figure 70 Description of the approximate position of the two platelets (#1 and #2) with respect to the stopping power calculated by means of FLUKA simulation for each proton fluence.

Due to safety prescription due to radioactivity, it was not possible to perform X-ray diffraction measurements at the University of Geneva: the irradiated samples were thus studied at the Kurchatov Institute by means of synchrotron X-ray powder diffraction (XRPD) and resonant diffraction (REXD) by Y. Zubavichus. As will be explained hereafter, resonant diffraction measurements (also known as Anomalous X-ray scattering) have the advantage to overcome the problems due to the texture effects in the determination of the Bragg Williams LRO parameter.

According to the refinement procedure performed by Y. Zubavichus, it was found that the lattice constants of the Nb₃Sn phase in irradiated platelets increase up to 5.324 Å at $1 \times 10^{22} \text{ p/m}^2$. The peak broadening at very high fluences is mainly attributed to microstrain effects. The enhancement of the lattice constants and microstrains for both the steady loss and Bragg peak regions are reported in [Figure 71](#) as a function of the fluence.

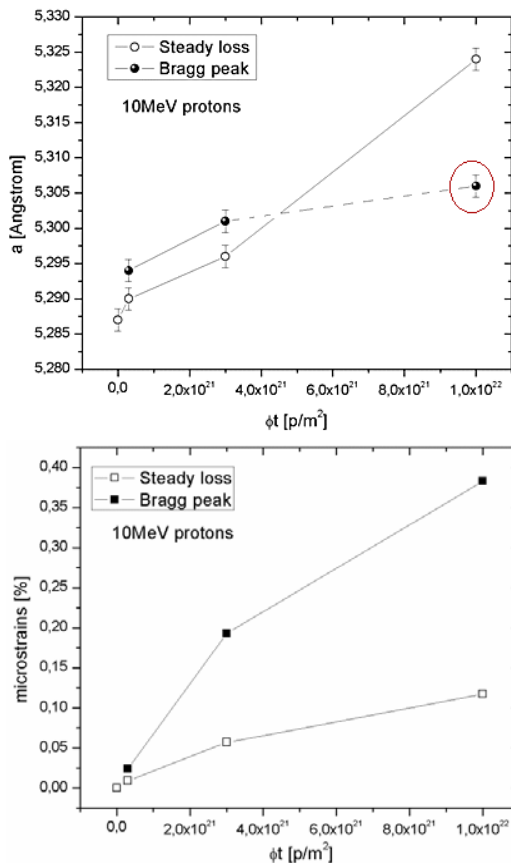


Figure 71 Increase of the lattice constant (top) and microstrain (bottom) with fluence for both the steady loss and the Bragg peak regions. It should be noted that at $1 \times 10^{22} \text{ p/m}^2$ the value of the lattice constant for the sample in the Bragg peak region is lower than expected due to the presence of more than one A15 phases (explanation: see text).

For the higher fluences, i.e. 3×10^{21} p/m² and 1×10^{22} p/m², the Bragg peak platelets (samples #2) are characterized by considerably larger microstrains. The inversion of this tendency for the lattice constant after 1×10^{22} p/m² (a higher value for the platelets #1 with respect to #2) is explained taking into account the split of the peak (220) of sample #2, shown in [Figure 72](#).

Indeed the available sample thickness (0.18 mm) is larger than the thickness of the total damage around the Bragg peak (calculated width: 0.05 to 0.1 mm, see [Figure 16](#) in Chapter 1) thus the “double” peak at high angles in sample #2 reflects the co-existence of two A15 phases with different degrees of order: the first one corresponds to a higher lattice constant at the Bragg peak (about 70% of the entire peak), the second one corresponds to the lattice constant in the region behind the Bragg peak (about 30%) being almost unchanged with respect to the state prior to irradiation reflecting the fact that after the Bragg peak there is no radiation damage.

It should be noticed that the increase of the microstrain induced in the platelets #1 (steady loss) is only 0.1% at the maximum fluence that is one order of magnitude higher than the highest fluence used for our proton irradiations on Nb₃Sn wires (1.38×10^{21} p/m²). At these fluences, as was explained in “Changes in T_c after irradiation” in Subsection 1.3.3, the effect of microstrains on the decrease of the critical temperature is negligible.

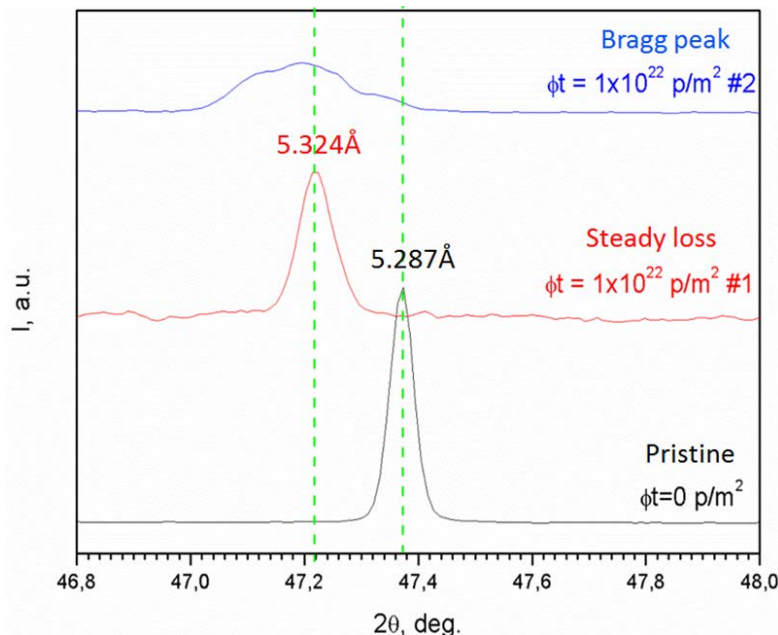


Figure 72 Comparison of the (220) peak between the pristine and the two platelets at the maximum fluence (1×10^{22} p/m²). For sample #2 the irregular shape of the peak reflects the occurrence of two regions inside this sample only one of which being damaged.

The decrease of the Bragg Williams LRO order parameter, S, with fluence was estimated by Zubavichus studying the changes in the relative intensity of the (110) peak, normalized to the (210) peak, in analogy to the empirical method developed by the author (see Subsection 3.3.1). As shown in Figure 73, the order parameter decrease with fluence and such decrease is stronger for the platelets #2 than for #1: as expected, the Bragg peak induced a higher disorder than the steady loss.

However the values of S found by means of X-ray powder diffraction (XRPD) are affected by a large uncertainty because the superlattice line (110) is very sensitivity to texture.

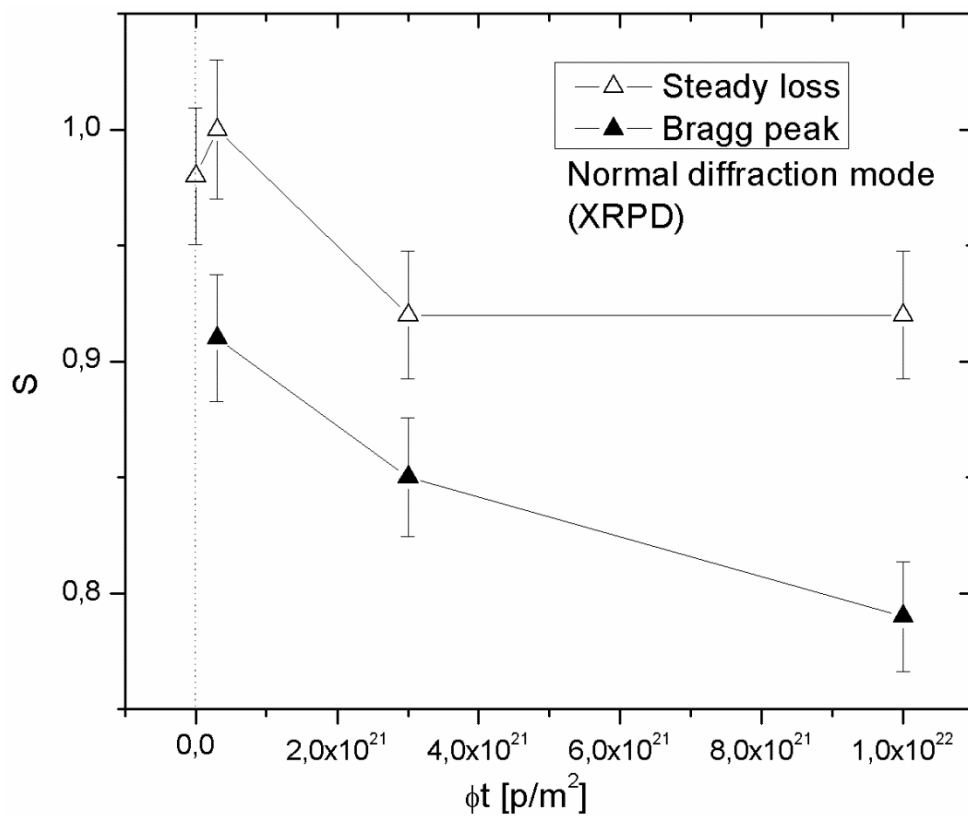


Figure 73 Decrease of the Bragg Williams LRO parameter, S, with fluence as estimated from the relative intensity of the (110) peak. The experimental pattern was measured by means of X-ray synchrotron diffraction (XRPD), i.e. normal diffraction mode. In the Bragg peak region a stronger variation of S is shown.

Indeed, according to crystallographic simulations performed by Y. Zubavichus, for a fully ordered stoichiometric Nb₃Sn, the relative intensity of the (110) peak with respect to the (210) peak is expected to be ~ 0.04 while the experimental value has been found in a larger range, i.e. between 0.04 and 0.06. This fluctuation in the experimental intensity with respect to the theoretical one reveals that there are some additional factors affecting line intensities, such as preferred orientation or local inhomogeneities, which have not been taken into account leading to incorrect S values.

To improve the determination of S, a set of additional measurements near the absorption edge of Niobium, i.e. in the resonant diffraction mode, have been performed. By means of these measurements, the intensity of the (110) peak is increased nearly 3 times, allowing a better estimation of the order parameter.

The changes in the (110) intensity with fluence are shown in [Figure 74](#) and the resulting S value in [Figure 75](#).

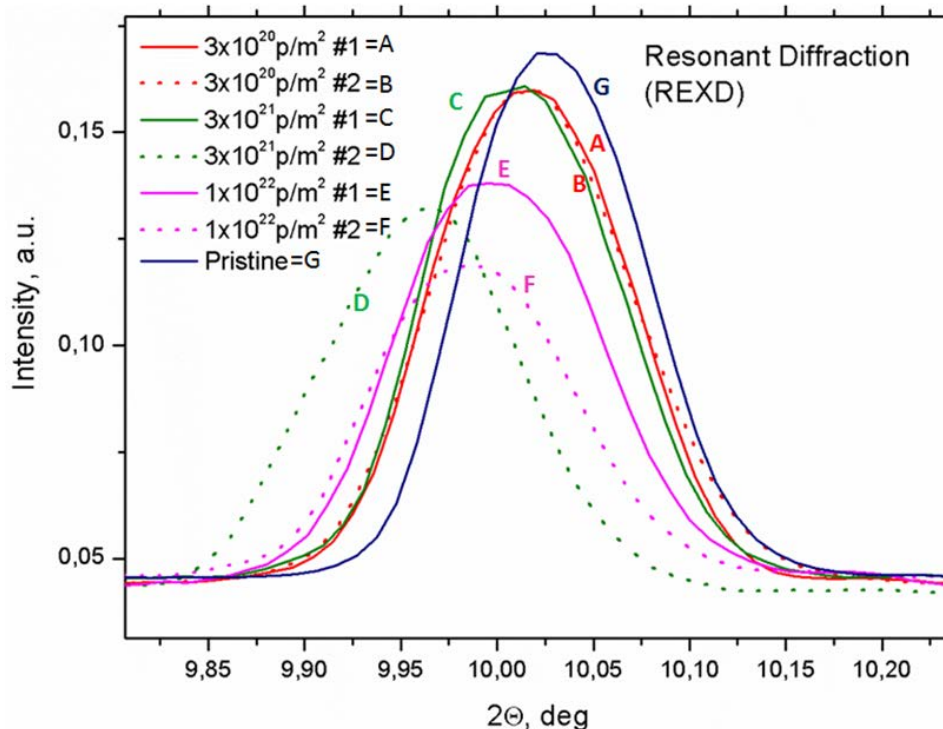


Figure 74 Variation of the (110) intensity with fluence acquired in the resonant mode for the Bragg peak (dashed lines, samples #2) and the steady loss regions (continuous lines, samples #1).

In the resonant diffraction mode, the pristine sample is characterized by the maximum relative intensity of the (110) line, whereas the respective intensities for the proton-irradiated samples are systematically lower especially for those in the Bragg peak region.

The decrease of the order parameters S up to the maximum fluence of 1×10^{22} p/m² for the platelets in the steady loss and at the Bragg peak is 3.1% and 14.2%, respectively.

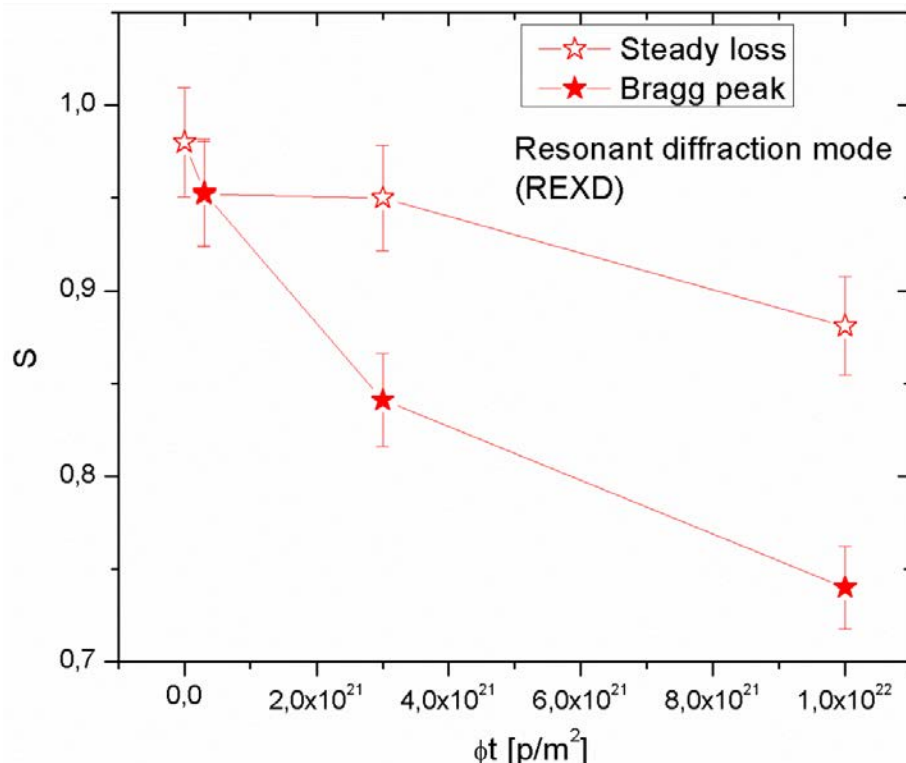


Figure 75 Decrease of the Bragg Williams LRO parameter, S, with fluence as estimated from the relative intensity of the (110) peak. The experimental pattern was measured by means of resonant diffraction (REXD) that is texture independent allowing a better estimation of S. In the Bragg peak region a stronger variation of S is shown.

4.2.2. Decrease of T_c at the Bragg peak

VSM magnetization measurements with a Quantum Design PPMS system have been performed at the Kurchatov Institute on the irradiated Nb₃Sn platelets (#1 and #2) to study the decrease of the critical temperature after proton irradiation at 10 MeV up to 3×10^{21} p/m².

As shown in Figure 76 the T_c degradation is stronger for the platelets at the Bragg peak than for those that are located in the steady loss region being the percentage variation 26.26% and 13.41% respectively.

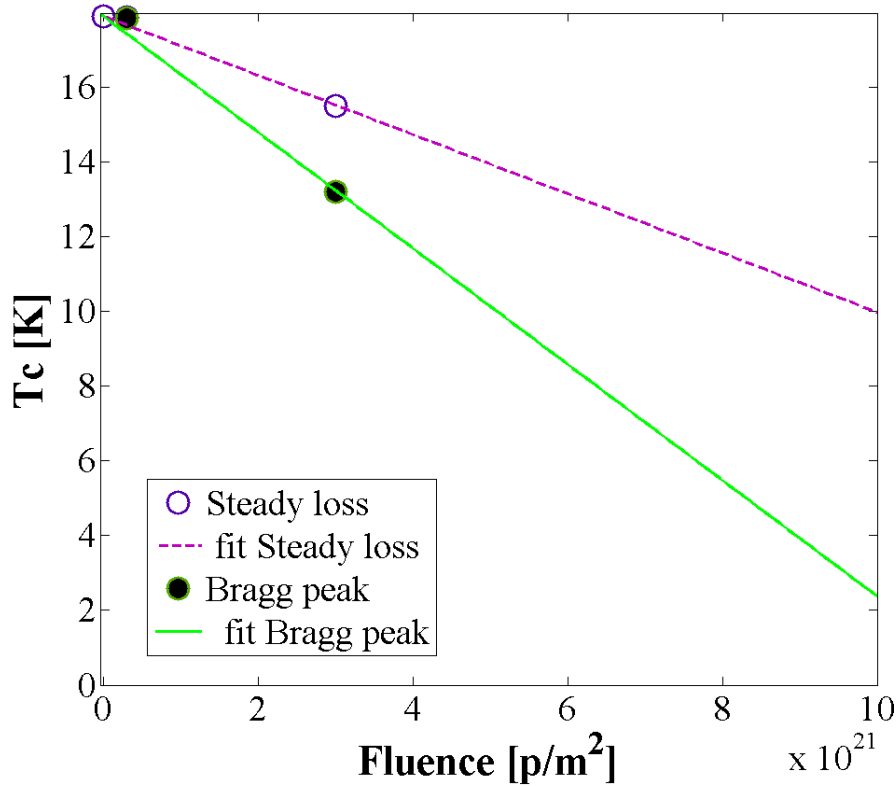


Figure 76 Decrease of the critical temperature after 10 MeV proton irradiation after $1 \times 10^{20} \text{ p/m}^2$ and $3 \times 10^{21} \text{ p/m}^2$.

In analogy to the analysis performed on the proton irradiated Nb₃Sn wires (see Subsection 4.1.1), the linear decrease of T_c found on the irradiated platelets was fitted by the relation $T_c = T_{c0} - k_T \Phi t$, where T_{c0} is the critical temperature in the unirradiated platelet (i.e. 17.9K) and k_T is the slope $dT_c/d\Phi t$ given in Table 11.

Two conclusions follow from this analysis: first of all the slope k_T is larger for the platelets #2 reflecting the higher damage induced into the A15 structure by the Bragg peak; second, the k_T

value for the steady loss curve is almost the same of that one found for the Nb₃Sn wires (see Table 6).

Platelet	$k_T [10^{-20} \text{ K p}^{-1} \text{m}^2]$
#1 (Steady loss)	0.07±0.01
#2 (Bragg peak)	0.15±0.01

Table 11 Fit parameters for the linear decrease of T_c with fluence for the Nb₃Sn platelets (#1 and #2) irradiated at 10 MeV up to the fluence of $3 \times 10^{21} \text{ p/m}^2$.

As previously discussed the small increase of the microstrain cannot be responsible for the decrease of T_c . It follows that the changes in T_c are caused by the homogeneous decrease of S , as already explained by several authors (see discussion in Subsection 1.3.3.).

The exponential behavior of the T_c vs the Bragg Williams LRO parameter described by the equation 29 in Chapter 1 is shown in Figure 77.

Comparing the present results with those obtained by Sweedler et al. [79] after neutron irradiations at 1 MeV up to $5 \times 10^{23} \text{ n/m}^2$ it follows that all the data obtained on the Nb₃Sn platelets in the steady loss region fall on the same curve regardless of the type of particles. The results of the platelets #2 deviate from the exponential behavior of the $T_c/T_{c0}(S/S_0)$ curve, which is due to the inhomogeneity in the atomic ordering induced in the Bragg peak region, giving rise to a distribution of T_c values: the lower values of T_c cannot be detected by means of magnetization measurements due to shielding effects.

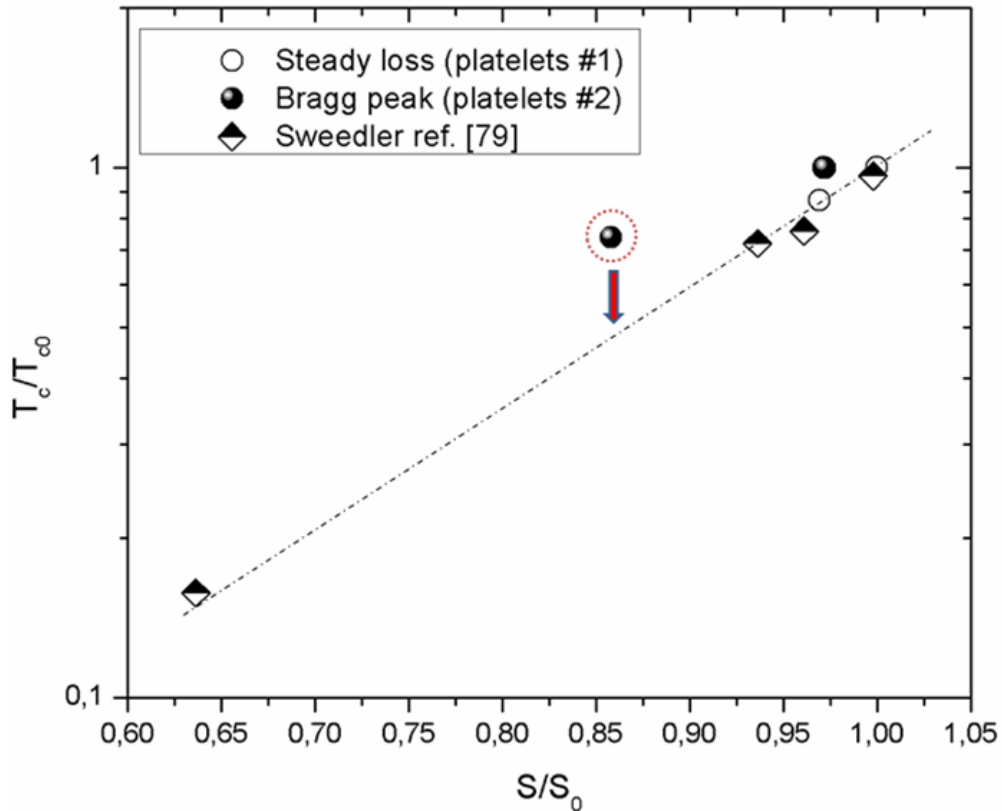


Figure 77 Relationship between the ratio T_c/T_{c0} and S/S_0 after proton irradiation at 10 MeV up to the fluence of $3 \times 10^{21} \text{ p/m}^2$. Comparisons of the results obtained by Sweedler et al. [79] after neutron irradiation at 1 MeV up to $5 \times 10^{23} \text{ n/m}^2$ are shown. The arrow indicates that due to the inhomogeneity induced by the Bragg peak the measured value of T_c for the platelet #2 is higher than the expected ones.

CHAPTER 5: CALCULATION OF THE DPA NUMBER

In Subsection 1.3.2 the main differences between proton and neutron irradiations were described in details.

Protons are usually generated in accelerators and emerge in monoenergetic beams with very narrow energy widths while the neutron energy spectrum in a reactor extends over several orders of magnitude in energy.

In Section 4.1.4 an experimental method ($T_c(\phi t)$ slope ratio), previously introduced by Flükiger et al. [152], was used to compare the damage induced by protons and neutrons on Nb₃Sn wires; by means of this method it was found that the same effects on J_c and T_c can be observed at proton fluences one order of magnitude lower.

In this chapter the comparison between the radiation effects induced by charged and neutron particles on the critical properties of Nb₃Sn wires under investigation will be performed by discussing the number of displacements per atom (dpa).

The goals of this last part of the work are:

1. The replacement of the fluences by the dpa number resulting from calculations by means of FLUKA simulation. As will be shown, dpa is a very convenient quantity for a direct comparison of the damage induced by different projectiles (protons and neutrons) at various energies.
2. Formulation of a relationship between the statistical dpa values and the physical changes, in case of T_c being monitored by the Bragg-Williams LRO parameter.

5.1. Definition and calculation of dpa with FLUKA code

The displacement per atom (dpa) is a statistical quantity that includes information about the amount of radiation damage in irradiated materials and is commonly used to quantify the damage produced under different irradiation environments (i.e. different projectiles, energies and fluences).

As reported by Fasso et al. [157], in FLUKA the dpa quantity is defined as:

$$dpa = \frac{A}{VN_A\rho} N_F \quad 55$$

where ρ is the density in units of g/cm^3 , A is the mass number, V is the volume, N_A is the Avogadro number and N_F is a Frenkel pair. For example, 3 dpa means each atom in the material has been displaced from its site within the structural lattice of the material an average of 3 times.

A Frenkel pair forms when an atom or ion leaves its place in the lattice (leaving a vacancy) and lodges nearby in the crystal (becoming an interstitial). N_F is defined in FLUKA following the NRT theory (see Subsection 1.3.1) as:

$$N_{NRT} \equiv N_F = k \frac{\xi(T)T}{2E_d} \quad 56$$

where k is the displacement efficiency and the product $\xi(T)T$ is related to NIEL (Non Ionizing Energy Losses). The value of the Lindhard partition function $\xi(T)$ gives the fraction of the total stopping power $S(T)$ that goes into NIEL:

$$\xi(T) = \frac{S_n(E, E_{th})}{S(T)} \quad 57$$

where $S_n(E, E_{th})$ is the *restricted nuclear stopping power* for recoil energy T above the damage threshold, E_{th} (i.e. the displacement energy E_d in subsection 1.3.1). It should be noticed that the reason behind the use of a restricted nuclear stopping power in FLUKA implementation is due to the fact that the Lindhard approximation using the unrestricted NIEL includes all the energy losses, i.e. also those below E_{th} , with the consequence to overestimate the number of dpa.

The displacement efficiency k (i.e. the parameter that reflects the recombination of pairs) can be considered independent from energy and equal to 0.8 only in the range of $T \leq 1 - 2 \text{ keV}$ while

at higher energies, the development of collision cascades results in defect migration and recombination of Frenkel pairs due to overlapping of different branches of a cascade which translates into decay of $k(T)$. It follows that at high energy, a *modified displacement efficiency* $k(T)$ based on molecular dynamics (MD) is introduced into the FLUKA code.

In FLUKA the only parameter requested to the user is the damage threshold E_{th} for all material in the simulation. For Nb_3Sn such threshold was fixed to 30 eV. This value was chosen as an average among several literature values [158, 159]. The evaluation of dpa is performed as follow:

- For charged particles: above the transport threshold E_{th} the dpa estimation is based on the *restricted nuclear stopping power* weighted with the *modified displacement efficiency* $k(T)$ that takes into account the recombination effects; below the transport threshold E_{th} the integrated nuclear stopping power obtained by the Lindhard partition function is used. Recoils and secondary charged particles are explicitly produced if their energy lies above transport threshold (i.e. they become a projectile), otherwise they are treated as below threshold.
- For neutrons: at high energy ($> 20 \text{ MeV}$) the dpa are obtained as for charged particles; at low energy ($\leq 20 \text{ MeV}$) dpa estimation are based on (un)restricted NIEL as provided by NJOY (i.e. multi-group approach) [160].

5.2. Evaluation of dpa at the Bragg Peak

In Subsection 1.3.2 it was explained that the formation of the Bragg peak in the energy loss curve for charged particle is due to the relationship between the total stopping power and the scattering cross section (equation 26): as the energy of the charged particle decreases the scattering cross section increase finally leads to the formation of a peak in the energy deposition. In addition it was observed that the nuclear stopping power becomes important at low ion energy (see [Figure 14](#) in Chapter 1) thus at the end of the stopping curve.

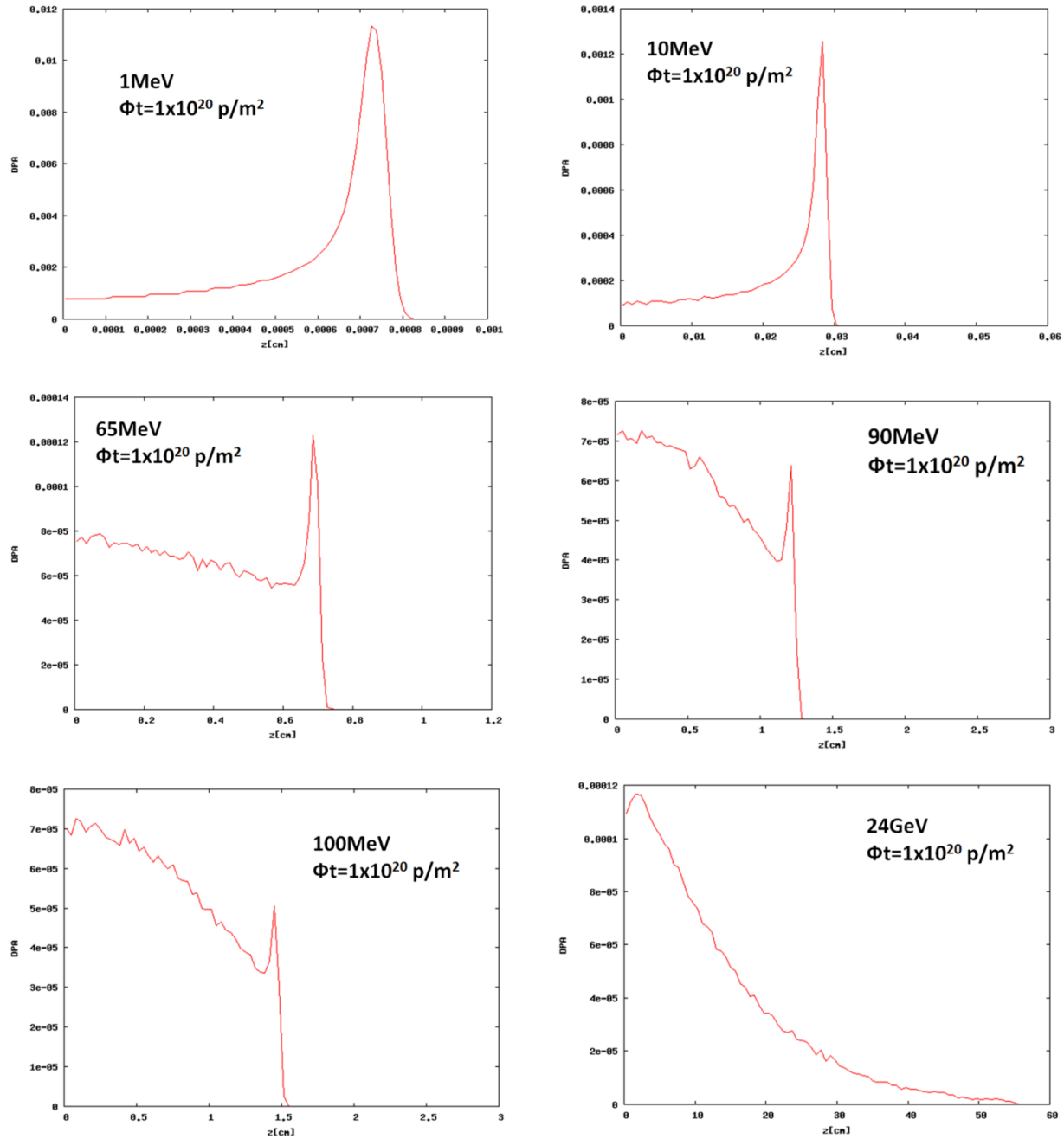


Figure 78 Evolution of the Bragg peak with proton energy.

For investigating the damage effects it is more important to take into account the number of dpa along the slowing down of the charge particle (i.e. along the penetration depth). In Figure 78 the calculated dpa values with the proton penetration depth for different energies are shown. At the lower proton energies (1, 10 and 65 MeV in Figure 78) the higher number of dpa is produced by

the primary particles occurring at the location of the Bragg peak; at high proton energies (90 and 100 MeV and 24 GeV), the dpa are mainly produced by the secondary particles, the dpa value is thus higher in the steady energy loss region. In [Figure 79](#) the dpa values at the Bragg peak (dpa_1) and in the steady energy loss region (dpa_2) with the proton energy are shown while in [Figure 80](#) the ratio dpa_1/dpa_2 (i.e. $dpa_{BraggPeak}/dpa_{SteadyLoss}$) proves that above 100 MeV the dpa contribution is mainly due to the secondary particles (the Bragg peak disappears).

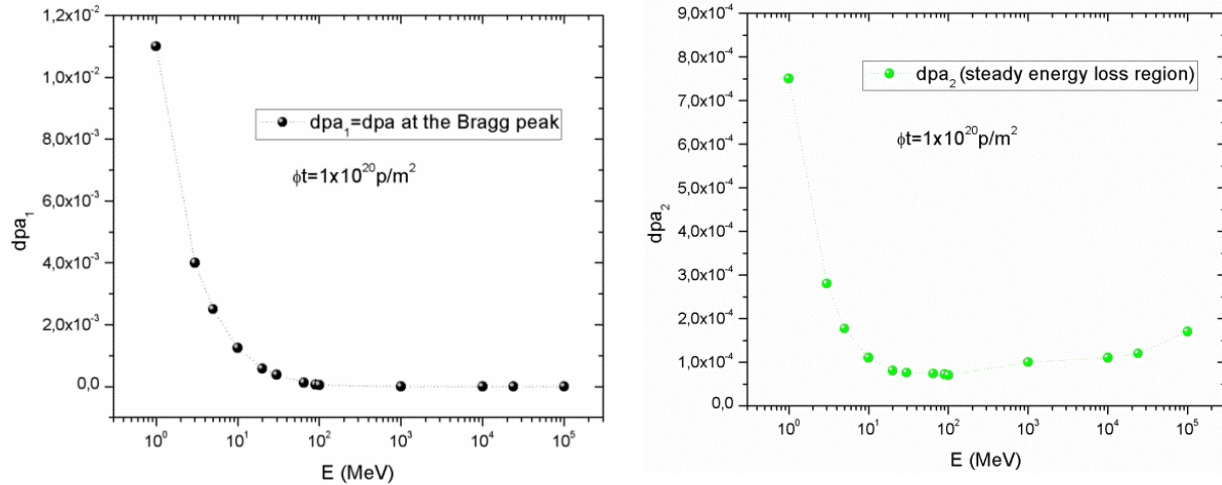


Figure 79 Evaluation of the dpa for Nb_3Sn at the Bragg peak (left, dpa_1) and in the steady energy loss region (right, dpa_2) as a function of the proton energy. The simulation is performed by means of FLUKA code.

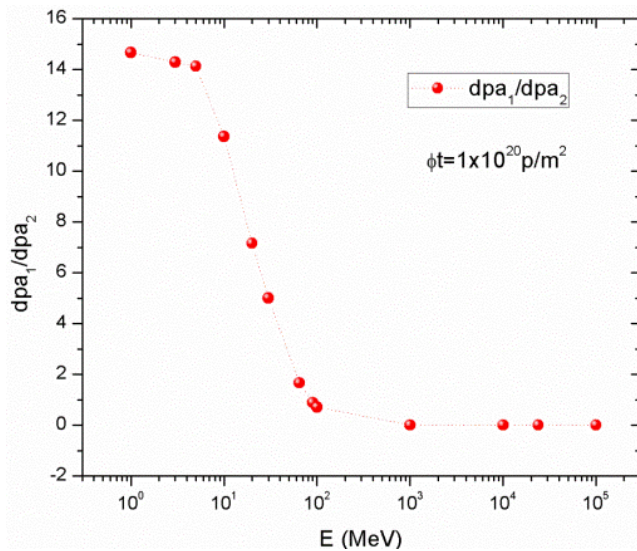


Figure 80 Ratio of the dpa_1/dpa_2 (i.e. $dpa_{BraggPeak}/dpa_{SteadyLoss}$) as a function of the energy.

In [Figure 81](#) a comparison between the dpa produced by protons and by neutrons is shown. At the maximum fluences used in both the experiments the dpa for neutrons at 1 MeV and dpa_2 (i.e. the dpa estimated in the steady energy loss region) for protons at 65 MeV and 24 GeV are about 10^{-3} explaining the same effects observed in the decrease of T_c and in the enhancement of J_c (see Subsection 4.1.4) at proton fluences one order of magnitude lower than neutron fluences. For completeness the higher dpa values calculated at the Bragg peak (dpa_1) are reported on the same graph.

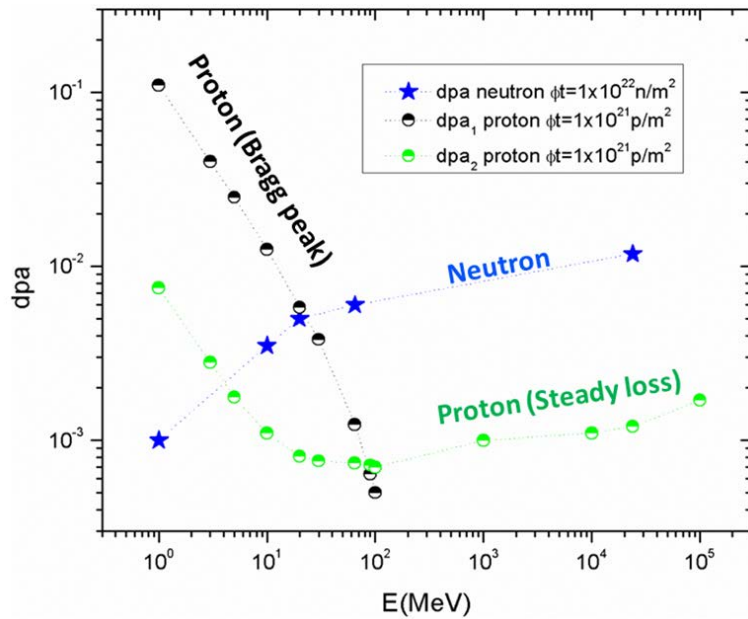


Figure 81 Comparison of dpa produced in Nb_3Sn by proton and neutron irradiation (FLUKA simulation) with energy.

Bode et al. [151] found that after low energy proton irradiation on binary Nb_3Sn wires (2.83 MeV) the $J_{c\max}$ was reached at fluence of $0.6 \times 10^{21} \text{ p/m}^2$ while as reported by Flükiger et al. [152] after low energy neutron irradiation (1 MeV) the maximum in the critical current was not observed up to fluence of $1.2 \times 10^{22} \text{ n/m}^2$ (i.e. at neutron fluence ~ 20 times higher than proton fluence). The reason behind the higher damage induced by low energy proton with respect to low energy neutron irradiation can be now explained on the basis of the dpa values shown in [Figure 81](#): 1 MeV neutrons with a fluence of $1 \times 10^{22} \text{ n/m}^2$ produce 1×10^{-3} dpa while 1 MeV protons with a fluence one order of magnitude lower than neutron ($1 \times 10^{21} \text{ p/m}^2$) create

7.5×10^{-3} dpa.

5.3. Scaling between fluence and displacement per atom (dpa)

The first problem to determine the equivalence between the measure of radiation effect in charged particle and neutron irradiation is the use of a common parameter that reflects the damage regardless the type of projectiles and energies. A good candidate to this aim is the dpa number.

As will be demonstrated hereafter the changes in the superconducting properties (T_c/T_{c0} and J_c/J_{c0}) after proton and neutron irradiation of the same Nb₃Sn wires up to fluences corresponding to those encountered in HL-LHC show a very similar variation when reported as a function of the dpa number. This proves that dpa is an appropriate quantity to measure the concentration of radiation defects.

5.3.1. Relationship between dpa and physical properties

In 1972 G. Ischenko et al. [161] irradiated Nb₃Sn layers with 24 GeV oxygen ions at fluences from 3.2×10^{13} to 1.6×10^{15} cm⁻² and compared the enhancement of the J_c vs. fluence with the data obtained after irradiation of Nb₃Sn with protons and deuterons. They observed that it was possible to rescale the curve of J_c versus a normalized fluence for the different projectiles, the maximum of J_c occurring at $\sim 2 \times 10^{16}$ cm⁻² MeV⁻¹, regardless of the type of particles, i.e. for protons, deuterons and oxygen ions.

Taking the idea from G. Ischenko [161], E.V. Semenov analyzed the literature data about irradiation on Nb₃Sn films in an internal report [162] and replaced the fluences of different ion types by the dpa values. He found that the critical current density of irradiated Nb₃Sn films as a function of dpa generally follows the same behavior having a maximum value between 0.007-0.008 dpa. This author concluded that dpa is a universal parameter to characterize the degree of radiation damage in A15 compound. However, the dpa values calculated by Semenov [162]

were obtained by means of the SRIM code which neglects the contribution to the displacement from secondary particles. The dpa calculation disregarding secondary particles leads unreasonably small values at higher energies where these contributions become dominant with respect to those of primary particles (see calculation in this work for Nb₃Sn, [Figure 82](#)).

In view of the estimation of the damage induced by high proton energies on Nb₃Sn quadrupoles for HL-LHC upgrade through a W shield it is extremely important to evaluate the dpa numbers caused by both primary and secondary particles: the complete calculation has been performed by A. Lechner et al. [2] (see Section 5.5 for further details).

In the present work, proton fluencies are converted to dpa values calculated by means of FLUKA simulation that, as described above, takes also into account the secondary particles as well as the recoil above the threshold energy (30eV).

In [Figure 82](#) a comparison between the dpa values estimated by Semenov with SRIM [162] and by the author with FLUKA [1] is presented: the strongest discrepancy occurs at high energy where the contribution of secondary particles becomes relevant, i.e. above 100 MeV.

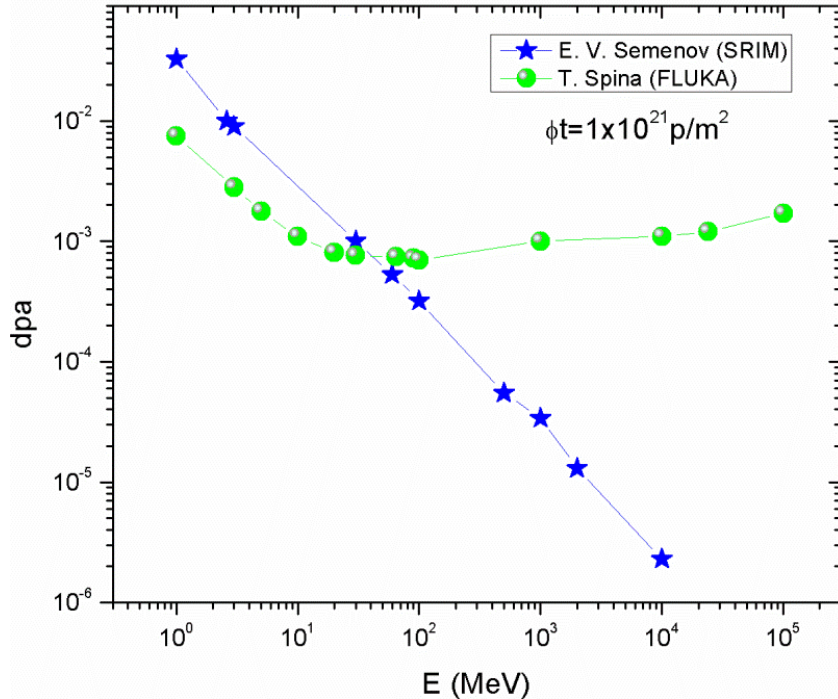


Figure 82 dpa values as a function of energy for proton irradiation on Nb₃Sn calculated using the FLUKA code (circles, this work) and the SRIM code [162].

In [Table 12](#) the dpa values obtained by FLUKA simulation corresponding to different energies, projectiles and fluences are reported.

It is interesting to note that the same value of dpa is obtained for proton fluences one order of magnitude lower than in the case of neutrons leading to the same conclusion found comparing the *slope ratio* in [Subsection 4.1.4](#).

Projectile	Energy [MeV]	Φt [p or n / m ²]	dpa [from FLUKA]
Neutron	1	1×10^{22}	1×10^{-3}
Proton	65	1×10^{21}	8×10^{-4}
Proton	24×10^3	1×10^{21}	1×10^{-3}

Table 12 Calculated dpa values (from FLUKA) for different projectiles, energies and fluences

Relationship between dpa and T_c for the Nb_3Sn wires

As explained in [Subsection 1.3.3](#) and confirmed in [Subsection 4.2.2](#) the decrease of T_c at low fluences is mainly due to the decrease of the LRO parameter, S , i.e. to the site exchanges mechanism (or antisite defects) during irradiation. On the other hand the occurrence of site exchanges is a direct consequence of the radiation induced Frenkel pairs and thus, for [equation 55](#), of dpa.

In [Figure 83](#) (PIT Ta alloyed wire (#0904)), the decrease of T_c/T_{c0} plotted as a function of the dpa values shows the same trend for the two different proton energies (24GeV and 65MeV) as observed in the decrease of T_c/T_{c0} vs fluence discussed in [Subsection 4.1.1](#). This behavior reflects that at a certain value of dpa the decrease of the critical temperature (T_c/T_{c0}) is the same regardless of the different proton energies and fluences.

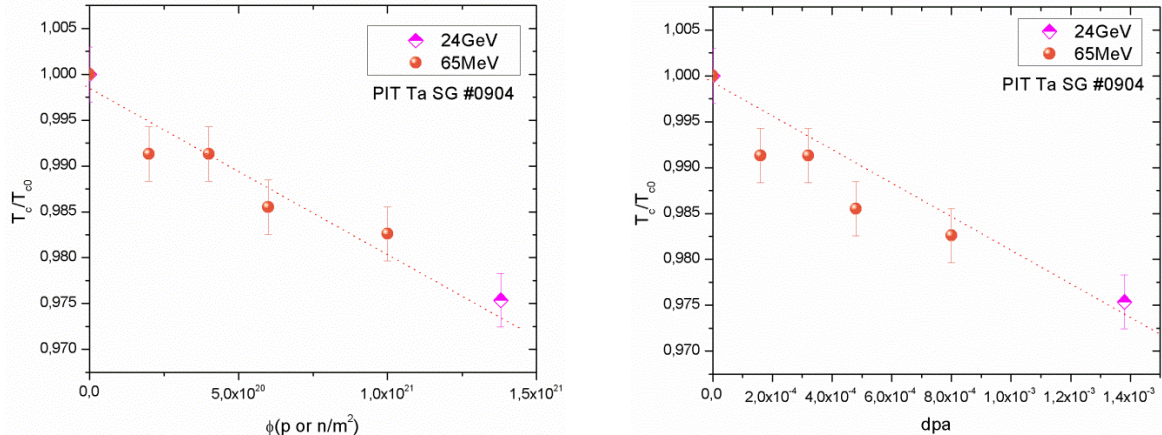


Figure 83 Decrease of the critical temperature T_c with fluence (left) and with dpa (right) for PIT Ta alloyed wire (#0904) after proton irradiation at 65 MeV and 24 GeV.

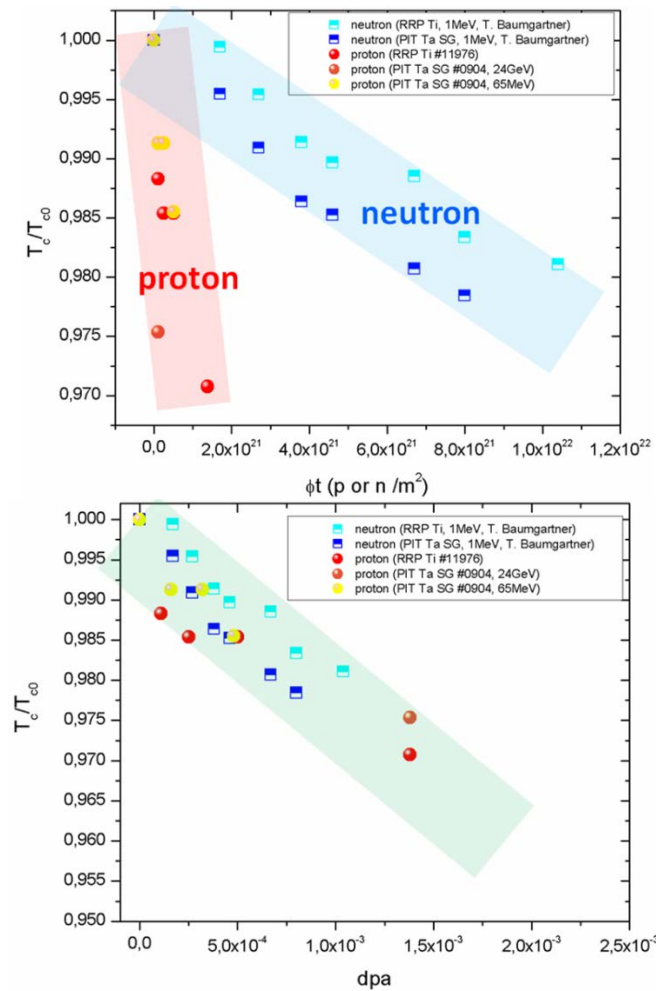


Figure 84 Comparison of the decrease of the critical temperature after proton and neutron irradiation on the same Nb₃Sn wires (PIT Ta alloyed (#0904) and RRP Ti alloyed (#11976)) as a function of fluence (top) and of dpa (bottom).

In a similar way, comparing the effects of proton and neutron irradiations on the decrease of T_c/T_{c0} (Figure 84) with dpa values a scaling behavior appears: at a certain value of dpa the decrease of T_c is the same regardless the type of projectile and the energy during irradiation.

In a general way, these results demonstrate for the first time that the dpa value is an appropriate quantity for quantifying the radiation damage that leads to the decrease of T_c .

The curve $T_c/T_{c0}(\text{dpa})$ in Figure 84 (right), will be used in Section 5.5 to predict the reduction of T_c in Nb_3Sn wires after 10 years of operation under the HL-LHC condition (or 3000 fb^{-1})

Relationship between dpa and J_c for the Nb_3Sn wires

In the present work the increase of the critical current density after irradiation was assigned to the radiation induced defect clusters acting as new pinning centers. Even if it is not possible to find a direct relationship explaining the mechanism behind the creation of defect clusters and the dpa number (as it is the case for the critical temperature), it is reasonable to think that increasing the dpa number the quantity of stable defects could increase. Indeed, as shown in Figure 86, the two curves showing the enhancement factor J_c/J_{c0} with proton fluence after proton irradiation at 24 GeV and 65 MeV for the PIT Ta alloyed wire (#0904) drop on the same curve when are plotted as a function of the dpa values. This means that 5.0×10^{-4} dpa produce an increase of J_{c0} of about 1.35 at 4.2 K and 10 T regardless the nominal value of the proton energy.

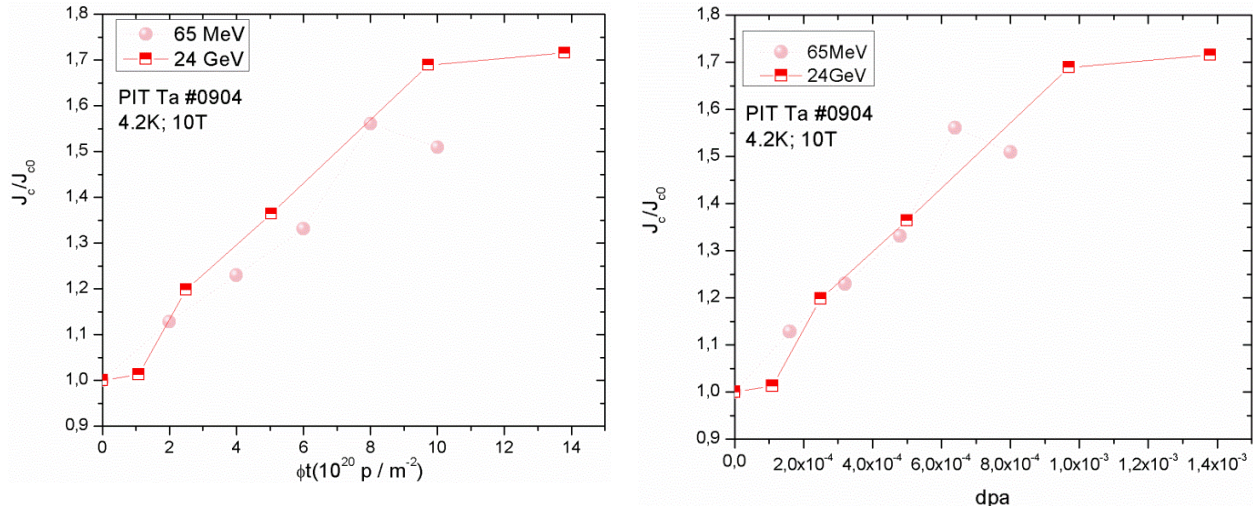


Figure 85 Enhancement of the critical current density with fluence (left) and with dpa (right) for PIT Ta alloyed wire (#0904) after proton irradiation at 24 GeV and 65 MeV.

In addition, comparing the effects of proton and neutron irradiations on the increase of J_c (Figure 87) as a function of dpa a scaling behavior appears: at a certain value of dpa the increase of J_c is the same regardless the type of projectile and the value of the energy during irradiation. From Figure 87 (right) the maximum of J_c/J_{c0} it is probably located at $> 1.4 \times 10^{-3}$ dpa, i.e. considerably lower than the value estimated by Semenov ($7 - 8 \times 10^{-3}$) [162].

It is suggested that the discrepancy with the Semenov analysis can be assigned to the different dpa values found at low energy (a factor 3-4 higher with respects to the dpa obtained by FLUKA simulation, see Figure 82) or/and to the different type of samples under investigation: binary thin films (Semenov) and ternary wires (present work).

A further reason for the difference resides in the fact that the individual dpa values extracted from the fluences reported in the literature do not take into account the precise, individual experimental conditions, which are usually not well described. This is in contrast to the present measurements, where the dpa values were determined taking into account the precise irradiation conditions (see Figure 36).

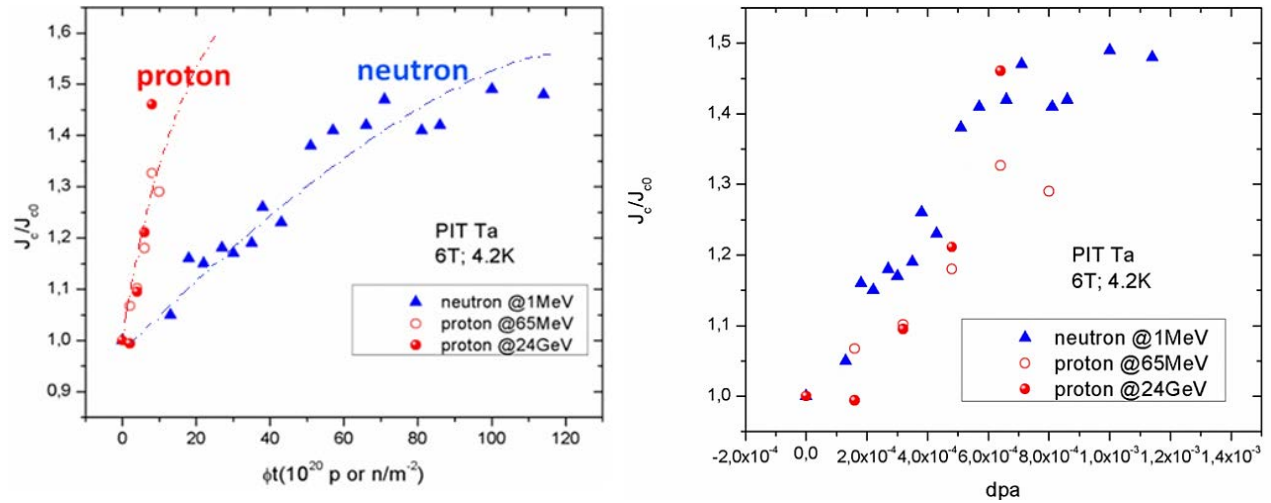


Figure 86 Comparison of the enhancement of the critical current density after proton and neutron irradiation on the same Nb₃Sn PIT wire (#0904) as a function of fluence (left) and of dpa (right).

5.4. Relationship between dpa and S

In this section the first relationship between the statistical (dpa) and the physical (S) quantity to describe the disorder induced by irradiation in Nb₃Sn is given.

In Figure 88 the experimental data for the changes of S with dpa is shown. At the same fluence the higher decrease in the S value found for the platelets at the Bragg peak can be explained in terms of the higher value of dpa.

The relationship between S and dpa can be described regardless the type of energy loss with the empirical function:

$$S = S_0 e^{-k dpa} \quad 58$$

where S_0 is the LRO parameter before irradiation, i.e. 0.98, and k a constant to define the convexity of the curve.

Fitting the experimental data with the function given in equation 58 and fixing the $dpa \geq 0$ and $0 \leq S \leq 1$ the value $k=2.562$ is found. The curve fitting is shown in Figure 89 and represents for the first time the relationship between S and dpa.

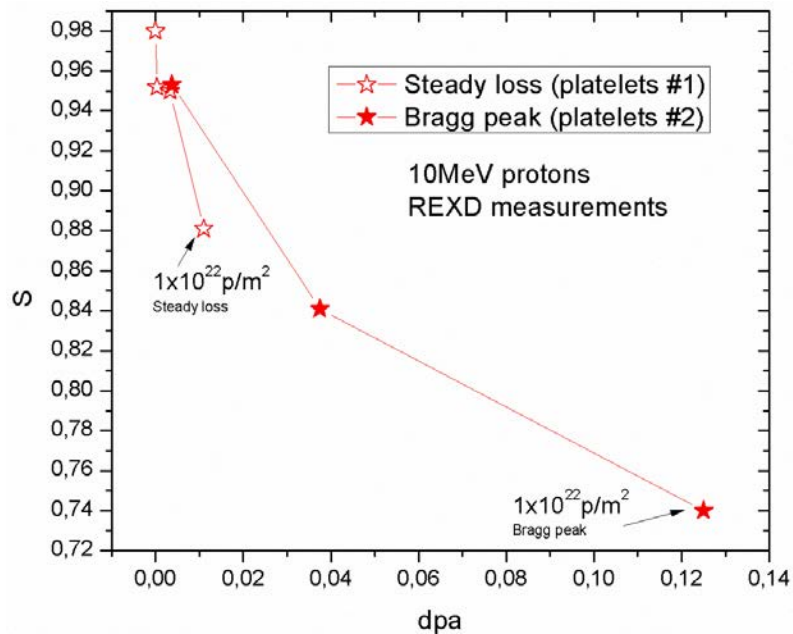


Figure 87 Variation of the LRO parameter S with dpa. At the same fluence the higher decrease of S for platelets #2 corresponds to higher dpa values.

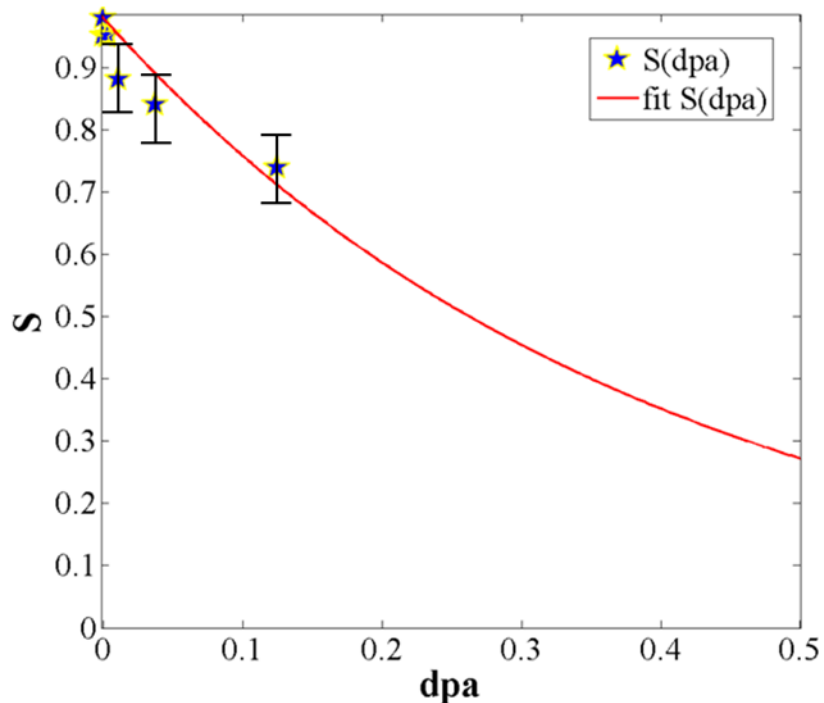


Figure 88 Relationship between the Bragg Williams LRO parameter (S) and the displacement per atom (dpa).

5.5. The effects of protons and neutrons irradiation on the performance of Nb₃Sn quadrupoles for HL-LHC Upgrade

The performance of the Nb₃Sn quadrupole magnets of QXF type (described by Ferracin et al. in [163]) in the High Luminosity LHC Upgrade accelerator during operation up to an integrated luminosity of 3000 fb⁻¹ is an important issue.

To reduce the peak energy deposition in the coils and to remove a considerable part of the heat load from the 1.9 K cooling system Esposito et al. [136] proposed to shield the magnet with a tungsten insert of several mm thickness.

After introducing the W shield, Lechner et al. [2] estimated that the radiation load (by high energy neutrons, protons, pions and especially electrons, positrons, and gammas) on the innermost winding of the quadrupoles will be considerably reduced from hundreds to few tens of MGy. In addition they calculated a maximum dpa value of 1.8×10^{-4} in the Q1 quadrupole, being mostly due to the hadronic shower: in particular the neutron contributions to the total dpa is 70,7%, while $\sim 25\%$ are due to ions and pions above transport threshold ($>1\text{keV}$). Only 1.7% is due to protons above transport threshold ($>1\text{keV}$).

Taking into account the total dpa value predicted for HL-LHC it is possible to predict the degradation of T_c during the entire acceleration lifetime. Indeed, considering Figure 84 (right) described above, the calculation of the dpa values based on the FLUKA code shows that for both proton and neutron irradiation the variation of T_c with the dpa value is very similar in the dpa range between 1×10^{-4} and 1.4×10^{-3} . It can be concluded that the total dpa value of 1.8×10^{-4} leads to a decrease of T_c by ~ 0.3 K.

Such a small decrease of T_c is not expected to affect the stability of the Nb₃Sn quadrupoles.

CONCLUSIONS AND PERSPECTIVES

The High Luminosity LHC project aims to reach an integrated luminosity of 3000 fb^{-1} , i.e. ten times more than the nominal LHC performance expected for 2010-2021. To reach this ambitious goal larger aperture magnets (150mm) in the region spanning from the interaction point to the matching section quadrupoles are required. The baseline is the Nb_3Sn technology, which allows a more compact layout and about 30% higher luminosity than those with NbTi wires.

The higher luminosity poses issue on the heat load and on the radiation damage.

Thus, in order to estimate the lifetime of these insertion quadrupole magnets during operation conditions a precise prediction of the potential damage on the superconductors caused by the simultaneous action of high energy irradiation sources is needed.

Due to the lack of multi-source reactors it is only possible to study the effects of each type of particles separately.

In particular, the present work had the scope to investigate how the critical properties of Nb_3Sn changes after proton irradiations.

After a theoretical introduction on the radiation damage in A15 compounds the whole work can be subdivided in three major parts:

1. The effects of proton irradiation on the critical properties (J_c , T_c , B_{c2}): on the Nb_3Sn wires;
2. The effects of proton irradiation on the crystallographic structure of Nb_3Sn platelets: i.e. the variation of the lattice constant, of the microstrains and of the Bragg Williams LRO parameter;
3. Quantification of the proton and neutron damage by means of dpa (displacement per atom).

Conclusion 1:**Changes induced by protons at 24 GeV and 65 MeV on the critical properties of Nb₃Sn industrial multifilamentary wires**

After room temperature proton irradiations at 24 GeV and 65 MeV and fluences up to $1.38 \times 10^{21} \text{ p/m}^2$ changes in the critical properties of ternary alloyed RRP and PIT Nb₃Sn wires are observed: J_c increases strongly with fluence, while B_{c2} shows only a moderate increase (of the order of 5%). On the other hand, T_c at low fluences decreases linearly with ϕt due to the decrease of atomic ordering. The small variation of the superconducting transition width with fluence suggests a homogeneous disorder in the filaments, in analogy to neutron irradiation, where the homogeneity was proven by specific heat measurements.

The negligible variation in the slope of $T_c(\phi t)$ for different energies shows that the effect on T_c induced by the two proton sources is similar, in spite of the very different energies.

Up to the present fluences, the expected maximum values of J_c/J_{c0} have not been reached, but the shape of the curves $J_c(\phi t)$ indicates that they may be close: from proton irradiations at 30 MeV at $3 \times 10^{21} \text{ p/m}^2$ in Kurchatov on the same wires (not discussed in the present work, the measurements still going on), we conclude that the maximum of J_c/J_{c0} may be situated at a fluence around $2 \times 10^{21} \text{ p/m}^2$. In spite of the different energies and regardless of the fabrication techniques (RRP and PIT), the enhancement of J_c/J_{c0} with fluence is similar for Ta alloyed wires. The value of J_c/J_{c0} of the Ti alloyed wire exhibits a stronger increase than Ta alloyed wires.

A modified two-mechanism model was introduced to analyze the variation in the volume pinning force after irradiation: the first contribution describes grain boundary pinning (assuming that this contribution is not affected by irradiation at the present fluences), the second contribution being described by a radiation induced point pinning defect mechanism.

A comparison of T_c and J_c with the results obtained after neutron irradiation in the frame of the collaboration with Baumgartner *et al.* [4] on the same wires shows that proton irradiation in the steady loss region causes already the same damage at fluences being one order of magnitude lower.

Conclusion 2:**Changes of the crystallographic structure of Nb_3Sn after proton irradiation at 10 MeV**

After 10 MeV proton irradiations of Nb_3Sn platelets up to fluences of $1.0 \times 10^{22} \text{ p/m}^2$, changes in the crystallographic parameters are observed by means of Synchrotron measurements: both the microstrains and the lattice constant increase while the Bragg Williams LRO parameter, S , decreases.

It was shown that the effects of proton irradiations are considerably more pronounced in the platelets where the Bragg peak occurs reflecting the inhomogeneous damage induced by protons in this region.

A good agreement with the exponential behavior of $T_c/T_{c0}(S/S_0)$ introduced by Sweedler et al. [79] after neutron irradiation has been found for the Nb_3Sn platelets located in the steady loss region confirming the similar behavior of protons and neutrons at proton fluences about one order of magnitude lower than neutron fluences. As expected, a deviation from this trend has been reported for the platelets including the Bragg peak, where the effect is markedly stronger.

Conclusion 3:**Relationship between the dpa values and the physical changes**

It was found that the effects induced by high energy protons (charged particles) and neutrons on the critical properties of Nb_3Sn wires can be correlated with the introduction of a statistical quantity, i.e. the displacement per atom (dpa).

Substituting the fluences with the dpa values obtained by means of Monte Carlo simulation (FLUKA code) and comparing the effects of proton and neutron irradiations on the decrease of T_c/T_{c0} with dpa values a scaling behavior appears: at a certain value of dpa the decrease of T_c is the same regardless the type of projectile and the energy during irradiation. It follows that the dpa value is an appropriate quantity for quantifying the radiation damage with different projectiles leading to a decrease of T_c .

This important result allows us to predict the reduction of T_c (about 0.3 K) in Nb_3Sn wires after 10 years of operations under the HL-LHC condition (3000 fb^{-1}). Since at the same time J_c exhibits a marked increase, the radiation effects on the superconductor are not expected to affect the stability of the Nb_3Sn quadrupole.

To completely answer the question about the thermal stability of the quadrupoles, further investigations on the reduction of the RRR of the Cu matrix in the Nb_3Sn wires after high energy irradiations at low temperature, followed by a recovery at 300 K, would be needed.

Résumé

Afin d'estimer la durée de vie des quadripôles dans l'accélérateur à Haute-Luminosité (HL-LHC), une connaissance précise des dommages potentiels dans les supraconducteurs causés par l'action simultanée de plusieurs sources d'irradiation à haute énergie est nécessaire.

Le présent travail traite les effets de l'irradiation de protons de haute énergie sur les propriétés physiques de Nb_3Sn , le matériau supraconducteur utilisé dans les quadripôles de HL - LHC: la densité de courant critique (J_c), la température critique (T_c), le champ critique supérieur (H_{c2}) et enfin le paramètre d'ordre atomique de Bragg - Williams (S) dans les fils de Nb_3Sn constituant les quadripôles.

Le présent travail peut être subdivisé en cinq parties:

- a) Etude du comportement de fils irradiés par des protons à haute énergie qui traversant le fil (région de perte régulière, excluant l'emplacement du pic de Bragg): dans ce cas, une comparaison directe avec l'irradiation neutronique sur les mêmes fils de Nb_3Sn est effectuée.
- b) Etude de la mise en valeur de J_c après irradiation par protons: un modèle à deux mécanismes a été introduit pour analyser la force d'épinglèrent prenant en compte la contribution des défauts induits par rayonnement supplémentaire à celle due aux limites de grain.
- c) Etude de la zone du pic de Bragg de fils irradiés par protons à haute énergie. Dans cette région les protons subissent une perte totale d'énergie; il n'y a aucune analogie avec l'irradiation neutronique. Les effets de l'irradiation dans la région du pic de Bragg sur les propriétés de la structure Nb_3Sn n'avaient jamais été étudiés avant le présent travail.
- d) Le but de ce travail était d'établir une corrélation entre les valeurs du déplacement par atome (dpa) et la variation du paramètre d'ordre atomique, S , dans le Nb_3Sn , ainsi que la variation corrélée de T_c au courant de la durée opérationnelle.

e) Application des résultats au problème des dommages causés par radiation dans l'accélérateur HL-LHC: étude des effets de l'irradiation sur la stabilité thermique des quadripôles de Nb_3Sn pour HL-LHC mise à niveau.

La thèse est structurée en cinq chapitres:

- Le premier chapitre contient un aperçu des concepts physiques expliquant dégâts dus à l'irradiation des fils supraconducteurs;
- Le deuxième chapitre décrit la caractérisation des fils de Nb_3Sn et la préparation des plaquettes de Nb_3Sn . Sont ainsi qu'une analyse détaillée de l'ordre atomique décrites à fournir une connaissance détaillée de l'ordre atomique dans les plaquettes avant l'irradiation;
- Dans le troisième chapitre, les différents types de mesure pour quantifier les effets de l'irradiation sont décrits; des détails sur l'activation après l'irradiation protonique sont donnés;
- Dans le quatrième chapitre, la variation des propriétés physiques des fils et des plaquettes de Nb_3Sn après irradiation est décrite. L'effet de l'irradiation sur les forces d'ancrage est décrit par un modèle à deux composantes, provenant des joint de grains et des nouveaux centres induits par la radiation (point pinning centres);
- Dans le cinquième chapitre de la comparaison entre les effets des rayonnements induits par les protons (particules chargées) et neutrons sur les propriétés critiques de fils Nb_3Sn particules chargées et de l'irradiation neutronique sur les propriétés critiques de fils Nb_3Sn sont corrélés, avec l'introduction d'une quantité statistique, à savoir le déplacement par atome (dpa) calcule au moyen de la simulation de Monte Carlo (le code FLUKA). Ceci a mené à une nouvelle corrélation: en effet, nous avons montré pour la première fois que les effets de l'irradiation à haute énergies per différentes particules sur T_c peuvent être représentés par une seule variable: le nombre dpa.

Ce résultant important permet de prédire l'abaissement de T_c dans les quadripôles de HL-LHC au courant de l'opération jusqu'à la luminosité de 3000 fb^{-1} . Vu qu'en même temps le courant critique augmente régulièrement, il ressort que la stabilité thermique des quadripôles n'est pas influencée par les effets sur le supraconducteur.

Une étude complète de la stabilité thermique requiert une étude approfondie de l'abaissement du nombre RRR du Cu entourant les fils de Nb_3Sn après irradiation à basse température et les conditions de rétablissement de ce paramètre lors de cycles de réchauffement à 300 K.

BIBLIOGRAPHY

- [1] A. Fassò, A. Ferrari, J. Ranft and P. Sala, "FLUKA," FLUKA team, 2000-2015. [Online]. Available: <http://www.fluka.org/fluka.php>. [Accessed 14 March 2015].
- [2] A. Lechner, L. Esposito, F. Cerutti, A. Ferrari, G. Steele and N. Shetty, "FLUKA radiation damage calculations for colliders like the HL-LHC," in *RESMM*, Wroclaw, Poland, May 12-15, 2014.
- [3] E. Todesco, H. Allain, G. Ambrosio, G. Arduini, F. Cerutti, R. De Maria, L. Esposito, S. Fartoukh, P. Ferracin, H. Felice, R. Gupta, R. Kersevan, N. Mokhov, T. Nakamoto, I. Rakno, J. M. Rifflet, L. Rossi, G. L. Sabbi, M. Segreti, F. Toral, Q. Xu, P. Wanderer and R. van Weelderen, "A first baseline for the magnets in the High Luminosity LHC insertion regions," *CERN-ACC-2014-0036*, 2014.
- [4] T. Baumgartner, "Effects of fast neutron irradiation on critical currents and intrinsic properties of State-of-the-Art Nb₃Sn wires," [Available Online]: <http://www.ub.tuwien.ac.at/diss/AC10774721.pdf>, Vienna, 2013.
- [5] F. Cerutti, A. Lechner, A. Mereghetti and A. Brugger, "Particle fluence on LHC magnets," in *Proc. WAMSDO Workshop Accel. Magn. Supercond. Design Optim.*, CERN, Geneva, Nov. 2011.
- [6] B. T. Matthias, T. H. Geballe, S. Geller and E. Corenzwit, "Superconductivity of Nb₃Sn," *Phys. Rev.*, vol. 95, p. 1435, 1954.
- [7] M. Cyrot and D. Pavuna, *Introduction to Superconductivity and High T_c Materials*, World Scientific Publishing Co Pte. Ltd., 1992.
- [8] J. Friedel and J. Labbé, *J. Phys. Radium*, vol. 27, 1966.
- [9] J. Muller, "A15-type superconductors," *Rep. Prog. Phys.*, vol. 43, 1980.
- [10] D. Dew Hughes, "Superconducting A-15 compounds: A review," *Cryogenics*, vol. 15, no. 8, pp. 435-454, 1975.
- [11] P. Anderson and P. W. Morel, *Phys. Rev.*, vol. 125, p. 1263, 1962.
- [12] W. L. McMillan, "Transition Temperature of Strong-Coupled Superconductors," *Phys. Rev.*, vol. 167, pp. 331-334, 1967.
- [13] R. Flükiger, "Phase Relationships, Basic Metallurgy And Superconducting Properties of Nb₃Sn and Related compounds," vol. 28, pp. 399-413, 1982.

- [14] A. Godeke, "A review of the properties of Nb₃Sn and their variation with A15 composition, morphology and strain state," *Supercond. Sci. Technol.*, vol. 19, no. 8, 2006.
- [15] W. Goldacker and R. Flukiger, "Phase transitions and superconducting properties of binary and Ti, Ta, Ga and H alloyed Nb₃Sn," *Physica B+C, Elsevier*, vol. Volume 135, no. 1–3, p. 359–363, 2 December 1985.
- [16] H. Devantay, J. Jorda, M. Decroux, J. Muller and R. Flukiger, *Journal of Material Science*, vol. 16, p. 2145, 1981.
- [17] R. Flukiger, W. Goldacker and R. Isernhagen, "Characterization of bulk and multifilamentary Nb₃Sn and Nb₃Al by diffractometric and resistive measurements," *Advances in Cryogenic Engineering Materials*, vol. 32, pp. 925-936, 1986.
- [18] R. L. Flukiger, Ordering, Phase Superconductivity Filamentary A15 Type Compounds, KfK 4204, 1987.
- [19] E. Drost, W. Specking and R. Flukiger, "Comparison of superconducting properties and residual resistivities of bronze processed Nb₃Sn wires with Ta, Ti and Ni+Zn," *IEEE Transactions on Magnetics*, vol. 21, no. 2, p. 281–284, 1985.
- [20] R. Flukiger, D. Uglietti, C. Senatore and F. Buta, "Microstructure, composition and critical current density of superconducting Nb₃Sn wires," *Cryogenics*, 48, vol. 48, no. 7-8, p. 293–307, 2008.
- [21] A. K. Ghosh, L. D. Cooley, J. A. Parrell, M. B. Field, Y. Zhang and S. Hong, "Effects of reaction temperature and alloying on performance of restack-rod-process Nb₃Sn," *IEEE Transactions on Applied Superconductivity*, vol. 17, no. 2, pp. 2623-2626, 2007.
- [22] R. M. G. Ozeryancky and E. Schwall, "Critical current and upper critical field of multifilament Nb_{3-x}Ta_xSn superconductor," *Journal of Applied Physics*, vol. 56, no. 3, p. 814–818, 1984.
- [23] M. Suenaga, "Optimization of Nb₃Sn," *IEEE Transactions on Magnetics*, vol. 21, no. 2, p. 1122–1128, 1985.
- [24] T. Asano, Y. Iijima, K. Itoh and K. Tachikawa, "Effects of titanium addition to the niobium core on the composite-processed Nb₃Sn," *Transactions of the Japan Institute of Metals*, vol. 27, no. 3, pp. 204-214, 1986.
- [25] P. E. Johnson-Walls, D. R. Dieterich, W. V. Hassenzahl and J. W. Morris Jr, "The microstructural state of Nb₃Sn in a multifilamentary titanium doped bronze-process wire," *IEEE Transactions on Magnetics*, vol. 21, no. 2, pp. 1137-1139, 1985.

- [26] H. Sekine, K. Itoh and K. Tachikawa, "A study of the H_c2 enhancement due to the addition of Ti to the matrix of bronze-processed Nb_3Sn superconductors," *Journal of Applied Physics*, vol. 63, no. 6, pp. 2167-2170, 1988.
- [27] J. L. Jorda, R. L. Flukiger and J. Muller, *J. Less-Common Met.*, vol. 75, p. 227, 1980.
- [28] W. Bragg and E. J. Williams, "The Effect of Thermal Agitation on Atomic Arrangement in Alloys," *Proc. R. Soc. Lond. A*, vol. 145, pp. 699-730, 1934.
- [29] R. L. Flukiger, Eds. A. Schmid, W. Weber, H. Wühl, North-Holland, Proc. LT 17, Karlsruhe, 1984.
- [30] E. C. Van Reuth and N. J. Poulis, "NMR results on the variation of T_c in V_3Au with atomic ordering," *Physics Letters*, vol. 25A, no. 5, pp. 390-391, June 1967.
- [31] E. C. Van Reuth and R. M. Waterstrat, "Atomic Ordering in Binary A15-Type Phases," *Acta Cryst.*, vol. B24, pp. 186-196, 1968.
- [32] R. L. Flukiger, J. L. Staudenmann and P. Fischer, *J. Less-Common Metals*, vol. 50, p. 253, 1976.
- [33] Full Prof manual, <https://www.ill.eu/sites/fullprof/php/tutorials.html>.
- [34] D. T. Mann and J. B. Cromer, "X-ray scattering factors computed from numerical Hartree-Fock wave functions," *Acta Crystallographica Section A*, vol. 24, no. Part 2, March 1968.
- [35] J. J. Hanak, K. Strater and G. W. Cullen, *RCA Rev.*, vol. 25, p. 342, 1964.
- [36] R. D. Blaughter, R. E. Hein, J. E. Cox and R. M. Waterstrat, "Atomic ordering and superconductivity in A-15 compounds," *Journal of Low Temperature Physics*, vol. 1, no. 6, pp. 539-561, 1969.
- [37] R. L. Flukiger, A. Paoli and J. M. Muller, *Solid State Comm.*, vol. 14, p. 443, 1974.
- [38] J. M. Muller, R. L. Flukiger, A. Junod, F. Heiniger and C. Susz, Plenum Press, New York: in Low Tem. Physics LT-13, K. D. Timmerhaus, W. J. O'Sullivan and E. F. Hammel, eds., p. 446, 1974.
- [39] A. R. Sweedler, D. E. Cox and S. Moehlecke, "Neutron irradiation of superconducting compounds," *Journal of Nuclear Materials*, vol. 72, no. 1-2, pp. 50-69, 1978.
- [40] J. Appel, "Atomic ordering and T_c of narrow-band superconducting alloys," *Phys. Rev. B*, vol. 13, no. 7, pp. 3203-3208, 1976.
- [41] L. P. Gor'kov, "Theory of superconducting alloys in a strong magnetic field near the critical temperature," *Soviet Physics JETP*, vol. 37, no. 10, pp. 998-1004, 1960.

- [42] G. S. Was, *Fundamentals of Radiation Materials Science - Metals and Alloys*, Ann Arbor (USA): ISBN 978-3-540-49471-3 Springer Berlin Heidelberg New York, 2007.
- [43] D. Kiselev, "Activation and radiation damage in the environment of hadron accelerators," to be published.
- [44] G. Vogl, "Radiation Damage and Structural Lattice Defects," *Journal de Physique Colloques*, vol. 35, no. C6, pp. C6-165-C6-180, 1974.
- [45] G. H. Kinchin and R. S. Pease, *Jurnal Appl. Phys.*, vol. 25, p. 344, 1954.
- [46] P. Hosemann, "Studying Radiation Damage in Structural Materials by Using Ion Accelerators," *Review of Accelerator Science and Technology*, vol. 4, pp. 161-182, 2011.
- [47] L. S. Schioett, J. Lindhard, V. Nielsen and M. Scharff, *Kgl Dan Vidnsk Selsk Mat Fyf Medd*, vol. 36, no. 10, 1968.
- [48] M. J. Norgett, M. T. Robinson and I. M. Torrens, *Nucl. Eng. Des.*, vol. 33, pp. 50-54, 1975.
- [49] J. A. Mascitti and M. Madariaga, "Method for the calculation of DPA in the reactor Pressure Vessel of Atucha II," *Science and Technology of Nuclear Installation*, p. 6, 30 November 2010.
- [50] E. M. Schulson, "The ordering and disordering of solid solutions under irradiation," *Journal of Nuclear Materials*, vol. 83, pp. 239-264, 1979.
- [51] J. Ziegler, "The Stopping and Range of Ions in Matter (SRIM)," vol. <http://www.srim.org/>.
- [52] J. Staudenmann, *Helv. Phys. Acta*, vol. 47, p. 39, 1974.
- [53] J. Staudenmann, *Solid State Comm.*, vol. 23, p. 121, 1977.
- [54] D. O. Welch, G. J. Dienes and O. W. Lazareth Jr, *IEEE Trans. Magn.*, Vols. MAG-19, p. 889, 1983.
- [55] D. O. Welch, G. J. Dienes, O. W. Lazareth Jr and R. D. Hatcher, *J. Phys. Chem. Sol.*, vol. 45, p. 1225, 1984.
- [56] A. Seeger, *in Proc. 2nd UN Intl. Conf. Peaceful Uses of Atomic Energy (Geneva)*, vol. 6, p. 250, 1958.
- [57] A. Seeger, "Radiation Damage in Solids," *IAEA*, vol. 1, p. 101, 1962.
- [58] F. Rullier-Albenque, "PhD Thesis," University of Paris/Orsay (F), 1984.
- [59] K. Y. Liou and P. Wilkes, *J. Nucl. Mater.*, vol. 87, p. 317, 1979.

[60] "NIST, National Institute of Standards and Technology," [Online]. Available: http://physics.nist.gov/cgi-bin/Star/ap_table.pl. [Accessed 27 02 2015].

[61] A. Konobeyev, U. Fischer, C. H. M. Broeders and L. Zanini, "Displacement cross section files for structural materials irradiated with neutrons and protons," IAEA, Report NDS-214, <http://www-nds.iaea.org/displacement/iaea-nds-0214.pdf>., 2009.

[62] I. V. Voronova, N. N. Mihailov, G. V. Sotnikov and V. J. Zaikin, "The influence of radiation damage on the superconducting properties of Nb₃Sn," *Journal of Nuclear Materials*, vol. 72, pp. 129-141, 1978.

[63] H. Kupfer, R. Meier-Hirmer and T. Reichert, "Field dependent change of the critical current density in neutron irradiated A15 superconductors with grain boundary pinning," *Journal of Applied Physics*, vol. 51, no. 2, pp. 1121-1126, 1980.

[64] F. Weiss, R. L. Flukiger, W. Maurer, P. A. Hahn and M. W. Guinan, "Changes in superconducting properties by room-temperature neutron-irradiation for binary and alloyed Nb₃Sn multifilamentary wires," *IEEE Transactions on Magnetics*, vol. 23, no. 2, p. 976-979, 1987.

[65] S. T. Sekula, "Effect of irradiation on the critical currents of alloyed and compound superconductors," *Journal of Nuclear Materials*, vol. 72, pp. 91-113, 1978.

[66] H. Bauer, E. J. Saur and D. G. Schweitzer, "Effect of neutron irradiations on superconducting properties of A-15 compounds undoped and doped with ¹⁰B and ²³⁵U," *Journal of low temperature physics*, vol. 19, no. 3/4, pp. 171-187, 1975.

[67] T. Allen and G. S. Was, "Intercomposition of microchemical evolution under various types of particle irradiation," *Journal of Nuclear Materials*, vol. 205, pp. 332-338, 1993.

[68] K. Wohlleben and H. J. Bode, "Enhancement of superconducting critical current density in Nb₃Sn diffusion layers produced by irradiation with protons," *Phys. Lett.*, vol. 24 A, no. 1, pp. 25-27, 1966.

[69] G. W. Cullen, R. L. Novak and J. P. McEvoy, *RCA-Review*, vol. 25, p. 479, 1964.

[70] L. R. Aronin, "Radiation damage effects on order-disorder in nickel-manganese alloys," *Journal of Applied Physics*, vol. 25, no. 3, pp. 344-349, 1954.

[71] R. Bett, "The effects of neutron irradiation damage on the superconducting properties of Nb₃Sn," *Cryogenics*, vol. 14, no. 7, pp. 361-366, 1974.

[72] P. A. Hahn, M. W. Guinan, L. T. Summers, T. Okada and D. B. Smathers, "Fusion neutron irradiation effects in commercial Nb₃Sn superconductors," *Journal of Nuclear Materials*, Vols. 179-181, pp.

1127-1130, 1991.

[73] F. Weiss, R. Flukiger, W. Maurer, P. A. Hahn and M. W. Guinan, *IEEE Transactions on Magnetics*, vol. 23, no. 2, p. 976-979, 1987.

[74] S. Moehlecke, A. R. Sweedler and D. E. Cox, *Phys. Rev. B*, vol. 21, p. 2712, 1980.

[75] J. A. Tarvin and D. E. Cox, *Phys. Rev. B* 18, vol. 22, 1978.

[76] R. Caton and R. Viswanathan, *Phys. Rev. B*, vol. 18, p. 15, 1978.

[77] R. Viswanathan, R. Canton and C. S. Pande, *J. Low Temp. Phys.*, vol. 30, no. 1978, p. 503.

[78] B. Cort, G. R. Stewart, C. L. Snead Jr, A. R. Sweedler and S. Moehlecke, *Phys. Rev.*, vol. B24, p. 379, 1981.

[79] A. R. Sweedler, D. G. Schweizer and G. W. Webb, *Phys. Rev. Lett.*, vol. 33, p. 168, 1974.

[80] A. R. Sweedler, D. E. Cox and L. Newkirk, *J. Electronic Materials*, vol. 4, p. 883, 1975.

[81] C. S. Pande, *Sol. State Comm.*, vol. 24, p. 241, 1977.

[82] A. R. Sweedler, D. Cox, D. G. Schweitzer and G. W. Webb, "Neutron induced disorder in superconducting A-15 compounds," *IEEE Transactions on Magnetics*, vol. 11, no. 2, pp. 163-165, 1975.

[83] B. Seeber and O. Meyer, "Channelling effect measurements of 4He-induced damage in V3Si single crystals," *Sol. State Comm.*, vol. 22, pp. 603-607, 1977.

[84] L. R. Testardi, J. M. Poate and H. J. Levinstein, *Phys. Rev. B*, vol. 15, p. 2570, 1977.

[85] L. R. Testardi, R. L. Meek, J. M. Poate, W. A. Royer, A. R. Storm and J. H. Wernick, *Phys. Rev. B*, vol. 11, p. 4304, 1975.

[86] J. M. Poate, R. C. Dynes, L. R. Testardi and R. H. Hammond, in *Superconductivity in d- and f- Band Metals*, New York, Ed. D. H. Douglass, Plenum Press, 1976, p. 489.

[87] O. Meyer and J. Pfluger, *Solid State Commun.*, vol. 32, p. 1148, 1979.

[88] U. Schneider, G. Linker and O. Meyer, *J. Low Temp. Phys.*, vol. 47, p. 439, 1982.

[89] R. D. Burbank, R. C. Dynes and J. M. Poate, *J. Low Temp. Phys.*, vol. 36, p. 573, 1979.

[90] G. Saemann-Ischenko and C. Nolscher, *Phys. Rev. B*, vol. 32, p. 1519, 1985.

[91] T. Okada, M. Fukumoto, K. Katagiri, K. Saito, H. Kodaka and H. Yoshida, "Effects of irradiation and strain in a bronze processed multifilamentary Nb3Sn superconducting composite," *IEEE Trans. on Magn.*, Vols. MAG-23, no. 2, pp. 972-975, 1987.

[92] G. De Marzi, L. Morici, L. Muzzi, A. della Corte and M. Buongiorno Nardelli, "Strain sensitivity and superconducting properties of Nb3Sn from first principles calculations," *J. Phys. Condens. Matter*, vol. 25, no. 13, 2013.

[93] A. E. Karkin, A. V. Mirmelshtein, V. E. Arkhipov and B. N. Goshchitskii, *Phys. Stat. Sol. (a)*, vol. K117, p. 61, 1980.

[94] B. Cort, G. R. Stewart, C. L. Snead, A. R. Sweedler and S. Moehlecke, *Phys. Rev. B*, vol. 24, p. 3794, 1981.

[95] R. L. Flukiger, S. Foner and E. J. McNiff Jr, in *Superconductivity of d and f Band Metals*, New York, Eds. H. Suhl and M.B. Maple, Academic Press Inc., 1980, p. 265.

[96] S. Moehlecke, D. E. Cox, A. R. Sweedler and J. Less, *Common Metals*, vol. 62, p. 111, 1978.

[97] S. A. Alterovitz, D. E. Farrell and B. S. Chandrasekhar, "Superconductivity of proton irradiated V3Si," *Phys. Rev. B*, vol. 24, no. 1, p. 90, 1981.

[98] D. M. Parkin and C. L. Snead Jr, *Nuclear Technology*, vol. 29, no. 3, pp. 264-267, 1976.

[99] T. Baumgartner, M. Eisterer, H. W. Weber, R. L. Flukiger, C. Scheurlein and L. Bottura, "Effects of neutron irradiation on pinning force scaling in state of the art Nb3Sn wires.," *Superconductor Science and Technology*, vol. 27, 2014.

[100] B. S. Brown, T. H. Blewitt, D. G. Wozniak and M. Suenaga, "Critical current changes in Nb3Sn irradiated with fast neutrons at 6 K," *Journal of Applied Physics*, vol. 46, no. 12, pp. 5163-5168, 1975.

[101] S. L. Colucci, H. Weinstock and M. Suenaga, "Critical current enhancement in Nb3Sn by low-temperature fast-neutron irradiation," *Journal of Applied Physics*, vol. 48, no. 2, pp. 837-838, 1977.

[102] M. Fähnle, "The influence of fast neutron irradiation on the critical current densities in Nb3Sn. I. Low neutron doses ($\Phi < 2 \times 10^{18}$ neutrons/cm²)," *Physica Status Solidi (B)*, vol. 84, no. 1, pp. 245-251, 1977.

[103] K. Wohlleben and H. J. Bode, "Enhancement of superconducting critical current density in Nb₃Sn diffusion layers produced by irradiation with protons," *Phys. Letters*, vol. 24A, no. 1, pp. 25-27, November 1966.

[104] C. L. Snead Jr, "Low-temperature 30 GeV-proton effects on critical properties of type-II superconducting filamentary conductors," *Journal of Nuclear Materials*, vol. 72, no. 1-2, pp. 190-197, 1978.

[105] T. Baumgartner, M. Eisterer, H. W. Weber, R. Flukiger, B. Bordini, L. Bottura and C. Scheuerlein, "Effects of neutron irradiation on pinning force scaling in state of the art Nb₃Sn wires," *Superconductor Science and Technology*, vol. 27, no. 1, pp. 1-7, 2014.

[106] A. A. Abrikosov, *Soviet Phys.-JETP* vol.5, p.1174 (1957), vol. 5, p. 1174, 1957.

[107] Y. B. Kim, C. F. Hempstead and A. R. Strnad, *Phys. Rev.*, vol. 131, p. 2486, 1963.

[108] Y. B. Kim, C. F. Hempstead and A. R. Strnad, *Phys. Rev.*, vol. 139, p. 1163, 1965.

[109] C. Kittel, *Introduction to Solid State Physics*, John Wiley & Sons, seventh edition, 1966.

[110] D. Dew Huges, "The metallurgical enhancement of type II superconductors," *Rep. Prog. Phys.*, vol. 34, pp. 821-873, 1971.

[111] D. Dew Hughes, "Flux pinning mechanisms in type II superconductors," *Philosophical Magazine*, vol. 30, pp. 293-305, 1974.

[112] R. M. Scanlan, W. A. Fietz and E. F. Koch, "Flux pinning centers in superconducting Nb₃Sn," *Journal of Appl. Phys.*, vol. 46, no. 5, pp. 2244-2249, 1975.

[113] W. Schelb and W. Schauer, "Improvement of Nb₃Sn high field critical current by a two stage reaction," *IEEE Transaction on Magnetics*, vol. Mag 17, no. 1, pp. 374-377, 1981.

[114] C. S. Pande and M. Suenaga, "A model of flux pinning by grain boundaries in type II superconductors," *Appl. Phys. Lett.*, vol. 29, pp. 443-444, 1976.

[115] D. Uglietti, "Electro-mechanical properties, microstructure and critical current of Nb₃Sn wires," 2006.

[116] A. Das Gupta, C. C. Koch, D. M. Kroeger and Y. T. Chou, "How Effectively can Grain Boundaries Pin Flux Lines?," *Advances in Cryogenic Engineering*, vol. 24, pp. 350-357, 1978.

[117] G. Zerweck, "On pinning of superconducting flux lines by grain boundaries," *Journal of Low*

Temperature Physics, vol. 42, no. 1/2, pp. 1-9, 1981.

[118] W. E. Yetter, D. A. Thomas and E. J. Kramer, "Grain-boundary flux pinning by the electron-scattering mechanism," *Philosophical Magazine Part B*, vol. 46, no. 5, pp. 523-537, 1982.

[119] D. O. Welch, "An approximation closed-form expression for the electron-scattering-induced interaction between magnetic flux lines and grain boundaries," *IEEE Transaction on Magnetics*, Vols. Mag-21, no. 2, pp. 827-830, 1985.

[120] W. W. Webb and A. Fietz, "Hysteresis in superconducting alloys—temperature and field dependence of dislocation pinning in niobium alloys," *Physical Review*, vol. 178, no. 2, pp. 657-667, 1969.

[121] J. W. Ekin, "Unified scaling law for flux pinning in practical superconductors: I. Separability postulate, raw scaling data and parameterization at moderate strains," *Superconductor Science and Technology*, vol. 23, no. 8, pp. 1-30, 2010.

[122] E. J. Kramer, "Scaling laws for flux pinning in hard superconductors," *Journal of Applied Physics*, vol. 44, no. 3, pp. 1360-1370, 1973.

[123] P. Holdway and R. D. Rawlings, "Microstructure and radiation damage of commercially produced Nb₃Sn tapes," *Cryogenics*, vol. 24, no. 3, pp. 137-142, 1984.

[124] T. Baumgartner, "Effects of Fast Neutron Irradiation on Critical Currents and Intrinsic Properties of State-of-the-Art Nb₃Sn Wires," Ph.D. dissertation unpublished, [Online] Available: <http://www.ub.tuwien.ac.at/d>, Phys. Dept., Technical University, Vienna, Austria, 2013.

[125] G. W. Cullen, *Proc. Summer Study on Superconducting Devices and Accelerators, Brookhaven National Laboratory*, p. 437, 1968.

[126] M. W. Guinan, A. van Konynenburg and J. B. Mitchell, "Effects of low temperature fusion neutron irradiation on critical properties of a monofilament niobium-tin superconductor," Informal Report, Lawrence Livermore National Laboratory, 1984.

[127] E. Seibt, "Irradiation and annealing effects of deuteron irradiated NbTi and V₃Ga multifilamentary composite wires at low temperature," *IEEE Transactions on Magnetics*, vol. 11, no. 2, pp. 174-177, 1975.

[128] E. Maier and P. Seibt, "Volume pinning force and upper critical field of irradiated Nb₃Sn," *Applied Physics Letters*, 39 (2): pp. 175-177, 1981., vol. 39, no. 2, pp. 175-177, 1981.

[129] N. R. Werthamer, E. Helfand and P. C. Hohenberg, "Temperature and Purity Dependence of the Superconducting Critical Field, H_{c2}. III. Electron Spin and Spin-Orbit Effects," *Phys. Rev.*, vol. 147,

no. 295, 1966.

[130] Adesso.

[131] Lortz.

[132] T. Otto, C. Scheurlein, R. Catherall, M. Glaser, O. Militaru, R. Flukiger, A. Ballarino and L. Bottura, "Radioactivity of Nb₃Sn/Cu wires after proton irradiation," *IEEE Trans. App. Superconductivity*, vol. 23, no. 3, p. 6000504, 2013.

[133] M. Soll, H. Bauer, K. Boening and R. Bett, *Physics Letters*, vol. 51A, p. 83, 1975.

[134] R. Meier-Hirmer and H. Kupfer, *J. Nucl. Mater.*, vol. 109, p. 593, 1982.

[135] M. Glaser, M. Huhtinen, F. Lemeilleura, C. Leroyb, P. Royb and M. Tavlet, "Radiation Test Facilities in the New PS East Hall At CERN".

[136] L. S. Esposito, F. Cerutti and E. Todesco, "Fluka energy deposition studies for the HL-LHC," in *Proceedings of IPAC 2013*, Shanghai, China, 2013.

[137] "Cryogenic Ltd.," <http://www.cryogenic.co.uk/products/vibrating-sample-magnetometer-vsm>.

[138] A. Niazi, P. Poddar and A. K. Rastogi, *Current science*, vol. 79, no. 1, july 2000.

[139] Vibrating sample magnetometer- manual, SWT Physic department, 2006.

[140] C. P. Bean, "Magnetization of High-Field Superconductors," *Rev. Mod. Phys.*, vol. 36, p. 31, 1964.

[141] "ac Susceptibility Measurements in High-T_c superconductors," PHY4803L - Advance Physics Laboratory, University of Florida - Department of Physics , 2012.

[142] L. S. Zevin and G. Kimmel, in *Quantitative X-ray Diffractometry*, edited by I Mureinik (Berlin Spinger), 1995a, pp. 35-45.

[143] R. E. Dinnebier and S. J. L. Billinge, *Powder Diffraction: Theory and Practice*, RSC Publishing, 2008.

[144] W. Pitschke, H. Hermann and N. Mattern, "The influence of surface roughness on diffracted X-ray intensities in Bragg Brentano geometry and its effect on structure determination by mean of Rietveld analysis," *Powder Diffr.*, vol. 8, no. 2, 1993.

[145] A. A. Chernyshov, A. A. Veligzhanin and Y. V. Zubavichus, "Structural Materials Science end-station at the Kurchatov Synchrotron Radiation Source: Recent instrumentation upgrades and experimental results," *Nucl. Instruments and Methods in Phys. Research A*, vol. 603, no. A, pp. 95-

98, 2009.

- [146] Y. V. Zubavichus, "A microstructure investigation of Nb3Sn samples using synchrotron radiation-based X-ray diffraction," Kurchatov Institute (Russia), 2015.
- [147] C. Senatore and R. Flukiger, "Formation and upper critical fields of the two distinct A15 phases in the subelements of powder in tube Nb3Sn wires," *App. Phys. Lett.*, vol. 102, no. 012601, 2013.
- [148] T. Boutboul, L. Oberli, A. den Ouden, D. Pedrini, B. Seeber and G. Volpini, "Heat treatment Optimization Studies on PIT Nb3Sn strand for the NED Project," *IEEE Transaction on Applied Superconductivity*, vol. 19, no. 3, pp. 2564-2567, 2009.
- [149] T. Spina, C. Scheurlein, D. Richter, B. Bordini, L. Bottura, A. Ballarino and R. Flukiger, "Variation of the Critical Properties of Alloyed Nb-Sn Wires after Proton Irradiation at 65 MeV and 24 GeV," *Applied Superconductivity, IEEE Transactions*, vol. 25, no. 3, 2014.
- [150] T. Spina, C. Scheurlein, D. Richter, L. Bottura, A. Ballarino and R. Flukiger, "Critical current density of Nb3Sn wires after irradiation at 65MeV and 24GeV protons," *Journal of Physics: Conference series*, vol. 507, p. 022035, 2014.
- [151] H. J. Bode and K. Wohlleben, "Enhancement of superconducting critical current density in Nb3Sn diffusion layers produced by irradiations with protons," *Phys. Lett. A*, vol. 24, no. 1, pp. 25-27, 1967.
- [152] R. Flukiger, T. Baumgartner, M. Eisterer, H. W. Weber, T. Spina, C. Scheurlein, C. Senatore, A. Ballarino and L. Bottura, "Variation of $(J_c/J_{c0})_{max}$ of Binary and Ternary Alloyed RRP and PIT Nb3Sn Wires Exposed to Fast Neutron Irradiation at Ambient Reactor Temperature," *IEEE Trans. App. on Superconductivity*, vol. 23, no. 3, p. 8001404, 2012.
- [153] R. M. Waterstrat and B. Dickens, *J. Appl. Phys.*, vol. 45, p. 3726, 1974.
- [154] R. Flukiger, J. L. Jorda, A. Junod and P. Fischer, *Appl. Physics Comm.*, vol. 1, p. 9, 1981.
- [155] P. Muller, W. Szymczak and G. Ischenko, *Nucl. Instrum. and Meth.*, vol. 149, p. 239, 1978a.
- [156] M. Lehmann and G. Saemann-Ischenko, *Phys. Lett.*, vol. 87A, p. 369, 1982.
- [157] A. Fasso, A. Ferrari, G. Smirnov, F. Sommerer and V. Vlachoudis, "FLUKA realistic Modeling of Radiation Induced Damage," *Progress in Nuclear Science and Technology*, vol. 2, pp. 769-775, 2011.
- [158] C. L. Snead Jr, R. C. Birtcher and M. A. Kirk, "Metastable reversal of the martensitic phase in Nb3Sn induced by energetic-electron irradiation," *Journal of Nuclear Materials*, vol. 244, pp. 273-277,

1997.

- [159] M. Soll, "Changing of the critical current density of Nb₃Sn," *Journal of Nuclear Materials*, vol. 72, pp. 122-128, 1978.
- [160] R. E. MacFarlane and R. M. Boicourt, "NJOY: A neutron and photon cross section processing system," *Trans. Am. Nucl. Soc.*, vol. 22, p. 720, 1975.
- [161] G. Ischenko, H. Mayer, H. Voit, B. Besslein and E. Haindl, "Einfluß der Bestrahlung mit hochenergetischen Sauerstoffionen auf die kritische Stromdichte supraleitender Nb₃Sn-Schichten," *Z. Physik*, vol. 256, pp. 176-184, 1972.
- [162] E. V. Semenov and A. Ryazanov, "DPA calculation to scale the existing database Ic vs fluence, based on elastic collisions and electronic stopping power in the production of the damage," Moscow, 2014.
- [163] P. Ferracin, G. Ambrosio, M. Anerella, F. Borgnolotti, R. Bossert, D. Cheng, D. R. Dietderich, H. Felice, A. Gosh, A. Godeke, S. Izquierdo Bermudez, P. Fessia, D. Krave, M. Juchno, J. C. Perez, L. Oberli, G. Sabbi, E. Todesco and M. Yu, "Magnet design of the 150mm aperture low β quadrupoles for the High Luminosity LHC," *IEEE Trans. on Applied Superconductivity*, vol. 24, no. 3, p. 4002306, 2014.
- [164] H. Hartmann, F. Ebert and O. Bretschneider, "Elektrolysen in Phosphatschmelzen. I. Die elektrolytische Gewinnung von α - und β -Wolfram," *Zeitschrift für anorganische und allgemeine Chemie*, vol. 198, p. 116.
- [165] H. Hartmann, F. Ebert and O. Bretschneider, "Elektrolysen in Phosphatschmelzen. I. Die elektrolytische Gewinnung von α - und β -Wolfram," *Zeitschrift für anorganische und allgemeine Chemie*, vol. 198, p. 116, 1931.
- [166] R. P. C. Schram, "RX-ray attenuation, Application of X-ray imaging for density analysis," Technical report, The Nuclear Research & consultancy Group , 2001.
- [167] H. a. O. Hittmair, *Supraleitung*, Verlag Karl Thiemig, no. ISBN 978-3521061132., 1979.
- [168] E. C. v. R. a. R. M. Waterstrat, *Acta Cryst.*, vol. B 24, p. 186, 1968.
- [169] M. T. Robinson, 1969.
- [170] Groom.
- [171] G. Gladyshev.

[172] K. B. a. H. B. M. Söll, "Influence of disordering by low-temperature neutron irradiation on the superconducting transition temperature of Nb₃Sn," *Journal of Low Temperature Physics*, vol. 24, no. 5-6, pp. 631-644, 1976.

[173] R. W. R. a. Y. Anjaneyulu, "Position dependent flux pinning by proton irradiation damage thick niobium samples," *Journal of Applied Physics*, vol. 48, no. 3, pp. 1296-1300, 1977.

[174] T. H. G. S. G. a. E. C. B. T. Matthias, "Superconductivity of Nb₃Sn," *Phys. Rev.*, vol. 95, p. 1435, 1954.

[175] P. M. a. E. Seibt, "Volume pinning force and upper critical field of irradiated Nb₃Sn," *Applied Physics Letters*, 39 (2): pp. 175-177, 1981., vol. 39, no. 2, pp. 175-177, 1981.

[176] F. Goodenough and J. B. Bachner, "Superconducting transition temperature and electronic structure in the pseudobinaries Nb₃Al-Nb₃ Sn and Nb₃Sn-Nb₃Sb," *J. Phys. Chem. Solids*, vol. 28, pp. 889 -895, 1967.

[177] D. Rodrigues Jr, C. L. H. Thieme, D. G. Pinatti and S. Foner, "Grain boundary composition, transport and flux pinning of multifilamentary Nb₃Sn wires," *IEEE Transaction on Applied Superconductivity*, vol. 5, no. 2, pp. 1607-1610, 1995.

[178] R. Labusch, *Crystal Lattice Defects*, vol. 1, no. 1, 1969.

CURRICULUM VITAE

Name: Tiziana Spina

Date of birth: 05.06.1984

Place of birth: Isernia (Italy)

Address: Via Pulsone, n°5, 86021 Boiano (CB, Italy)

EDUCATION AND EXPERIENCE

2012-2015 – PhD research at the University of Geneva (Switzerland) and at CERN (TE-MSC-SCD)

2008-2011 – Master degree in Physics (curriculum: Physics of Matter) at the University of Naples Federico II (Italy).

Diploma thesis: “Measurement of transverse resistivity in superconductive strands with electric and magnetic techniques”. This thesis work was performed in the laboratories of ENEA Frascati (Rome, Italy).

2003-2008 – Bachelor degree in Physics at the University of Naples Federico II (Italy).

1998-2003 – High school diploma (Scientific Lyceum in Boiano, Italy)

PUBLICATIONS

- T. Spina, C. Scheuerlein, D. Richter, A. Ballarino, F. Cerutti, L.S. Esposito, A. Lechner and L. Bottura, R. Flükiger, “Correlation between the number of displacements per atom

(dpa) and Tc after high energy irradiations in Nb₃Sn wires for HL-LHC accelerator”, to be published (EUCAS 2015)

- T. Spina, C. Scheuerlein, D. Richter, B. Bordini, L. Bottura, A. Ballarino, R. Flükiger, “High energy proton irradiation on Nb₃Sn wires and thin platelets for the HL-LHC accelerator”, to be published (M2S 2015)
- T. Spina, C. Scheuerlein, D. Richter, B. Bordini, L. Bottura, A. Ballarino, and R. Flükiger, “Variation of the Critical Properties of Alloyed Nb-Sn Wires After Proton Irradiation at 65 MeV and 24 GeV”, *App. Supercond. IEEE Trans.*, vol. 25 (3), 2015.
- T. Spina, C. Scheuerlein, D. Richter, L. Bottura, A. Ballarino, R. Flükiger, “Critical current density of Nb₃Sn wires after irradiation with 65MeV and 24GeV protons”, Journal of physics: Conference series vol. 507, 2014. DOI: 10.1088/17426596/507/2/022035.
- R. Flükiger and T. Spina, “The behavior of copper in view of radiation damage in the LHC luminosity upgrade”, *Proceedings of WAMSDO: Workshop on accelerator magnet superconductors, design and optimization*, edited by E. Todesco, CERN-2013-006, pp. 76-82, DOI:10.5170/CERN, Geneva, 2013.
- R. Flükiger, T. Baumgartner, M. Eisterer, H.W. Weber, T. Spina, C. Scheuerlein, C. Senatore, A. Ballarino, L. Bottura, “Variation of (J_c/J_{c0})_{max} of binary and ternary alloyed RRP and PIT Nb₃Sn wires exposed to fast neutron irradiation at 300K”, *App. Supercond. IEEE Trans.*, vol. 23 (3), 2013.
- M. Breschi, M. Massimini, T. Spina, V. Corato, “Experimental and theoretical analysis of transverse resistances in a Nb₃Sn LMI-EM strand”, *App. Supercond., IEEE Trans.*, vol 23 (3), 2013.
- C. Zhou, M. Dhallé, A. Nijhuis, M. Breschi, T. Spina, A. della Corte and V. Corato, “Comparison of direct inter-filament resistance measurement on Nb₃Sn strands between University of Twente and ENEA”, *App. Supercond., IEEE Trans.* vol.2 (3), 2013.

- L. Muzzi, V. Corato, A. della Corte, G. De Marzi, T. Spina, J. Daniels, M. Di Michiel, F. Buta, G. Mondonico, B. Seeber, R. Flükiger and C. Senatore, “Direct observation of Nb₃Sn lattice deformation by high energy X-ray diffraction in internal-tin Nb₃Sn wires subject to mechanical loads at 4.2K”, *Supercond. Sci. Technol.* 25 054006, 2012.
- Tiziana Spina, Valentina Corato, Gianluca De Marzi, Chiarasole Fiamozzi Zignani, Luigi Muzzi, Umberto Gambardella, Pasquale Fabbricatore, and Antonio della Corte, “Comparison between direct and indirect measurements of the transverse resistivity in NbTi strands”, *Elsevier Ltd. Physics Procedia*, 2011 available online at www.sciencedirect.com